Mode Conversion Losses in Overmoded Millimeter Wave Transmission Lines

by

David S. Tax

C.A.S., Acadia University (2003)
B.Eng. (Electrical), Dalhousie University (2006)

Submitted to the
Department of Electrical Engineering and Computer Science
in partial fulfillment of the requirements for the degree of

Master of Science

at the

MASSACHUSETTS INSTITUTE OF TECHNOLOGY

September 2008

Signature of Author . . . .
Department of Electrical Engineering and Computer Science
August 29, 2008

Certified by . . . .
Richard J. Temkin
Senior Research Scientist, Department of Physics
Thesis Supervisor

Accepted by . . . .
Professor Terry P. Orlando
Chairman, Committee on Graduate Students
Department of Electrical Engineering and Computer Science
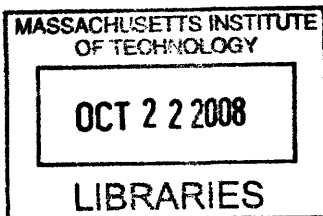
Mode Conversion Losses in Overmoded Millimeter Wave Transmission Lines

by

David S. Tax

Submitted to the Department of Electrical Engineering and Computer Science
On August 29, 2008, in partial fulfillment of the
requirements for the degree of
Master of Science

Abstract

Millimeter wave transmission lines are integral components for many important applications like nuclear fusion and NMR spectroscopy. In low loss corrugated transmission lines propagating the HE_{11} mode with a high waveguide radius to wavelength ratio (a/λ), the transmission line loss is predominantly a result of mode conversion in components such as miter bends. The theory for determining losses in miter bends though is only approximate, and is based instead on the problem of the loss across a diameter-length gap between two waveguide sections. Through simulation, we verified that the existing analytic theory of this gap loss is correct; however, our simulations could not verify the assumption that the miter bend loss is half the loss in the gap. We also considered the problem of higher order modes (HOMs) mixed with an HE_{11} input entering the miter bend. Using a numerical technique, we found that the loss through the miter bend is dependent on both the amplitude of the HOM content as well as its phase relative to the phase of the HE_{11} mode. While the overall loss averaged across all phases remains the same with increasing HOM content, the power that fails to traverse the gap tends to increase, and it is this power that appears as very high order modes that will cause heating around the miter bend. For the ITER transmission line, the loss based on gap theory is 0.027 dB and, using a coherent technique, we measured a loss of 0.05 ± 0.02 dB with a vector network analyzer (VNA). We also set out to measure the mode conversion caused by a miter bend by using a 3-axis scanner system to measure the field patterns within the ITER waveguide. Due to the presence of higher order modes output by the HE_{11} launcher, definitive results on the mode conversion attributed to the miter bend could not be obtained. Using a phase retrieval code, we were able to calculate the mode purity of the launcher output and found it to be 98 ± 0.5 %. Future work will concentrate on reducing this HOM content to enable measurements of the miter bend mode conversion.

Thesis Supervisor: Richard J. Temkin
Title: Senior Research Scientist, Department of Physics

Acknowledgements

First and foremost, I need to acknowledge my parents, Ted and Cara Tax. They have never ceased to support me in everything I do, and this thesis was no exception. They have always encouraged me to succeed and have admirably filled the role as my #1 fan. My sisters, Jaimie and Dana, have also always been great supporters of mine too, and of course I can't forget about Cody.

Next, I want to thank Dr. Richard Temkin for his expertise and enthusiasm. His knowledge and advice have been extremely valuable since I first arrived here at MIT. I also want to thank Dr. Jagadishwar Sirigiri for his guidance and assistance, Dr. Michael Shapiro for all his help in the theory department, and Ivan Mastovsky for looking after the construction of any parts that were needed along the way.

Moving along, I want to thank Nick Comfoltey for putting up with me these last two years. It was great sharing an office with someone so easy to talk to, and I'm glad that I had the opportunity to bring out the Canadian within him. I would also like to acknowledge my other lab-mates, Antonio, Antoine, Roark, Colin, and Brian, who were all normally more than willing to humor my various sports rants. Last but not least, I want to thank all my friends at MIT for making the last two years so enjoyable. So if you know me, and you somehow get a hold of this thesis, then I'm probably acknowledging you.

Table of Contents

List of Figures

List of Tables

Chapter 1

Introduction

At one time, the term "transmission line" would evoke no other image in one's mind beyond the massive system of cables supplying electric power to homes and businesses around the world. While these are still arguably the most common transmission lines, new technologies are constantly being developed that require some sort of system to transmit power from one location to another. There are a variety of ways to accomplish this task, and the implementation differs greatly based on the frequency of the transmitted power.

For direct current (DC) or low frequency AC applications like electric power transmission, which operates at 50 or 60 Hz depending on the country, simple conducting wires suffice for transmission lines. At higher frequencies, the conduction loss from standard metal wire is much larger; therefore it is preferable to use an alternative like coaxial cable. Coaxial cables are particularly applicable in the radio frequency (rf) range up to a few GHz for applications such as television signals (which are typically a few hundred MHz). In other fields, the maximum data rate that can be transmitted across the transmission line is paramount. In these cases, fiber optics, which generally transmit a modulated signal in the visible spectrum (several hundred THz), are usually the system of choice.

Thus far there has been no discussion of the microwave region of the electromagnetic spectrum which includes frequencies from approximately 300 MHz to 300 GHz. The upper portion of this frequency range is also often referred to as the millimeter waves region since wavelengths are on the scale of a few millimeters. Transmission of microwaves is usually accomplished by means of waveguides that, as the name would indicate, guide electromagnetic waves within metallic or dielectric walls.

While we have known for a while of the benefits to using microwaves for various applications, a lack of appropriate sources in the frequency range has left many of these unexplored thus far. The most common source is the magnetron, which can be found in any household microwave oven; however other sources are required to explore other portions of the microwave spectrum at higher power levels. One such source is the gyrotron, and research is constantly ongoing to push the output power and efficiency higher for higher frequencies. There are many important applications in the microwave frequency spectrum that require millimeter wave transmission lines and a brief description of a few of these applications follows.

1.1 Applications of Millimeter Wave Transmission Lines

1.1.1 Nuclear Fusion – Electron Cyclotron Heating

One major application for millimeter wave transmission lines, and perhaps one of the most important, is nuclear fusion. In this day and age, with increasing worries about global warming as a result of carbon emissions and the depletion of resources currently used for energy production, nuclear fusion provides a bright alternative that does not produce any unwanted carbon or radioactive byproducts and utilizes resources for which there is an abundance. Though this all sounds well and good, the technology is not yet a reality in terms of producing a commercially viable energy producing reactor due to the engineering and physics challenges that still face the scientific community. This is where the project now known simply as ITER comes in, as it attempts to bridge the gap between a final commercial reactor and the current state of fusion research. A conceptual design of the ITER tokamak is shown in Figure 1-1. The ITER project is an international collaboration between the United States, Europe, China, Japan, South Korea, Russia, and India. Each ITER member is responsible for supplying certain components and supporting ITER-relevant research efforts. In fact, much of the work in this thesis was in support of the US ITER team, who are responsible for supplying many of the transmission lines that will be required on ITER.

13

Figure 1-1: Proposed design for the ITER tokamak [1]

A nuclear fusion reaction involves the fusing of two small nuclei and results in a heavier atom along with neutrons, protons, and energy, depending on the initial atoms. In ITER, the reaction of choice will fuse two hydrogen isotopes, deuterium and tritium, resulting in a helium atom, a neutron, and a large amount of energy. The difficulty in harnessing sufficient power from this reaction stems from the fact that, at standard temperature and pressure, the reaction is extremely rare. In order to increase the energy output, it is necessary to increase the collision frequency between the reactants, which can be accomplished by raising the temperature. This though is no easy task, since the

ignition point, where the energy resulting from reactions is sufficient to maintain the temperature, is in the realm of 100 million degrees Celsius. At such high temperatures, the normally gaseous reactants exist as a plasma, a state of matter in which the electrons are no longer bound to the nuclei.

Clearly, given the temperatures involved, plasma confinement is very important. Luckily, this is made easier by the characteristics of the plasma since both species, the ions and electrons, can be manipulated with electric and magnetic fields. There are several proposed devices to confine the plasma, like the stellarator or inertial confinement (ICF) based devices; however for ITER, the scientists and engineers based their design on what is arguably the most popular and promising device: the tokamak. The tokamak, first conceived in Russia during the 1950s, is a toroidal structure that confines the plasma using a series of magnetic field coils around various cross-sections of the torus as well as poloidal field coils to ensure the plasma remains well confined.

As mentioned previously, incredibly high temperatures are required for a fusion plasma to attain ignition. In order for the plasma to reach such temperatures, a vast amount of external heating is necessary. There are several ways to heat a plasma, each of varying technological difficulty. One of the easiest ways to heat a plasma is Ohmic heating. Ohmic heating simply involves inducing a current through the plasma which results in heating due to the plasma's resistance. Ohmic heating however can not provide a complete solution to the heating problem since the plasma resistivity decreases with increased plasma temperature, and it is therefore ineffective beyond temperatures of about 10 million degrees Celsius. Several auxiliary heating methods have been considered, such as neutral beam heating and ion cyclotron heating (ICH), however technical challenges of each method have prevented them from being feasible options at this time and have led to electron cyclotron heating (ECH) becoming the method of choice.

Electron cyclotron heating transfers energy to the plasma by means of cyclotron damping, a mechanism sometimes referred to as collisionless damping. Cyclotron damping involves the absorption of an electromagnetic wave's energy when the wave's frequency is approximately equal to a resonant frequency of the particle. In the case of ECH, the frequency of interest is the electron cyclotron frequency, which is defined as:

$$\omega_c = \frac{eB}{\gamma m_e} \tag{1.1}$$

where e is the charge of an electron, m_e is the mass of an electron, B is the external magnetic field strength, and $\gamma = \dfrac{1}{\sqrt{1 - v^2/c^2}}$. For ITER, this frequency is 170 GHz.
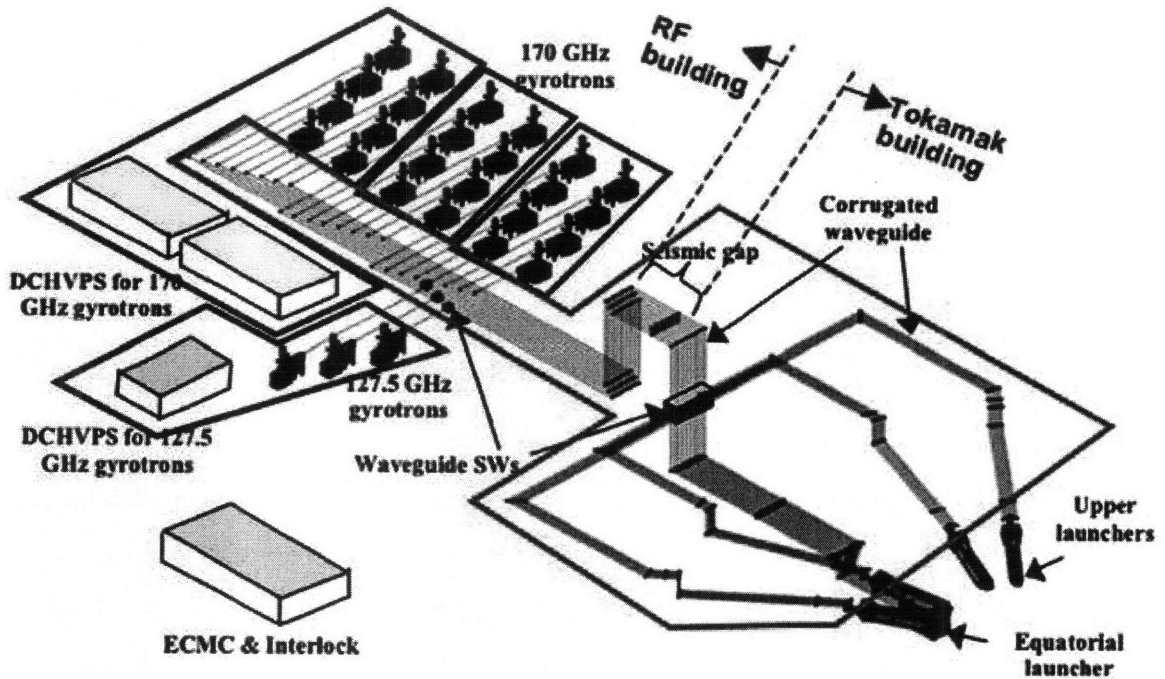
Figure 1-2: Diagram of the design for the ITER electron cyclotron heating (ECH) system [2]

In order to reach ignition, auxiliary power levels on the scale of tens of megawatts will be required. At one time, ECH did not appear very promising due to the lack of available sources; however intense research in the gyrotron field has indicated that such sources are now a reality. Various gyrotrons have demonstrated power outputs on the order of 1 MW at 170 GHz with pulse lengths on the scale of minutes, pushing ever closer to the design specifications laid out by the ITER team for the ECH system. The ECH system on ITER currently calls for 24 1 MW gyrotrons, which should supply 20 MW of 170 GHz power to the plasma [3]. This is where the millimeter wave transmission lines come in since all the power must be transmitted from the gyrotrons to the tokamak, which will be housed in a separate building. Figure 1-2 contains a diagram

showing the gyrotrons and transmission lines for the proposed ITER ECH system. The ITER team has designed a transmission line that should minimize losses; however the lack of a complete theoretical understanding of all transmission line components, along with imperfections in gyrotron output beams and the high power levels involved create some uncertainty.

Determining the losses to be expected in the transmission line is an important task to ensure that the system meets ITER design specifications. As mentioned previously, theoretical estimation of the line losses can be a difficult and imprecise task. In addition, the size of the transmission line components relative to the wavelength of the power is extremely large, making it impossible to solve the complete problem using most available numerical simulation codes; therefore experimental testing of the transmission line components is a necessary step to assure the ITER design team that the ECH system will perform as expected. Several of the measurements to follow in this thesis will use this ITER ECH prototype transmission line.

1.1.2   Plasma Diagnostics – Electron Cyclotron Emission

In the previous section, the ITER project was introduced along with the basic principles of nuclear fusion. What have not been discussed thus far are the goals for ITER. The first objective for ITER is to demonstrate a fusion plasma that reaches ignition. Another way to state this objective is for the reactor to have a Q greater than one, meaning that the energy output surpasses the energy input. This represents an important step in proving the feasibility of a future commercial fusion reactor. The second objective for ITER is to advance the knowledge in the field of plasma physics. It is this second objective that will actually command the majority of ITER's run time.

When ITER is eventually constructed, it will not simply consist of walls, confinement systems, and heating systems; it will also consist of a number of plasma diagnostics. These plasma diagnostics are systems that are installed outside and within the tokamak's vacuum chamber which have the ability to measure things like the temperature or density profiles of the plasma. These profiles are very important to the scientists trying to learn more about plasma behavior and the various instabilities that can arise during operation.

17

Within the plasma, the electrons move in a helical trajectory, spiraling around the magnetic field lines with an angular frequency equivalent to the electron cyclotron frequency, defined by Eqn (1.1). In the tokamak's toroidal configuration, the magnetic field is not constant throughout the entire cross-section, varying along the path from the inner wall to the outer wall. This variation in the magnetic field strength means that the electron cyclotron frequency will also have a radial dependence. In the previous section, electron cyclotron heating was discussed in which the electrons absorb energy at the electron cyclotron frequency; however it should also be noted that electrons emit radiation at this frequency, as well as its harmonics. This is known as electron cyclotron emission (ECE), and plasma diagnostics can be designed to take advantage of this phenomenon.
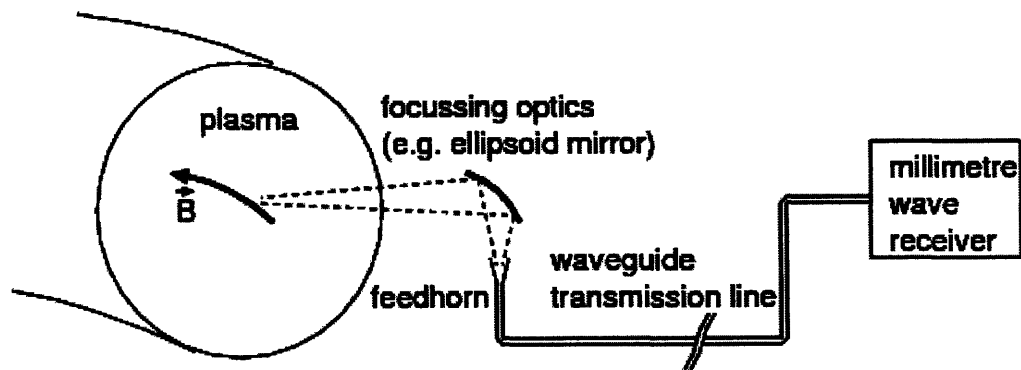
Figure 1-3: Typical electron cyclotron emission (ECE) diagnostic setup [4]

If a plasma is optically thick at the frequency of interest, meaning that nearly all the energy of an electromagnetic wave that passes through is absorbed, the plasma will radiate as a black-body source. For such a plasma, the intensity of the black-body emission will depend only on the electron temperature [5]. ECE diagnostics are founded on these aforementioned principles. A high directivity antenna receives the ECE microwave radiation along a narrow line of sight that is generally chosen perpendicular to the magnetic field lines. This power is coupled into a millimeter wave transmission which transmits the power to a frequency resolving system. This final system will then decompose the received power spectrum, of varying intensity across a frequency band, into a

physical result indicating the electron temperature profile along the cross-section. Thus far, ECE diagnostics have proven to be an effective tool for retrieving electron temperature profiles [6].
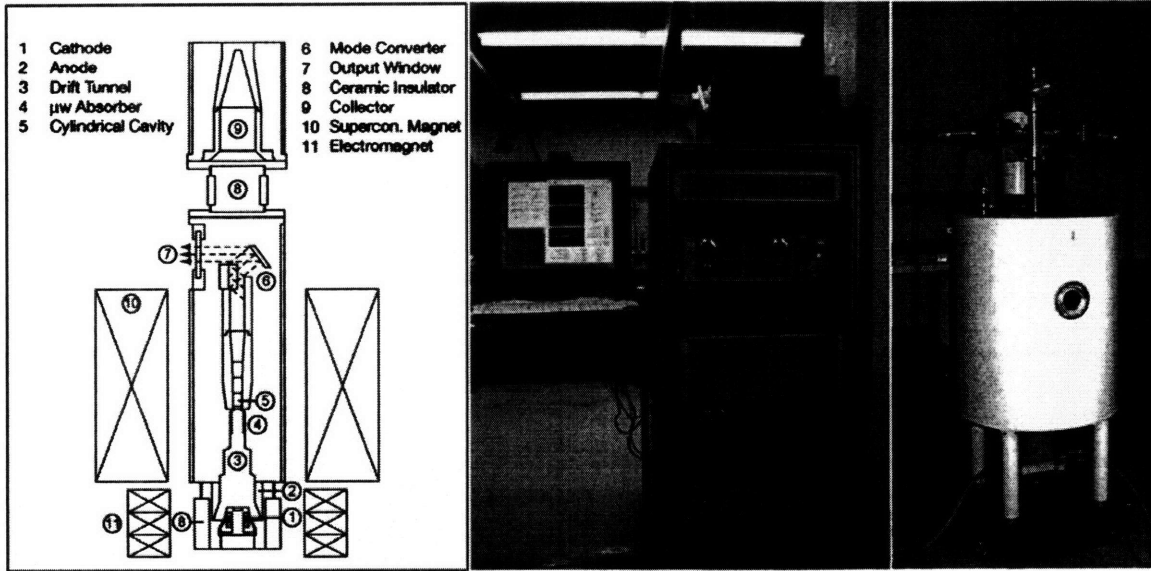
Figure 1-4: Schematic and photos of a 460 GHz gyrotron for nuclear magnetic resonance (NMR) applications [7]

1.1.3   Spectroscopy – Nuclear Magnetic Resonance

In section 1.1.1, the gyrotron was introduced as a millimeter wave source capable of producing MW outputs. Here, we explore another important application of the gyrotron: nuclear magnetic resonance (NMR) spectroscopy.

NMR spectroscopy is an important tool to those in the chemistry, biological science, and medical fields. NMR takes advantage of the quantum mechanical property of spin, meaning that the nucleus has a non-zero magnetic moment. Commonly, NMR systems take advantage of nuclei with a spin of one half such as protons (^{1}H). In this case, the nucleus can take on a spin state of either ½ or -½. The NMR signal is proportional to the difference in the population between the N_+ spins occupying the low energy level and the N_- spins occupying the high energy level. In thermal equilibrium, the relative population of the two states is given by $N_-/N_+ = \exp(\Delta E/k_B T)$, where k_B is the Boltzmann constant, T

is the temperature, and the energy difference between the two states is $\Delta E = \hbar\gamma_p B_{NMR}$ with $\hbar$ being Planck's constant, γ_p is the proton gyromagnetic ratio, and B_{NMR} the applied magnetic field. Even for a large magnetic field, the small energy difference results in a weak polarization $P = (N_+ - N_-)/(N_+ + N_-) = \tanh(\Delta E/2k_B T)$, on the order of a fraction of a percent. On the other hand, electron paramagnetic resonance (EPR), which takes advantage of the spin property of electrons, can exhibit a polarization on the order of a few percent under the same conditions. This property can be exploited by using a technique known as dynamic nuclear polarization (DNP) to enhance the signal-to-noise ratio of NMR experiments.
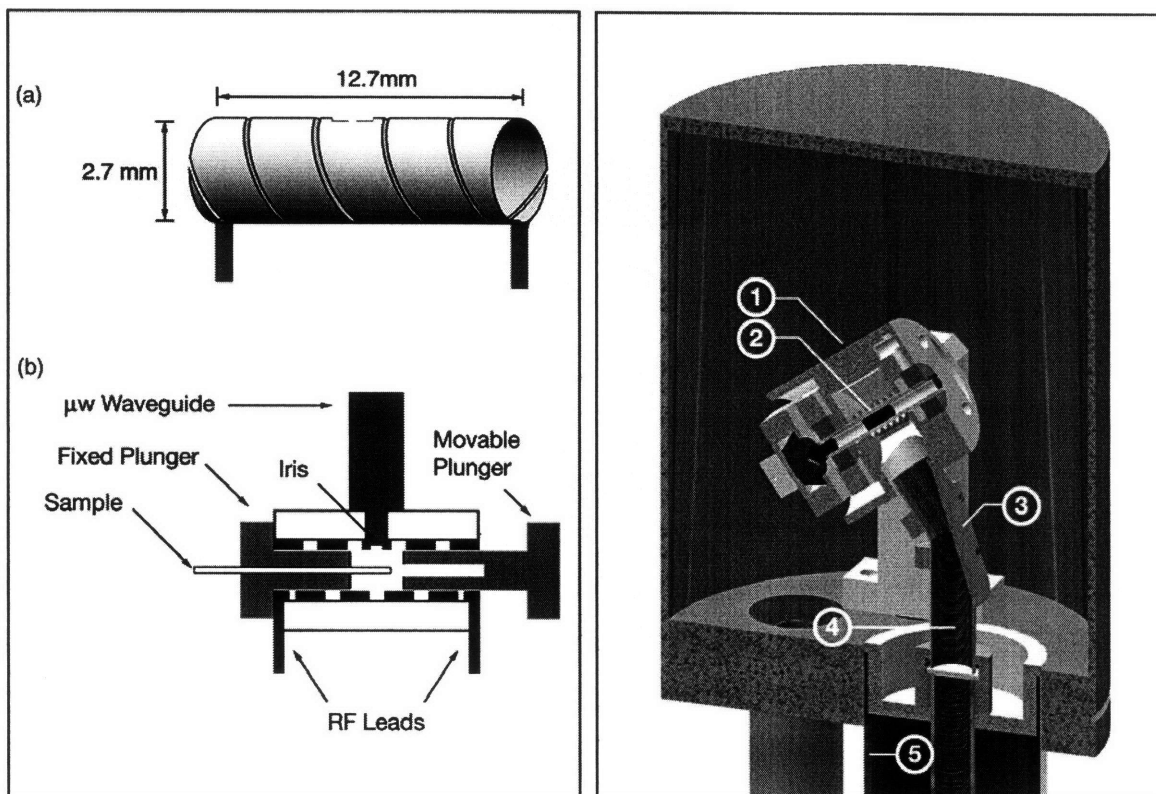
Figure 1-5: Left - Probe used for DNP in liquids and solids [8], Right - Zoomed out view of another DNP probe showing millimeter wave transmission lines, (1) – Stator, (2) – Sample, (3) – Waveguide bend, (4) – Inner conductor, (5) – Outer conductor [9]

DNP involves transferring the large polarization of the electron spins to the nuclear spins by irradiating the sample with electromagnetic waves at a frequency around the

electron Larmor frequency. Theoretically, signal enhancement on the order of $\gamma_e/\gamma_p \sim$ 660, where γ_e is the electron gyromagnetic ratio, is possible [10]. Generally, NMR setups use high magnetic field strengths, > 5T, thus sources in the 100s of GHz are required. These sources should be able to produce tens of watts of power since the signal enhancement scales with power [11], and should have pulse lengths sufficient for a near complete transfer of polarization [12]. The gyrotron is an excellent source to fulfill the above requirements and one of these devices for NMR applications is shown in Figure 1-4. The gyrotron though is no small device, and it also requires a powerful magnet of its own, therefore the source and the sample must be some distance away from one another and thus a millimeter wave transmission line is required to transmit the power.

1.1.4 Radar

Radar is another important application that necessitates the use of microwave transmission lines

While the concept of radar had been around for a while, it wasn't until the World War 2 era where it truly came into prominence and emerged as one of the most important technologies of its time. The concept of radar is fairly simple: transmit electromagnetic waves into free space, and if an object is in range, then the waves will be reflected back and can be detected by a receiver. The ability to detect various objects using radar is strongly dependant on the frequency of the source, or more intuitively it's dependant on the wavelength of the electromagnetic waves. Due to the numerous applications for radar systems (weather, air traffic control, defense, etc.), there is a demand for radar systems at rf frequencies right through to millimeter wave frequencies. Transmission lines are again an integral part of a radar system. These transmission lines should have very low loss to retain a high signal to noise ratio of the detected signals, which are often quite small. They also must ensure the integrity of any incoming signal, since most radar systems are quite sensitive, and any abnormality introduced by such transmission lines could easily be misinterpreted.

1.2 Thesis Outline

This thesis presents a body of work covering theory and experiments pertaining to millimeter wave transmission lines.

Chapter 2 covers the theory of transmission line losses, beginning with the basic electromagnetic principles involved in dealing with waveguides, and continuing into a discussion of how losses are calculated in a real transmission line system. In chapter 3, numerical simulations of transmission line components are compared with the transmission line theory discussed in the previous chapter. Chapter 4 provides a theoretical look into a problem that has not previously received much consideration: an impure waveguide mode at the input of transmission line components. This problem is solved numerically and using established analytical expressions, and is followed by a discussion of the consequences the results.

The next two chapters are dedicated to experimental work. Chapter 5 considers two methods for measuring losses in transmission lines and the results for two separate transmission lines are presented. Chapter 6 approaches the loss measurement from a different perspective, instead determining the mode content within the transmission line. Mode content measurements for the ITER ECH prototype transmission line are presented.

Finally, Chapter 7 summarizes the work within this thesis, presenting conclusions on the results and a discussion of future work that can be done.

Chapter 2

Theory of Millimeter Wave Transmission Line Losses

In Chapter 1, there was a brief discussion about the different types of transmission lines that are applicable for various application frequencies. For the region of the electromagnetic spectrum known as millimeter waves, transmission lines typically consist of waveguide. Thus, before discussing the losses in such transmission line systems, it is necessary to cover the basic electromagnetic principles involved in dealing with waveguides.

2.1 Propagation in Waveguides

2.1.1 Electromagnetic Basics

The basis for anything and everything in electromagnetics is Maxwell's equations and the constitutive relations:

$$\nabla \times \bar{H} = \frac{\partial}{\partial t} \bar{D} + \bar{J} \tag{2.1}$$

$$\nabla \times \bar{E} = -\frac{\partial}{\partial t} \bar{B} \tag{2.2}$$

$$\nabla \cdot \bar{D} = \rho \tag{2.3}$$

$$\nabla \cdot \bar{B} = 0 \tag{2.4}$$

$$\bar{D} = \varepsilon \bar{E} \tag{2.5}$$

$$\bar{B} = \mu \bar{H} \tag{2.6}$$

23

where H is the magnetic field strength, D is the electric displacement, J is the electric current density, E is the electric field strength, B is the magnetic flux density, and p is the electric charge density. Each of the above listed terms may carry both a spatial and time dependence. The permittivity ε and the permeability μ are simply positive constants for free space and basic isotropic media. These are the only cases that will require consideration in this thesis.

In general, for most practical applications, the fields are time harmonic, and can be written in the form $\bar{E}(r,t) = \mathrm{Re}\{\bar{E}(r)e^{-j\omega t}\}$, where $\bar{E}(r)$ can be a complex quantity. This simplifies theoretical analysis using Maxwell's equations by allowing the time derivatives to be replaced by $-j\omega$.

Another important equation, which can be obtained from simple manipulation of Maxwell's equations, is the wave equation for $\bar{E}$:

$$\left(\nabla^2 + \omega^2 \mu \varepsilon\right)\bar{E} = 0 \tag{2.7}$$

for the time harmonic case in a source-free region. The simplest solution to the wave equation is of the form: [13]

$$\bar{E} = \hat{x}E_0 \cos(kz - \omega t) \tag{2.8}$$

By introducing this solution to the wave equation, a very important equation known as the dispersion relation is obtained:

$$k^2 = \omega^2 \mu \varepsilon \tag{2.9}$$

This equation relates the frequency of the wave to k, known as the wavenumber or the spatial frequency. $\bar{k}$ is actually a vector, called the wave vector, that indicates the direction of propagation of the wave.

2.1.2   Boundary Conditions and Waveguide Modes

When there exists a boundary between two different media, a set of equations relating the normal and tangential components of the electric and magnetic fields within the two media are used:

24

$$\hat{n} \times \left(\vec{E}_1 - \vec{E}_2 \right) = 0 \qquad (2.10)$$

$$\hat{n} \times \left(\vec{H}_1 - \vec{H}_2 \right) = \vec{J}_s \qquad (2.11)$$

$$\hat{n} \cdot \left(\vec{B}_1 - \vec{B}_2 \right) = 0 \qquad (2.12)$$

$$\hat{n} \cdot \left(\vec{D}_1 - \vec{D}_2 \right) = \rho_s \qquad (2.13)$$

These boundary conditions are particularly useful when considering waveguide problems. Waveguide is commonly a rectangular or cylindrical structure that allows power to propagate in one direction while metallic or dielectric walls confine the wave in the other directions. Therefore, solving for the fields within a waveguide is more or less a matter of satisfying the boundary conditions at the walls.

There is one other key principle to take note of before solving waveguide problems, and that is superposition. Using superposition, the complete problem can be separated into two simpler cases where there is only one field, magnetic or electric, with a component in the longitudinal direction (in the direction of propagation). When all electric fields are transverse to the direction of propagation, and thus the longitudinal component is zero, the fields are referred to as transverse electric (TE). When the longitudinal component of the magnetic field is zero and thus all magnetic fields are transverse to the direction of propagation, the fields are referred to as transverse magnetic (TM).

To illustrate propagation in a waveguide, the mathematically simpler case of a metallic rectangular waveguide is considered first. For a guided wave propagating in the $\hat{z}$ direction, the z dependence of the fields will be of the form $e^{\pm jk_z z}$, where k_z is the z component of the wave vector. This allows for the substitution of all z derivatives with jk_z. After separating out the transverse components, denoted by the subscript t, of all field vectors, Eqns (2.1) and (2.2) are written as: [13]

$$\left(\nabla_t + \hat{z} jk_z \right) \times \left(\vec{H}_t + \vec{H}_z \right) = -j\omega\varepsilon\left(\vec{E}_t + \vec{E}_z \right) \qquad (2.14)$$

$$\left(\nabla_t + \hat{z} jk_z \right) \times \left(\vec{E}_t + \vec{E}_z \right) = j\omega\mu\left(\vec{H}_t + \vec{H}_z \right) \qquad (2.15)$$

and the corresponding wave equations can be obtained:

$$\left(\nabla_t^2 + \omega^2 \mu\varepsilon - k_z^2\right)E_z = 0 \qquad (2.16)$$

$$\left(\nabla_t^2 + \omega^2 \mu\varepsilon - k_z^2\right)H_z = 0 \qquad (2.17)$$

For TM fields, $H_z = 0$, and the fields are determined by the solution of Eqn (2.16), while for TE fields, $E_z = 0$, and the fields are determined by the solution of Eqn (2.17).

As seen in Eqn (2.8), the solution to the wave equation is sinusoidal, however now taking into account the geometry of the waveguide, there will be a sinusoidal dependence in both transverse directions, $\hat{x}$ and $\hat{y}$. The exact nature of the solution is obtained after considering the boundary conditions.

Since the metallic walls can be approximated as a perfect conductor, the electric field outside the waveguide must be zero, which requires that the tangential electric field within the waveguide along the walls must be zero as well. Therefore, if we define a coordinate system such that the two sides of the waveguide span (0,a) and (0,b) respectively, the TM field solution is:

$$E_z = e^{jk_z z} \sin k_x x \sin k_y y \qquad (2.18)$$

The tangential electric and magnetic field components can be derived from this solution using Eqns (2.14) and (2.15). However, this solution is not yet complete since the boundary condition at $x = a$ and $y = b$ must also be satisfied, which imposes the following conditions:

$$k_x a = m\pi \qquad (2.19)$$

$$k_y b = n\pi \qquad (2.20)$$

where m and n are positive integers. A similar solution for the TE fields can be obtained with the same conditions applying.

The conditions in Eqns (2.19) and (2.20) indicate that there are multiple solutions. Each independent combination of m and n is known as a mode of the waveguide. For example, the TM$_{14}$ mode will have 1 maximum in the x direction and a total of 4 maxima or minima in the y direction. It should be noted that the assignment of x and y is arbitrary, however the convention is that the first number corresponds to the side which is longer. The lowest order TM mode is the TM$_{11}$ mode since from Eqn (2.18), neither m

26

nor n can be zero, otherwise E_z would be identically zero. For TE fields, m or n can be zero, and the lowest order mode is the TE$_{10}$ mode.

As introduced in the previous section, there is a dispersion relation associated with the solution to the wave equation, shown in Eqn (2.9). The wavenumber k can be represented by its components such that $k^2 = k_x^2 + k_y^2 + k_z^2$ and the guidance condition for the waveguide can be established:

$$k_z = \sqrt{\omega^2 \mu_0 \varepsilon_0 - (m\pi / a)^2 - (n\pi / b)^2} \qquad (2.21)$$

This guidance condition determines whether or not a particular mode can propagate in a waveguide of dimensions a x b at a frequency ω. If $\omega^2 \mu_0 \varepsilon_0 < (m\pi / a)^2 + (n\pi / b)^2$, then k_z will be imaginary, and from Eqn (2.18) it is apparent that the electric field will attenuate exponentially in the direction of propagation. This is known as cutoff. Thus for a given waveguide, each mode will have a corresponding cutoff frequency, below which the mode will not be able to propagate through the waveguide.

This concept of waveguide modes is integral in handling waveguide problems since, in real systems, it is highly preferable to be able to treat the fields as a summation of modes rather than dealing with the field functions within the coordinate system.

2.1.3   Cylindrical Waveguide

The derivation of the modes of a circular cylindrical waveguide is essentially the same as that for a rectangular waveguide, however cylindrical coordinates are used instead. The solution to the wave equation in cylindrical coordinates is comprised of the product of a Bessel function and a sinusoid. For the TM case, this solution is: [13]

$$E_z = e^{jk_z z} J_m(k_\rho \rho) \cos m\varphi \qquad (2.22)$$

and the dispersion relation is:

27

$$k_z^2 + k_\rho^2 = \omega^2 \mu\varepsilon \tag{2.23}$$

The boundary condition for cylindrical waveguide requires that the tangential electric field, E_z and E_φ, be zero at the walls, ie: at $\rho = a$, the waveguide radius. This boundary condition is satisfied when $J_m(k_\rho a) = 0$, requiring that:

$$k_\rho = \chi_{mn} / a \tag{2.24}$$

where χ_{mn} is the nth root of the Bessel function of the mth order, such that $J_m(\chi_{mn}) = 0$.
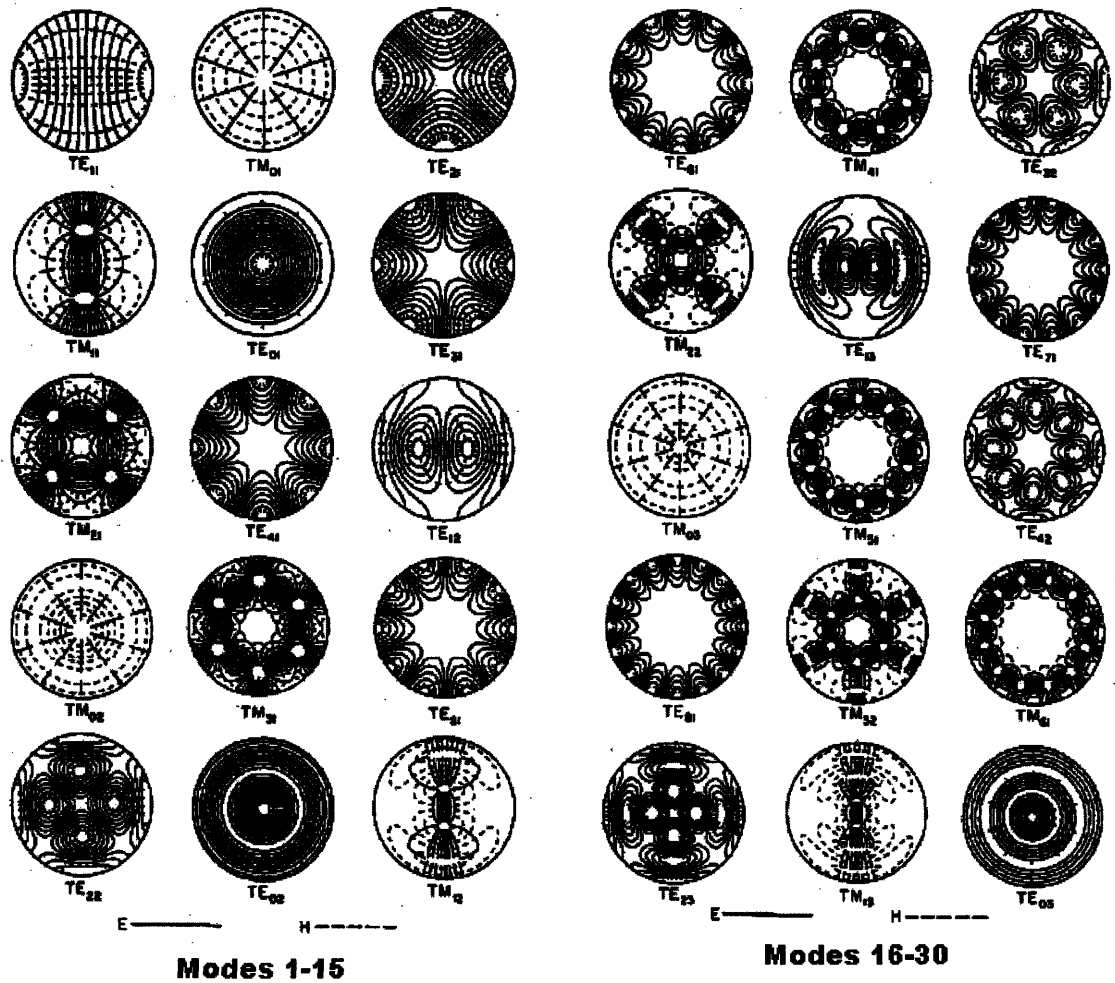
Figure 2-1: First 30 modes in a circular cylindrical waveguide [14]

Unlike with rectangular waveguides, the boundary condition for TE modes in cylindrical waveguide differs from that for the TM modes. The TE boundary condition requires

28

that $J'_m(k_\rho R) = 0$, relying instead on the derivative of the Bessel function and its corresponding set of zeros, χ'_{mn}. The best way to find the zeros of the Bessel functions and their derivatives is to simply look the values up in one of the readily available tables. A quick perusal of these tables shows that χ'_{11} is the smallest number, meaning that the lowest order mode in a cylindrical waveguide is the TE$_{11}$ mode. The field pattern of the 30 lowest order modes in a cylindrical waveguide can be seen in Figure 2-1.

2.1.4   Wall Losses

Thus far, it has been assumed that the waveguide walls are perfectly conducting; however, in reality, metallic walls will have a large, but finite, conductivity. In order for this to be a factor, we must introduce one concept key to waveguide propagation that has not been discussed to this point, and that is the concept of surface currents along the walls of the waveguide.

The presence of surface currents is derived from the boundary conditions. Considering a parallel plate waveguide with conducting walls, there will be a surface current such that:

$$\vec{J}_s = \hat{n} \times \vec{H}_{wall} \qquad (2.25)$$

When the walls have a finite conductivity, there exists a finite tangential electric field at the walls (for a perfect conductor, this is identically zero):

$$\vec{E}_{wall} = \sqrt{\frac{\omega\mu}{j\sigma}} \hat{n} \times \vec{H}_{wall} \qquad (2.26)$$

where the conductivity σ is assumed to be large. There is therefore a time-average Poynting power density flow into the conductor [13]:

$$P = \frac{1}{2}\text{Re}\left\{-\hat{n} \cdot \left\langle \vec{E}_{wall} \times \vec{H}^*_{wall} \right\rangle\right\} = \frac{1}{2}\sqrt{\frac{\omega\mu}{2\sigma}}\left|\vec{H}_{wall}\right|^2 \qquad (2.27)$$

The result of this is an exponential attenuation in the power propagating through the line, which is typically measured in dB/m or dB/km.

We can also consider the wall losses in another, perhaps more intuitive way. If we consider the modes of a rectangular waveguide, each is simply a sinusoidal function, in

order to satisfy the boundary conditions. The *sin* and *cos* functions can each be decomposed into a pair of complex exponentials. Rather than viewing the fields inside the waveguide as a propagating mode, we can instead consider the fields as a sum of plane waves, one of which is propagating in the forward direction, and another of which is propagating in the reverse direction. Based on the propagation constant of the mode, these plane waves are incident on the walls of the waveguide at a particular angle. In the case where the walls are perfectly conducting, the plane wave encounters a lossless bounce; however, if the walls have a finite conductivity, then each bounce will have an associated loss.

This wall loss is often referred to as Ohmic loss since it is a result of the non-zero resistance, i.e. finite conductivity, of the waveguide walls. In a typical cylindrical waveguide, the Ohmic loss is a factor of the mode being used and the waveguide radius. Typically, this Ohmic loss is minimized by selecting a mode whose electric field is minimal along the waveguide walls and one that is far from cutoff with a shallow bounce angle. If the radius is increased, then the distance between bounces also increases and thus the Ohmic loss is reduced.

2.1.5   Corrugated Waveguide

Thus far, only smooth-wall metallic waveguide has been covered, however often times, other types of waveguide are preferred, such as waveguide with dielectric walls or metallic waveguide with corrugated walls. A corrugated waveguide is a smooth wall waveguide with periodic slots of a particular depth and width. Thus along the direction of propagation, the waveguide walls essentially appear to be a square wave. The radius of the waveguide is taken to be the inner radius, i.e. the top surface of the ridges between the slots.

In a corrugated waveguide whose diameter $2a$ is large compared to the wavelength λ and whose corrugation period P is small compared to λ, the wall begins to look like a surface with an anisotropic reactance:

$$Z_\varphi = E_\varphi / H_z = 0 \tag{2.28}$$

$$Z_z = -E_z / H_\varphi \approx j\sqrt{\frac{\mu_0}{\varepsilon_0}}(w/P)\tan kd = j\sqrt{\frac{\mu_0}{\varepsilon_0}}Z \tag{2.29}$$

where w is the corrugation width, d is the corrugation depth, and the free space propagation constant is $k = 2\pi/\lambda$ [15]. With this non-zero wall reactance, modes propagating in the waveguide will generally require both a TM and TE component; that is to say that a wave propagating in the z direction requires both E_z and H_z. The exceptions to this are the TE$_{0n}$ modes who have neither E_z nor H_φ, and thus are unaffected by the wall reactance, and TM$_{0n}$ modes which can still exist without an H_z component.

To characterize the modes that propagate within a corrugated waveguide, we introduce a parameter d_n reflecting the ratio of the TE and TM components present within the mode of the corrugated guide and requiring $E_\varphi = 0$ from Eqn (2.28):

$$d_n = \frac{pJ_p(X_n)}{X_n J'_p(X_n)}, p \neq 0 \tag{2.30}$$

$$d_n = 1, (\text{TE}_{0n}) \tag{2.31}$$

$$d_n = \frac{J_0(X_n)}{X_n J'_0(X_n)}, (\text{TM}_{0n}) \tag{2.32}$$

which must also satisfy the boundary condition from Eqn (2.29), therefore:

$$\frac{1}{d_n} - d_n\left[1 - (X_n/ka)^2\right] + \frac{X_n^2}{pkaZ} = 0, p \neq 0 \tag{2.33}$$

$$\frac{1}{d_n} + \frac{X_n^2}{kaZ} = 0, (\text{TM}_{0n}) \tag{2.34}$$

and as previously indicated, the TE$_{0n}$ modes are unaffected by this requirement.

The above equations parallel a dispersion relation for the roots X_n [15]. Starting with a mode in a smooth wall waveguide, Z can be varied to determine the deviation of the roots X_n from the roots in the smooth wall waveguide X_{n0}:

$$X_n = X_{n0} - \frac{\left[1 - (X_{n0}/ka)^2\right]p^2 kaZ}{X_{n0}\left(X_{n0}^2 - p^2\right)}, \text{(TE}_{pn})$$ (2.35)

$$X_n = X_{n0} - \frac{kaZ}{X_{n0}}, \text{(TM}_{pn})$$ (2.36)

For the case of TE$_{p1}$ and TM$_{01}$ modes, the roots become imaginary as Z increases and thus become surface waves within the corrugated waveguide and thus are not supported for normal propagation.

As discussed before, TE$_{0n}$ modes are unaffected by the change in wall reactance, therefore all of these modes are supported in a corrugated guide and have the same propagation constant.

For all other modes, we consider the limit as Z approaches infinity, and the assumption that X_n is much smaller than ka; therefore, $d_n^2 \approx 1$ and we have for $p \neq 0$:

$$\mp \sqrt{1 - (X_n/ka)^2} \approx \frac{1}{d_n} = \frac{1 - \dfrac{J_{p+1}(X_n)}{J_{p-1}(X_n)}}{1 + \dfrac{J_{p+1}(X_n)}{J_{p-1}(X_n)}}$$ (2.37)

The modes that satisfy this equation are called hybrid modes since they have both longitudinal electric and magnetic field components. For $d_m \approx -1$, the modes are labeled HE, and for $d_m \approx +1$, the modes are labeled EH, and are defined as follows:

$$J_{p-1}(X_n) \approx 0, \text{(HE}_{pn})$$ (2.38)

$$J_{p+1}(X_n) \approx 0, \text{(EH}_{pn})$$ (2.39)

These are defined such that TM smooth wall waveguide modes result in HE corrugated waveguide modes, while TE smooth wall waveguide modes result in EH corrugated waveguide modes.

32

Corrugated waveguide also supports the propagation of TM_{0n} modes for $n \neq 1$, however unlike in the TE_{0n} case, the wall reactance has an effect on the roots, and TM_{0n} modes end up sharing the same root as $TE_{0(n-1)}$ modes:

$$J_0'(X_n) = -J_1(X_n) \approx 0 \qquad (2.40)$$

Reviewing the table of Bessel roots, the lowest order mode in a corrugated waveguide is shown to be the HE_{11} mode. The advantage of using corrugated waveguides is the lower loss associated with them. The HE_{11} mode in corrugated waveguide exhibits significantly less loss than the mode with the lowest loss in smooth wall waveguide which is the TE_{01} mode. The HE_{11} mode can be thought of approximately as a mode mix containing 85% TE_{11} and 15% TM_{11}[16].

On top of being able to propagate a lower loss mode than smooth wall waveguide, corrugated waveguide also has many engineering possibilities with regards to the line itself. The surface in a corrugated waveguide that contributes the most attenuation is the front face of the ridges, which means that the reactance could be further reduced if the corrugations were rounded [17]. Another possibility for corrugated waveguide is to explore periodic loading, i.e. inserting dielectric or ferrimagnetic material in the slots [18].

2.2 Losses in Transmission Lines

The design of transmission line systems for real world applications is subject to a number of considerations. While the frequency is likely already specified by the particular application; the size, shape, and type of waveguide, as well as the mode, can be chosen to accommodate the design requirements. Also, real transmission lines are rarely just a long straight section of waveguide. Due to space limitations, components such as miter bends, i.e. 90° bends, are often required. Other specifications on the line may require the use of polarizers and other components.

In general, when it comes to setting up a transmission line, there is a tradeoff between two primary options and the choice is dependant on the application. One option is to use fundamental waveguide, meaning that the size of the waveguide is selected such that only one mode can propagate at the frequency of interest. In fundamental guide, there is no concern with mode conversion and the waveguide can change direction freely without any distortion of the signal. The downfall with using fundamental waveguide is that the Ohmic loss will be quite large; therefore when power loss is a concern or if dealing with a high power application, an alternative is required. This alternative is the use of large, overmoded waveguide. As previously mentioned, the HE_{11} mode in corrugated waveguides exhibits the lowest loss. Therefore when maximum transmission is desired or when worries of line heating arise due to the amount of power being transmitted, the ideal choice is a very large overmoded waveguide [19] propagating a hybrid mode [20]. The downfall of using large overmoded transmission lines is that there can be substantial mode conversion introduced by imperfections of the line or by various transmission line components. In the context of the work in this thesis, we are interested in transmission lines for high power applications such as ITER's ECH system, therefore only the losses in large overmoded transmission line systems will be discussed.

The ITER ECH line is designed to have minimal losses, therefore it is constructed with corrugated waveguide propagating the HE_{11} mode. The 63.5 mm diameter guide is highly overmoded, with $a/\lambda \sim 18$ for the 170 GHz power being transmitted. For most applications, there is no possibility of constructing a transmission line purely from straight sections of waveguide, thus components like miter bends that change the direction of propagation are often necessary. If an overmoded transmission line consisted only of sections of straight waveguide and quasi-optic waveguide miter bends with mirrors, the loss in the straight sections is negligible if the transmission line is constructed with sufficiently small tilt, offset and sag errors [21], and thus the mode conversion loss due to diffraction in the miter bend is the primary source of loss in the transmission line. This is illustrated in Table 2.1 where two separate loss estimates are shown for the ITER ECH transmission line.

Since standard miter bends can have relatively high losses, several efforts have been undertaken to reduce the losses of miter bends by either altering them or by considering

34

other components. Gradual waveguide bends may seem like an enticing option due to the significantly reduced mode conversion loss, however the required length of such a bend to significantly decrease the loss renders them impractical for large overmoded waveguide [22]. Another way of reducing the loss in miter bends that has been floating around for years is the use of phase correcting mirrors [23], however there are a number of concerns with how such components would function in a real system. Despite these efforts, the latest design of the ITER ECH system still calls for the use of standard miter bends, though the possibility of implementing improved miter bends still remains. Since the miter bends are the largest source of loss in the transmission line, a major part of determining the overall loss in a transmission line boils down to evaluating the loss in the miter bends, therefore it is important to have a theory allowing for calculation of this loss.

Losses	ITER DDD 5.2	MIT Estimate
MOU loss	0.22 dB	−
Injection loss		
Coupling loss, Tilt, Offset	0.035 dB	0.116 dB
Intrinsic loss		
Miter bends	0.248 dB	0.19 dB
Polarizers	0.044 dB	0.066 dB
Extrinsic loss		
WG Sag	0.078 dB	0.039 dB
WG Tilt/Offset		0.036 dB
Other loss	0.025 dB	0.043 dB
Total loss	**0.65 dB (14%)**	**0.49 dB (11%)**
Loss without MOU loss	**0.43 dB (10%)**	**0.49 dB (11%)**

Table 2.1: Table of estimated losses for the ITER ECH transmission line [24]

2.3 Loss Theory for Miter Bends

As established in the previous section, the miter bend is a major source of losses in transmission lines. Due to the geometry of the miter bend, solving for the fields and the losses in a miter bend is no trivial task. As a result, current miter bend loss estimates are derived from a simpler geometry that omits much of the asymmetry present in the miter bend problem.

The first work done to derive an expression for the mode conversion loss in a miter bend was based on a geometry involving the crossing of two waveguides, also equivalent to joining two miter bends back-to-back along their mirror planes [25]. The approach taken was to reduce the three dimensional boundary value problem to a couple of two dimensional ones. The result was obtained by assuming a TE_{01} input into one arm of the structure and then calculating the power in each TE_{0n} mode in the arm directly opposite the input. A two dimensional waveguide cross was also considered for non-90° bends [26], which was elaborated on further for the 90° case [27] and again for the rectangular geometry [28]. The mode conversion loss was derived using a combination of diffraction theory in open systems and ordinary waveguide wave theory. The nature of this loss was also discussed later, asserting that half of the lost power is transmitted in the form of a broad spectrum of low-order unwanted spurious modes, while one quarter travels backward in the form of several high-order spurious waves close to cutoff, and an equal fraction goes forward in the form of similar modes [29]. The result of these works agreed reasonably well with experimental results [30], though it is the later work of Doane and Moeller [31] that improved on the previous theoretical results and is the current standard for estimating miter bend losses. The details of this theory now follow.

The theory work in [31] takes a slightly different approach than the other works listed above. While in the majority of the other cases, a smooth wall TE_{01} waveguide cross was considered, this later work considers a geometry of a simple gap between two sections of corrugated waveguide designed for propagating the HE_{11} mode. Figure 2-2 shows how this gap geometry resembles that of a miter bend. While the theory can be done for a gap of any length, it is clear that for the miter bend, we need only consider the

case for a gap length $L = 2a$, where a is the miter bend waveguide radius. Because of the geometry under consideration in this theory, we herein refer to this work as gap theory.
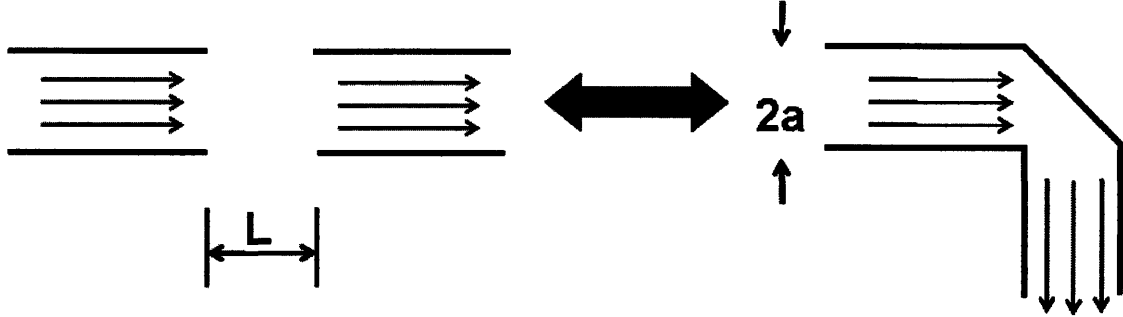
Figure 2-2: Comparison between the miter bend geometry and the waveguide gap geometry

Assuming a HE_{1m} mode propagating in the first waveguide, the linear polarized field at the aperture will be:

$$E = \frac{A_m}{\sqrt{R_m}} \frac{J_0(\chi_m r/a)}{a J_1(\chi_m)}$$
(2.41)

where A_m is the amplitude and R_m is the normalized propagation constant:

$$R_m \equiv \frac{\beta_m}{k} = \sqrt{1 - (\chi_m/ka)^2}$$
(2.42)

with k being the free space propagation constant, and χ_m the Bessel roots such that $J_0(\chi_m) = 0$.

The fields in the gap between waveguides can be written as:

$$E = \int_0^\infty A(\gamma) J_0(\gamma r) e^{-jz\sqrt{k^2 - \gamma^2}} d\gamma$$
(2.43)

and the field at the aperture of the second waveguide is decomposed into HE_{1n} modes:

$$E = \sum_n \frac{B_n}{\sqrt{R_n}} \frac{J_0(\chi_n r/a)}{a J_1(\chi_n)} e^{-jkR_n(2a)}$$
(2.44)

We recognize that to solve this problem, we simply equate Eqn (2.43) to Eqn (2.41) for $z = 0$ and to Eqn (2.44) for $z = 2a$. The first equality can be solved by considering the form of the Hankel transform to solve for the amplitudes $A(\gamma)$. The coefficients B_n can

37

then be solved in terms of *A(γ)* using the second equality. Thus the scattering coefficients S_{nm}, the ratio of the amplitude B_n at the output to the amplitude A_n at the input, can be obtained, which, assuming that *ka* is large compared to χ_n and $x \cong \gamma a$, can be written as:

$$S_{nm} \equiv \frac{B_n}{A_m} = 2\chi_n\chi_m\sqrt{\frac{R_n}{R_m}}\int_0^\infty \frac{xJ_0^2(x)\exp\left[j2a(x^2 - \chi_n^2)/(2ka^2)\right]}{(x^2 - \chi_n^2)(x^2 - \chi_m^2)}dx \qquad (2.45)$$

This integral can only be evaluated numerically; however, in [31], an approximate evaluation was obtained to provide a simple expression for determining the loss across the gap. The mode conversion loss is the difference in the power in the first waveguide, assumed to be unity, and the power in the input mode within the second waveguide. The mode conversion loss in a gap is:

$$0.0676\chi_1^2\left(\frac{a}{\lambda}\right)^{-3/2} \qquad (2.46)$$

where χ_1 = 2.405 for the HE$_{11}$ mode and 3.832 for the TE$_{01}$ mode. Thus, we have a relatively simple equation to determine the loss of a miter bend which only depends on the mode being propagated and the size of the waveguide relative to the frequency of the power.

What has not been discussed thus far is how this result determines the mode conversion losses in the miter bend. While similar, there are some obvious discrepancies between the two geometries. The generally accepted argument for comparing the losses in the waveguide gap to the losses in the miter bend goes as follows: if one were to imagine the walls of the waveguide continuing into the gap region to the location of the miter bend mirror, then diffraction would be eliminated in one of two planes, and thus the losses should be divided by a factor of two. Thus the loss in a miter bend is:

$$0.496\left(\frac{a}{\lambda}\right)^{-3/2} \qquad (2.47)$$

for the TE$_{01}$ mode, and:

$$0.196\left(\frac{a}{\lambda}\right)^{-3/2} \qquad (2.48)$$

for the HE$_{11}$ mode.

There is also the issue of how the mode converted power is distributed. By evaluating the mode content in the second waveguide in higher order HE_{1n} modes using Eqn (2.45), the results roughly agree with previous assertions that one half of the diffracted power should be in low order modes.

While agreement has been reasonable between the gap theory, the previous theory work, and experimental results [32], we must still acknowledge that these theories do have some shortcomings. None of the work thus far has considered asymmetric modes nor have situations been considered where all the power must be accounted for either in higher order modes at the output or reflected power at the input, therefore assessments of the mode distribution should be looked upon with a degree of skepticism. Even the total mode conversion loss values may not be perfectly correct since accurate measurements of such small losses at microwave frequencies are no easy task, thus it is difficult to attribute differences of 10, 20 or 30% between theory and experiment to problems within the theory.

Chapter 3

Numerical Simulation of Transmission Line Losses

In Chapter 2, the handling of how losses are calculated in a complete transmission line system was discussed and it was revealed that miter bends are a major contributor to the system's overall loss. A theory for calculating the losses in a miter bend was also presented. This theory has proven to agree reasonably well with experimental results; however the agreement is rarely perfect. While the burden of doubt is often placed on problems with experimental setups or difficulties in obtaining accurate measurements, it is not unreasonable to conceive that there are issues with the theory itself. The gap theory is widely accepted, though it requires that several assumptions are made to relate the result to that for an actual miter bend and it never truly considers the asymmetries present in the miter bend geometry.

Since it is not necessarily realistic to obtain a full analytic solution to the miter bend geometry and results based on gap theory may not be completely accurate, one option for obtaining a solution to the full miter bend problem is to use a numerical simulation code. One such code that is designed for the simulation of high frequency structures is Ansoft's HFSS.

HFSS is a finite element method code with a built-in eigenmode matrix solver. This means that the code can solve for the structure's modes and then return results in a scattering matrix that outlines transmission, reflection, and mode conversion coefficients, which is particularly useful for the study of waveguides. The accuracy of HFSS solutions depends on the size of the tetrahedral mesh with respect to the wavelength at the frequency being solved for. If the tetrahedra are too large, then the solution will not converge adequately. However, the number of tetrahedra is directly proportional to the

necessary computing resources to solve the problem, which can limit the ability to solve a problem that has a very large volume relative to the wavelength of interest.

For very low values of a/λ, the miter bend geometry can be solved with HFSS using a standard computer having only 2 GB of RAM, however our goal is to be able to determine the losses for larger overmoded miter bends such as those needed for ITER, $a/\lambda \sim$ 18, for which the resource demands are far too great. In order to obtain a loss estimate for the ITER miter bends, an alternative approach is required.

While the accuracy of the gap theory is not guaranteed, it is also not necessarily incorrect. Therefore, one way to obtain a proper loss estimate for ITER miter bends is to validate the gap theory itself or to make any necessary improvements. Validating the gap theory involves two main tasks: verifying that the analytical expression for loss across a waveguide gap is correct and verifying that the assumptions relating the result in a gap to the loss in a miter bend are correct.

3.1   Simulating the Waveguide Gap Problem

When using simulations to solve a problem, it is important to simplify the problem as much as possible.

The first aspect to take note of is that the ITER miter bends are corrugated and propagate the HE_{11} mode. This creates a problem since the HFSS eigenmode solver only considers TE and TM modes, even if the corrugated waveguide is modeled correctly. In order to get around this problem, a smooth wall waveguide propagating the TE_{01} mode can be considered instead. The gap theory is equally valid for the TE_{01} smooth wall waveguide case and the HE_{11} corrugated waveguide since both modes retain the same symmetry. The only difference is the change in the value of the Bessel zero, and the applicability of both cases is covered in [31]. A comparison of the field patterns for both modes is shown in Figure 3-1. The symmetry shared by each mode is apparent.
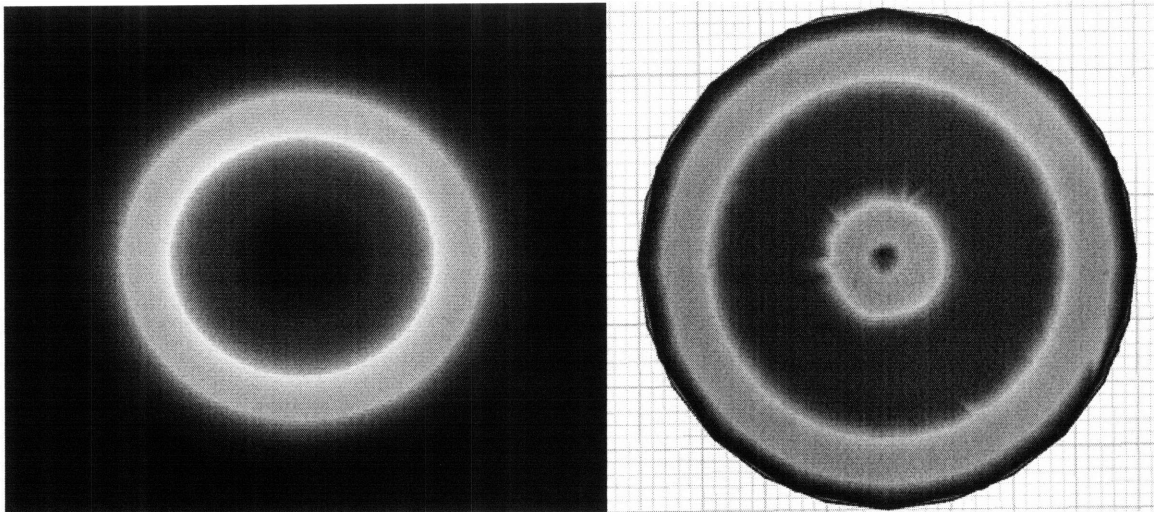
Figure 3-1: Comparison of the field patterns for the HE$_{11}$ mode (left) and the TE$_{01}$ mode (right)

The next issue to tackle is the size of the problem. It was previously mentioned how the miter bend is too large to solve even for moderate values of a/λ; however, the waveguide gap geometry is actually larger than the miter bend. The advantage of simulating the waveguide gap instead of the miter bend is that the gap problem has an axial symmetry about the center of the waveguide. While the miter bend can only be divided in half to retain the integrity of the initial problem, it is only necessary to simulate a small wedge of the gap geometry. This means that the volume of the gap problem can be reduced substantially so that higher values of a/λ can be simulated. The specifics of the TE$_{01}$ waveguide gap model are discussed next.

3.1.1 Modeling the TE$_{01}$ Gap

To obtain the simulation results in the scattering matrix form with HFSS, the driven modal solution is used, and waveport excitations are selected at the input and output apertures of the geometry. Waveports also allow the user to define the input in terms of the structure's modes to obtain plots of the electric fields within the structure. To account for the aforementioned axial symmetry, perfect E symmetry boundaries are used on the two sides of the wedge. When the electric field is normal to this symmetry plane, the

symmetry boundary assumes that the fields are mirrored across the boundary and thus no information is lost by only considering the given geometry.

Since it is the mode conversion loss that is of concern, rather than the Ohmic loss, the waveguide walls can be modeled using a perfect E boundary, which behaves like a perfect conductor. This allows for further simplification of the problem by neglecting the Ohmic loss.

The biggest difficulty in modeling the gap problem is developing a way to model the gap region itself, where the waves can propagate into free space. HFSS provides users with a radiation boundary that is supposed to absorb all fields incident upon it, and thus have zero reflection; however such a boundary is not perfect. If the radiation boundary is placed directly in line with the waveguide walls, it will still tend to somewhat confine the waves as if the conductor continued through the gap, rather than allowing the fields to expand as if in free space. In order to avoid such issues, the radiation boundary should be a small distance, on the order of a wavelength, away from the waveguide edge. At the same time, a larger radiation region means a larger volume that HFSS must solve and thus the required computing resources increase. Therefore, in order to minimize the resource requirements, a conical region is used to account for the fact that the expansion of the fields requires a larger radiation region towards the output side of the gap. The HFSS model to simulate the gap problem is shown in Figure 3-2.

When using HFSS, it is very important to parameterize the problem. Rather than using fixed dimensions, dimensions are entered as functions of a variable such as a, the waveguide radius, or λ, the wavelength. This allows the user to simply adjust the parameters and the model geometry will update itself accordingly for the new values, and it is especially useful in the case of the waveguide gap simulations since we are interested in solutions at different values of a/λ.

43
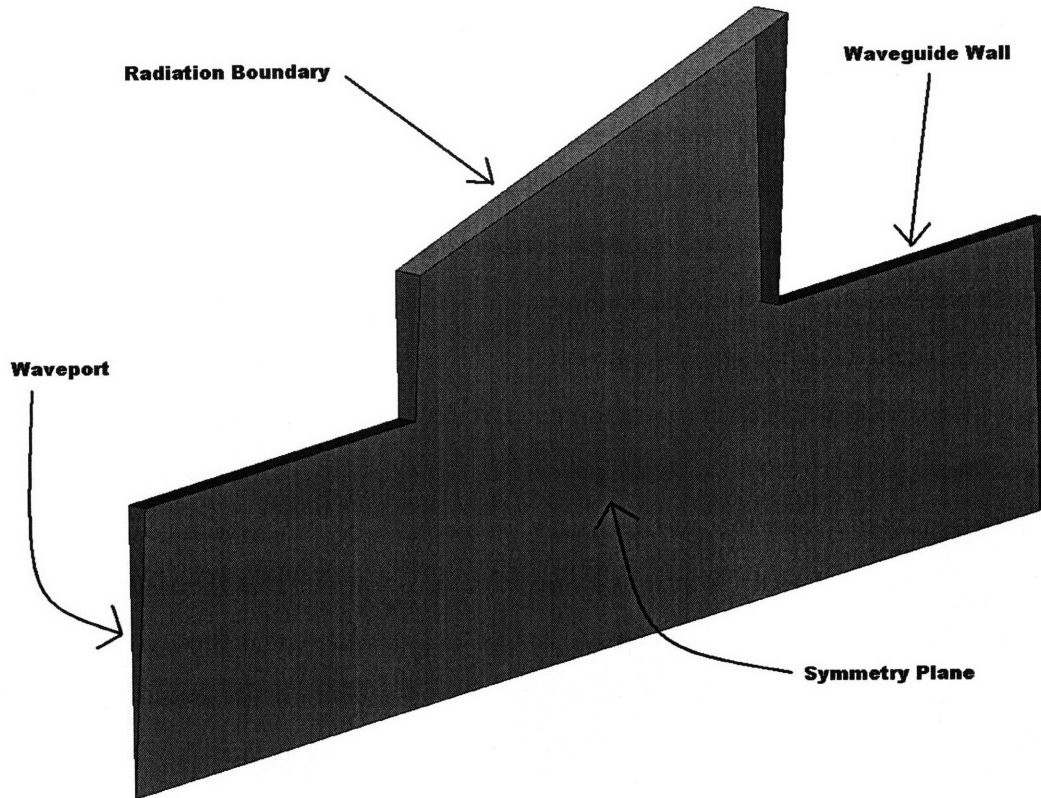
Figure 3-2: Diagram showing the geometry used to simulate the TE_{01} waveguide gap

3.1.2 TE_{01} Gap Results

To simulate the waveguide gap at a particular value of a/λ, the values of a or λ individually are irrelevant and the simulation results are unaffected provided that the ratio is the same. For consistency, the frequency was kept fixed at the ITER ECH value of 170 GHz with a corresponding wavelength of approximately 1.76 mm. The waveguide radius was then adjusted accordingly for a range of a/λ values.
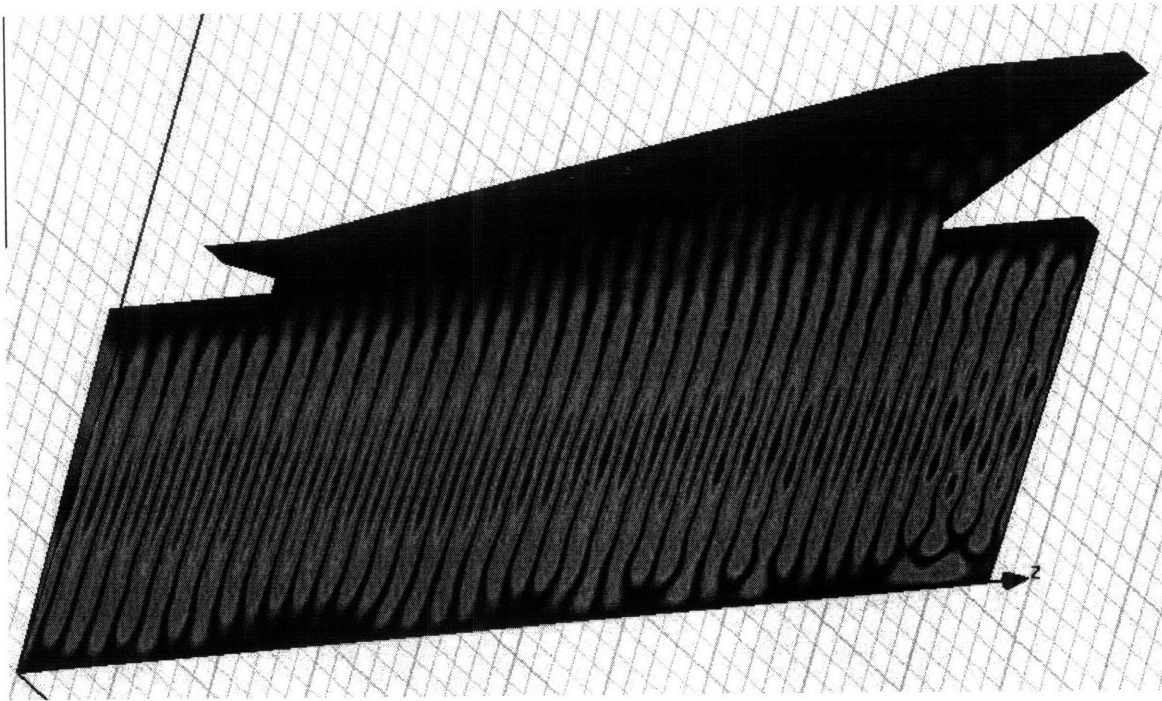
Figure 3-3: Plot of electric field magnitudes for the waveguide gap geometry with a/λ of 7

Figure 3-3 shows the magnitude of the fields within the gap model. The first thing we observe in the plot is the expansion of the fields as they propagate across the gap. In the gap geometry, it is this expansion that is the cause of the mode conversion. At the end of the first waveguide section, the fields are well confined within the waveguide radius. As the TE_{01} mode enters the gap, the mode is no longer confined by the waveguide's boundary conditions and there is some expansion out into free space. At the input of the second waveguide section, the field pattern is still similar to that of a pure TE_{01} mode, but it now has a tail with non-zero field magnitudes extending past the waveguide walls in the radial direction. As a result, some power will be lost, leaking out into the radiation boundary, which is noticeable in Figure 3-3. In these gap simulations, the waveguide is given a finite thickness; therefore, a small amount of power will also be reflected back towards the first waveguide due to the leading face of the waveguide. The rest of the power couples into the second waveguide where we also expect some further deformation of the field pattern due to diffraction along the edge of the waveguide.

The result is that the majority of the power reaches the output of the second waveguide section, though no longer as a pure TE_{01} mode. The amount of power in the

TE$_{01}$ mode at the output is plotted in Figure 3-4 for several values of a/λ, assuming unity input of a pure TE$_{01}$ mode. The theory curve that is plotted against the simulation result is the analytical expression from [31] which, for the TE$_{01}$ mode, is:

$$1 - 0.9925\left(\frac{a}{\lambda}\right)^{-\frac{3}{2}} \quad\quad (3.1)$$

The agreement between theory and simulation is quite good, showing that the gap theory correctly determines how much power in the input mode will transmit across the gap. It can be argued that the agreement is not great for low values of a/λ; however, this is not unexpected since the gap theory is simplified on the assumption that a/λ is large compared with the Bessel roots, and this assumption is weaker for low values of a/λ. We see that as a/λ increases, the power in the TE$_{01}$ mode at the output increases, which is due to a reduction in both the power lost into the gap as well as power lost to mode conversion. This result illustrates why large overmoded transmission lines are a popular option.
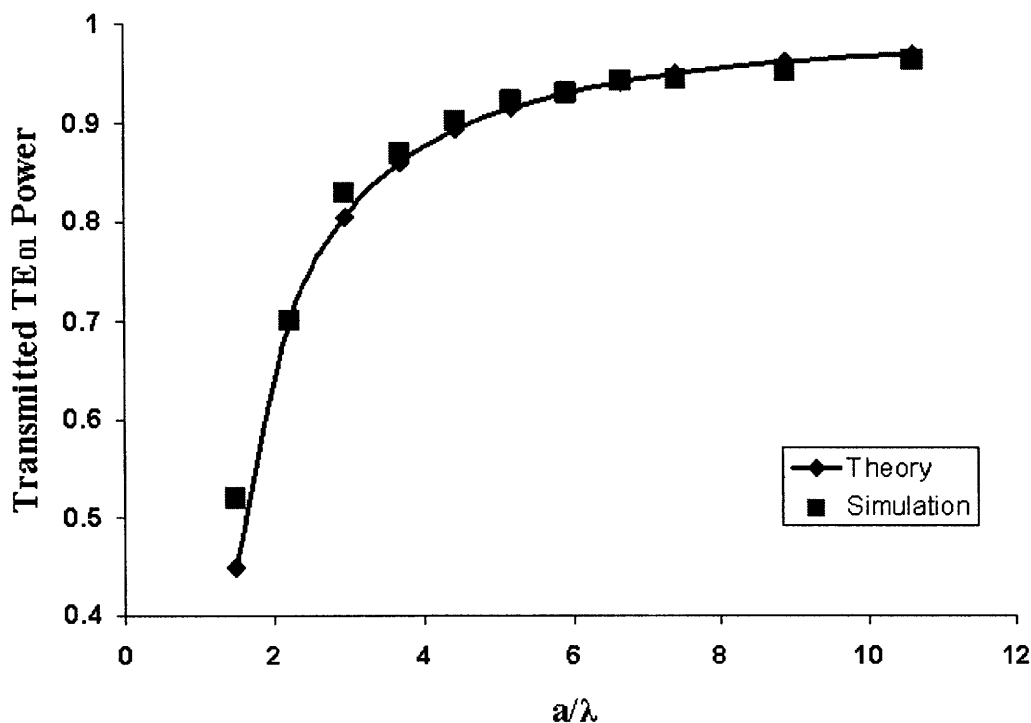
Figure 3-4: Transmission of the TE$_{01}$ mode across a smooth wall waveguide gap

90
80
70
60
50
40
30
20
10
0

% of Total Power Lost

0   2   4   6   8   10   12

a/λ
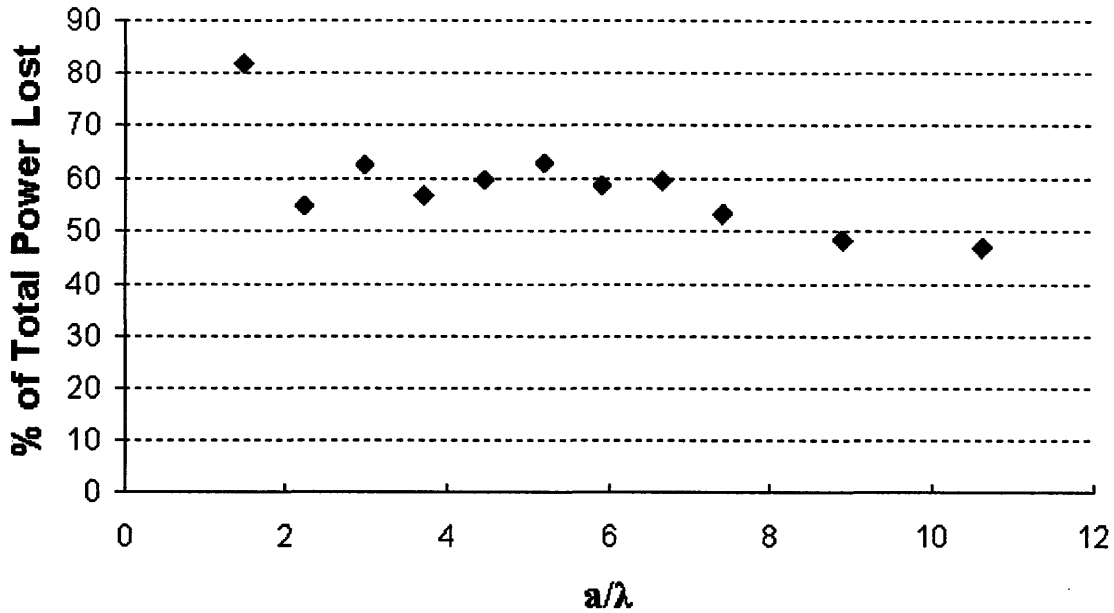
Figure 3-5: Percentage of power in high order modes (>TE$_{08}$) plus power radiating out of the gap with respect to the total TE$_{01}$ power lost

While the gap theory does seem to accurately predict the overall loss in TE$_{01}$ power, there still remains the issue of determining how the lost power is allocated. When estimating miter bend losses based on gap theory, the assumption is that half of the diffracted power is in low order modes, and then half of the remaining power is in higher order modes, with the rest of the power being reflected towards the input port. This is not entirely verifiable with the gap problem since the symmetry of the gap structure means that only TE$_{0n}$ modes are considered. In addition, the power that radiates out of the gap would not be able to do so in a miter bend; however, it could be assumed that, in the miter bend geometry, this power would be either reflected to the input port or found in high order modes at the output port. These assumptions are roughly verified by the result in Figure 3-5, where it can be seen that approximately half of the lost TE$_{01}$ power appears as mode conversion to high order modes and the other half appears as lower order modes, TE$_{02}$-TE$_{08}$, at the output. Figure 3-6 and Figure 3-7 look more closely at how the power is distributed into higher order modes at the output. We first notice that the concept of cutoff is quite apparent in each figure. As the waveguide radius increases, more modes
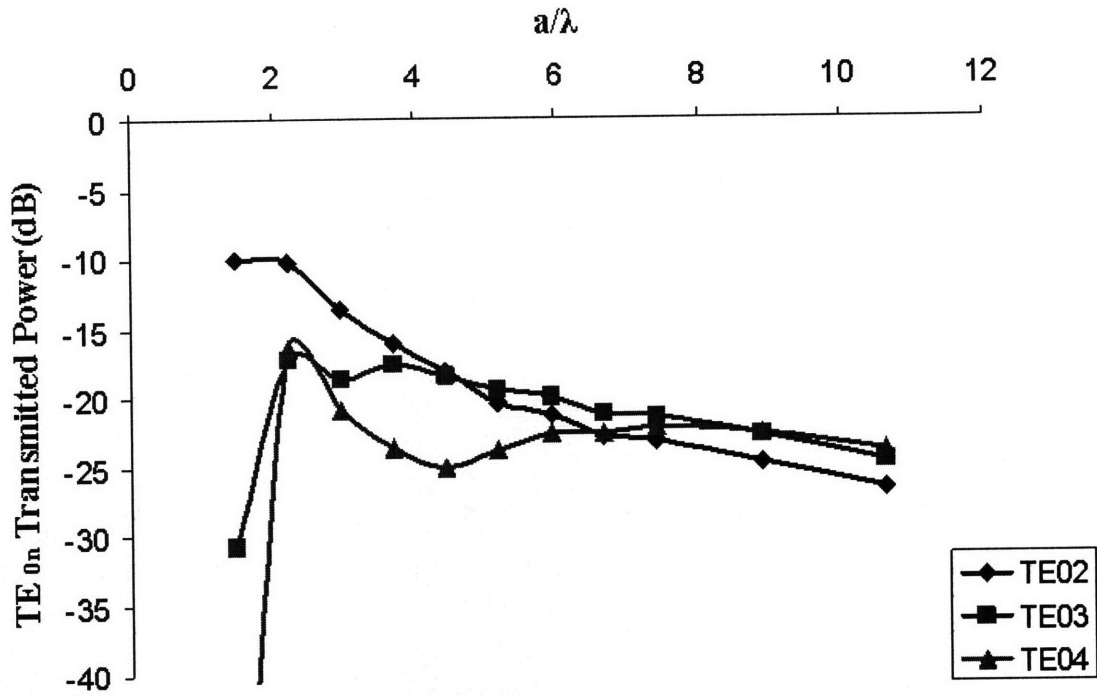
Figure 3-6: Mode conversion to low order modes across the waveguide gap
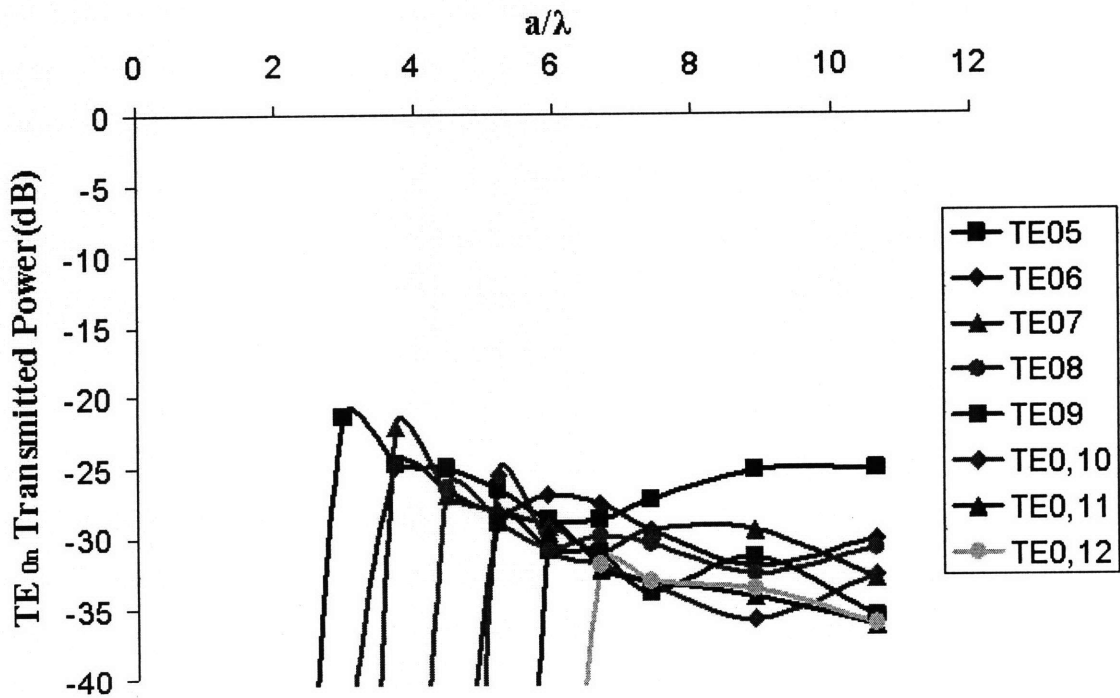
Figure 3-7: Mode conversion to high order modes across the waveguide gap

fall within the waveguide's cutoff. We also can see in the figures that the mode conversion to a particular higher order mode peaks right around that mode's cutoff. This is an interesting result, however for higher order modes, these peaked values are still less than the mode conversion to the relatively lower order modes. We see that only the lowest order modes, TE_{02} through TE_{04}, have as much as -20 dB mode conversion (1% power).

We can conclude that the theoretical expression for the loss across the gap is accurate and that the assumptions for the distribution of lost power are reasonable. However, in order to determine the actual nature of the mode conversion within the miter bend, the full problem should be solved.

3.2   Simulating the Smooth Wall Miter Bend

In order to properly make sense of the results of the waveguide gap simulations, we must also simulate the miter bend itself to view how the gap results correlate with the results for the miter bend at each a/λ. So while the excessive demand on computing resources prevents simulation of ITER sized miter bends, if the relationship between gap results and miter bend results can be determined at lower a/λ, then perhaps the expected result for large a/λ can be inferred.

3.2.1   Modeling the TE_{01} Miter Bend

The miter bend is actually an easier problem to model than the waveguide gap. The whole structure consists of waveguide therefore there is no need to include anything like radiation boundaries. Similar to the waveguide gap, waveports are used at the two ends of the miter bend so that simulation results are obtained in the proper form.

As previously mentioned, the waveguide gap has an axial symmetry, however only one proper symmetry plane that is normal to the wave propagation exists for the miter bend. The miter bend can then be split in half vertically and a perfect E symmetry plane is inserted along this face. In the case of the waveguide gap, all modes except TE_{0n} modes would violate the symmetry therefore only TE_{0n} modes were considered in the

49

simulations. In the case of the miter bend, the fields of all TE and TM modes satisfy the symmetry condition, with the exception of TM_{0n} modes. Similarly, if a perfect H symmetry plane was chosen instead, then all TE and TM modes with the exception of TE_{0n} modes would satisfy the symmetry condition. This is due to the orthogonality between the two sets of modes since one could interchange the magnetic and electric fields of a TE_{0n} mode and obtain a TM_{0n} mode. As a result, there is identically zero mode conversion to TM_{0n} modes for a miter bend with a TE_{01} input, which was verified by simulating a full miter bend. Another difference when solving the full miter bend is that there are two orthogonal versions of most waveguide modes, essentially each TE or TM mode appears twice where the second version is the same mode after undergoing a 90° rotation. However, simulations of the full miter bend showed that there was only mode conversion to one of each mode pair. Therefore, it is only necessary to simulate the half miter bend geometry in order to retain all the information that could be obtained from simulating the full miter bend.

3.2.2 TE_{01} Miter Bend Simulation Difficulties

It was already known that the increased volume of the miter bend geometry compared to that of the waveguide gap wedge would be a limiting factor to the values of a/λ that could be simulated with proper convergence. Therefore, there was no surprise when simulations would not converge adequately for a/λ of about 4-5. However, it turned out that computing resources were not the limiting factor for TE_{01} miter bend simulations using HFSS.

For both the waveguide gap and miter bend simulations, the driven modal solution is desired in order to obtain the results in scattering matrix form, requiring the use of waveports at each end of the structure. What has not been discussed thus far is the limitation of these waveport excitations. HFSS has a built-in cap on the number of modes that are considered by waveports, which is 25 for HFSS v10. Initially, HFSS v11 was supposed to increase this number to 99; however, this change was omitted in the final release, and the cap on waveport modes remains 25.

As previously mentioned, the waveguide gap problem only considers TE_{0n} modes due to the symmetry; therefore, even for a/λ values of 10, the structure still has only about 15 eigenmodes, i.e. TE_{01}-$TE_{0,15}$. In the case of the miter bend, all TE and TM modes with the exception of TM_{0n} modes are considered, and for a/λ values as low as about 1.7, the mode limit on waveports is already reached. To put this into perspective, the 3rd lowest order TE_{0n} mode, TE_{03}, is the 29th lowest order mode overall in circular waveguide, though this list includes 3 TM_{0n} modes as well.
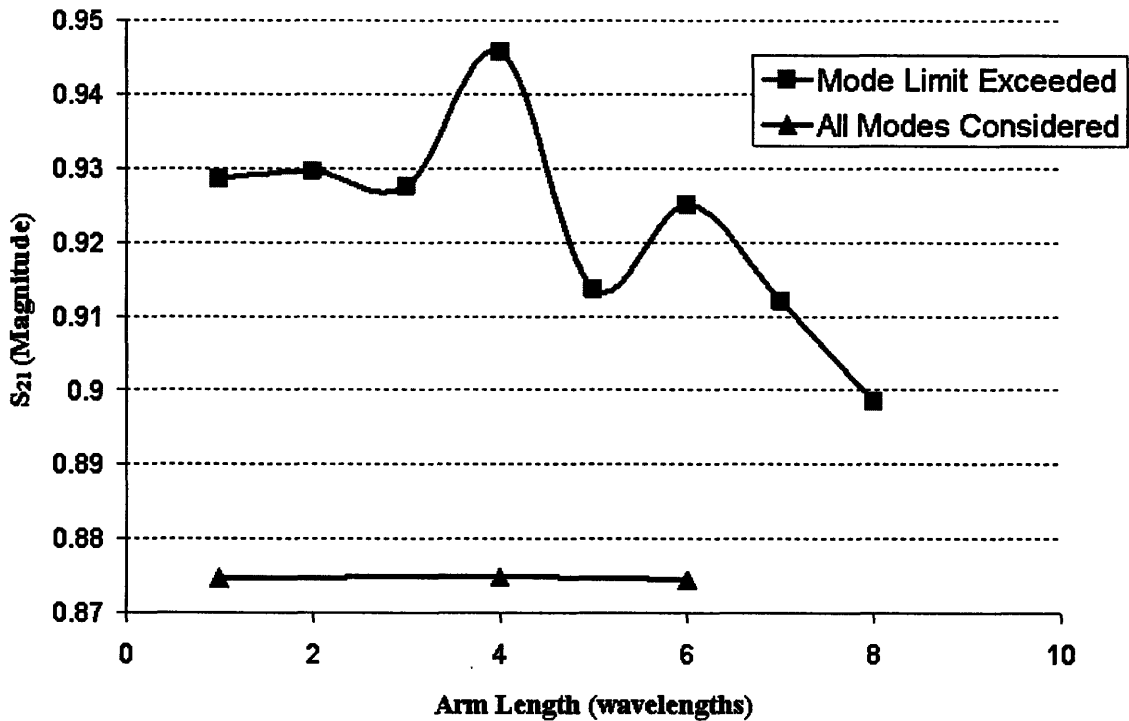
Figure 3-8: Magnitude of S_{21} (TE_{01} transmission) for two separate cases: all modes considered (a/$\lambda \sim$ 1.5) in blue, mode limit exceeded (a/$\lambda \sim$ 2.2) in red

While it is clear that the mode limit is reached in miter bend simulations, the question remains as to whether or not it will hamper the ability to obtain accurate results for higher values of a/λ. It could easily be argued that the mode conversion to the high order modes is quite small, and therefore the effect of omitting the majority of these high order modes is negligible. However, it turns out that this is not in fact the case. For low a/λ, where simulation results converge nicely and where relatively few modes are omitted, we find that the results are quite unreliable. Even though the simulation converges on a

solution, it doesn't necessarily mean that it is converging on the correct solution. This effect was discovered when simulations were run in which the length of the miter bend's arms were varied. Figure 3-8 shows the results of these simulations. For a value of a/λ where there are fewer than 25 eigenmodes, the S_{21} magnitude (equivalent to the square root of the transmitted TE_{01} power) remains relatively unchanged. On the other hand, for a value of a/λ where the waveport limitation forces the exclusion of modes within cutoff, we see that the S_{21} value can change quite a bit. With this variation of several percent, it makes it nearly impossible to draw any real conclusions with respect to the gap theory and the losses for an ITER sized miter bend. Nevertheless, results at low a/λ can still gain some information about the nature of the mode conversion in miter bends.
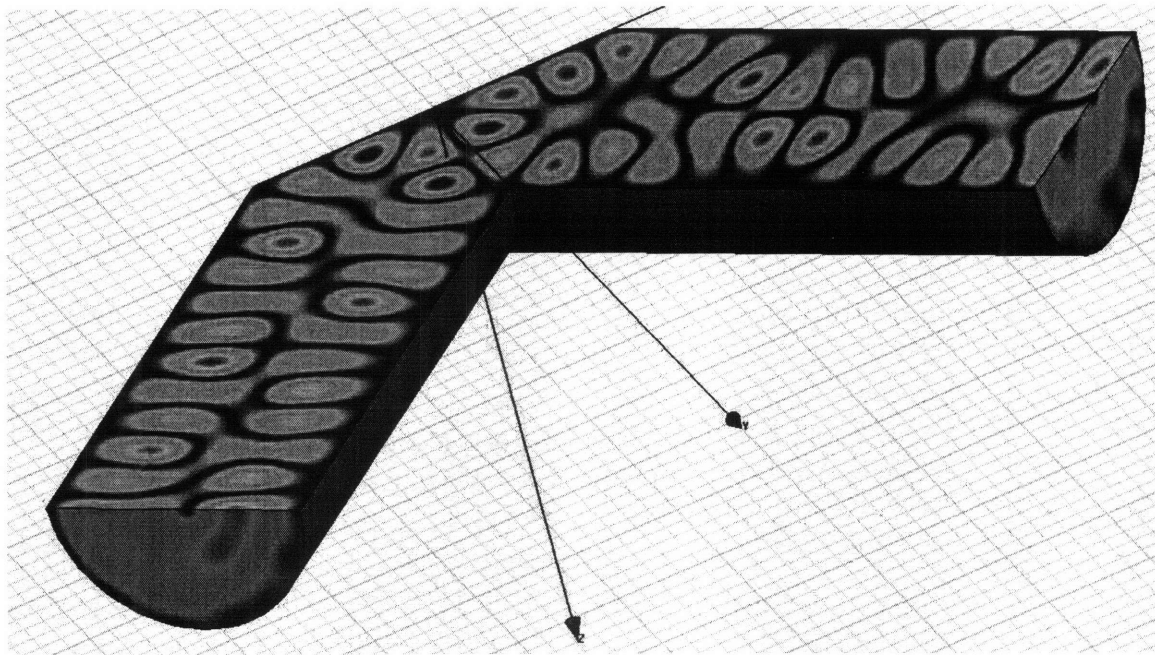
Figure 3-9: Electric field magnitude plot for the TE_{01} miter bend geometry with a/λ of 1.5

3.2.3 TE_{01} Miter Bend Results

As mentioned before, for a/λ greater than about 1.7, modes will be excluded and therefore the results cannot be accepted with any form of certainty. Thus the only TE_{01} miter bend results that will be covered are for $a/\lambda = 1.5$. A plot of the electric field magnitude within this half miter bend structure is shown in Figure 3-9. The problem with such a low value of a/λ is that there is significant mode conversion loss, which explains why the

TE_{01} mode is very difficult to distinguish in the arms and at the output port. Nevertheless, the TE_{01} mode is still dominant and that is the mode which the pattern most resembles. Table 3.1 shows the simulation results in more detail. The TE_{01} transmission is fairly close to the estimate based on the gap theory where we recall that the miter bend loss using gap theory is simply half the loss calculated for the gap, which is shown in Eqn (3.1). The table also shows the modes to which there is the most mode conversion, namely the TE_{02}, TE_{22}, and TE_{21} modes. This is a logical result since these are the lowest order modes that are most similar to the TE_{01} mode. It should be noted that the rest of the power was distributed more or less evenly in forward propagating and reflected modes, with approximately 0.3-0.4% power in each mode.

% Power at Output Port		
TE_{01} Transmission	**Simulated**	**73.2**
	Gap Theory	72.4
Mode Converted Power	**TE_{02}**	6.6
	TE_{22}	4.5
	TE_{21}	2.5

Table 3.1: Transmission and mode conversion in the TE_{01} miter bend with a/λ of 1.5

There was one other very interesting result that came out of the TE_{01} miter bend simulations. The modes of circular waveguide can be divided in to two types: modes with an even azimuthal mode number (TE_{0n}, TE_{2n}, TE_{4n}, etc.), and modes with an odd azimuthal mode number (TE_{1n}, TE_{3n}, TE_{5n}, etc.). We found that when a mode with an even azimuthal mode number is input to the miter bend, the amount of power in any of the modes with an odd azimuthal mode number is exactly the same at both the input port and the output port. The same applies to all the modes with an even azimuthal mode number when a mode with an odd azimuthal mode number is input. Thus for a TE_{01} input, if we see 0.36% power in the TE_{13} mode at the output, then we will see exactly 0.36% power in the TE_{13} mode at the input port. This behavior is a result of the symmetry of the miter bend, likely due to the boundary condition at the miter bend mirror. If the angle of the

bend was changed from 90° to 80° or 100°, then we would not see equal power in each mode at both apertures.

Therefore, even though the ability to do meaningful simulations of the TE_{01} miter bend is severely limited, some results providing information on the distribution of the mode converted power could still be obtained. There still remains one other option to derive some miter bend loss results using HFSS simulations, and that is to solve the HE_{11} corrugated miter bend.

3.3 HE_{11} Miter Bend

Simulating the HE_{11} miter bend is a little more difficult than the TE_{01} case. While a little more involved than a simple smooth wall miter bend, modeling the corrugated waveguide bend is still fairly straightforward. The main difficulty stems from the aforementioned fact that waveports won't solve for the hybrid modes within the corrugated geometry, requiring an alternate approach to excite the waveguide. The best solution to this problem is to use a Gaussian beam excitation. The correlation between the HE_{11} mode and a Gaussian beam is approximately 98%, thus the results should be similar. However, without waveports, the apertures of the miter bend must be defined to absorb all incident fields. Radiation boundaries were used for the TE_{01} gap problem, however for this application, the reflection could be problematic. HFSS provides another type of boundary which minimizes reflections even more than the radiation boundary, and that is the perfectly matched layer (PML). Another advantage of this Gaussian beam + PML approach is that it is less demanding on computing resources, thus better convergence can be achieved for higher values of a/λ compared to simulations using waveports.

When it comes to the results of simulating the corrugated miter bend, we must realize that they are only really useful on a qualitative level. The simulations are excellent for giving us an idea of what the field distribution looks like inside the miter bend, shown in Figure 3-10, however there is no easy way to deduce any quantitative results. While it is possible to use a mathematical code to convert the field profiles at the input and output of the bend to a distribution of modes, there is simply too much doubt about the accuracy of the fields to make any realistic assessment. Ignoring any inaccuracy that may be

introduced by the PMLs, the Gaussian beam excitation alone introduces an uncertainty of a couple percent.
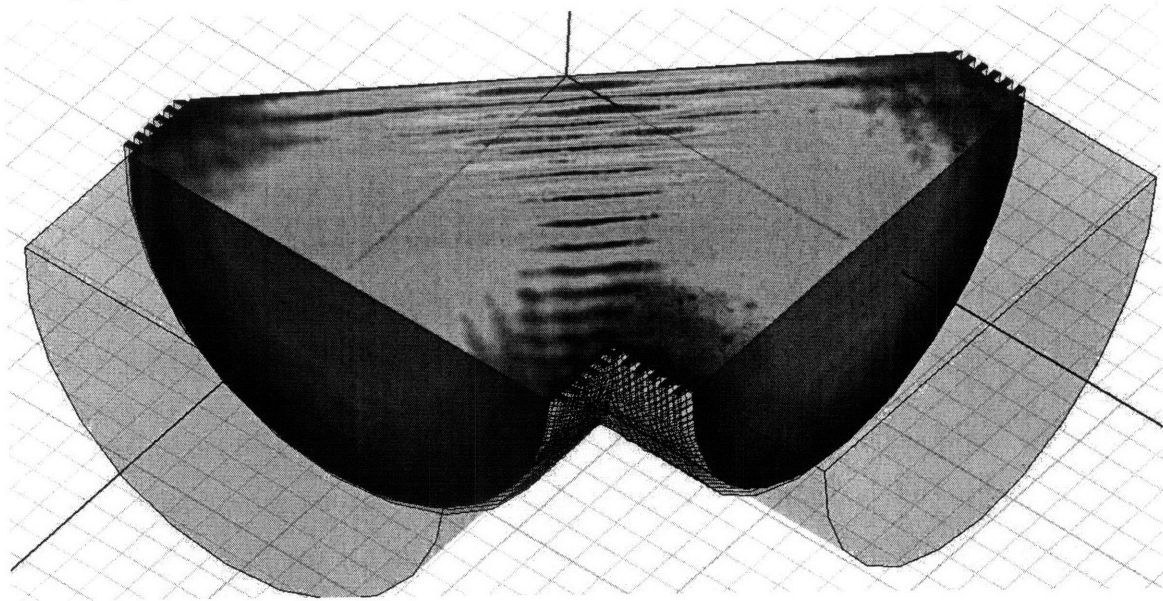
Figure 3-10: Electric field magnitude within the HE$_{11}$ miter bend geometry with a/λ of 4

3.4   Summary

We have verified that the analytic expression for the loss across a gap is accurate by simulating a smooth wall waveguide gap with a TE$_{01}$ input. The distribution of the lost TE$_{01}$ power across the gap is divided approximately evenly between power in relatively low order modes and power radiating out from the gap region. Due to limitations of the electromagnetic code, HFSS, the relevance of the gap result to the miter bend could not be verified. Nevertheless, some information was gained as to the nature of the mode conversion in TE$_{01}$ miter bends via simulation, showing that most mode converted power will appear in relatively low order modes that are symmetric or at least very similar to the input mode. While corrugated miter bend simulations may not be effective at putting numbers to the losses and mode conversion, they are useful to get an idea of the electric field distribution within the miter bend geometry with a HE$_{11}$ input.

Chapter 4

Losses in a Miter Bend with an Impure Input Mode

It has been mentioned several times that miter bends are major contributors to the overall losses in millimeter wave transmission lines. The gap theory for calculating mode conversion losses in miter bends was presented along with the results of HFSS simulations to verify the loss across a gap and to learn more about the nature of mode conversion in miter bends. While having such results is great, it fails to reflect the actual problem in the context of a real application. As is the case with nearly all theories, many problems that arise in real systems are simply omitted. Typically, things like impossibly small tolerances on fabrication, uneven temperature distributions, or material impurities can cause experimental results to diverge, sometimes significantly, from the theoretical predictions. In the case of miter bend losses there are also a number of factors that must be taken into consideration.

For a big project like ITER, an effort has been made to account for as many of these unpredictable factors as possible. The loss estimate shown in Chapter 2 for the ITER ECH system includes several losses that are not inherent to the components themselves, labeled as extrinsic loss. For example, mismatching of the apertures of the transmission line sections by even a few microns would introduce a loss that would not exist if the system was constructed absolutely perfectly. Perfect construction though is quite unlikely, and thus loss estimates for the transmission line include a small loss due to the tilt and offset of waveguide sections. Even something like the curvature of miter bend mirrors caused by focused heat dissipation resulting from Ohmic losses was something eventually put up for discussion by the ITER team. Though despite the care given to assessing all possibilities, there are invariably going to be aspects that get overlooked.

One glaring issue that has not received much consideration at all is the concept of how the losses in the miter bend could change if the input mode is not a pure HE_{11} mode.

The lack of attention to considering the effect of higher order modes (HOMs) at the input of a miter bend is not exclusive to ITER as no rigorous analysis has been shown anywhere trying to demonstrate any possible effects or to discount the need to consider the HOM content. Now, it should be mentioned that the above statement is not entirely true. A 16%/84% mixture of HE_{12} and HE_{11} has been considered for some time, since it is a good approximation of the TEM_{00} mode which can propagate through a miter bend with virtually no loss [33], however a complete formulation of the aforementioned problem has yet to be completed. This is despite the fact that it is known that a Gaussian beam from a gyrotron injected into a corrugated wave guide will exhibit a minimum of about 2 % HOM generation [34]. More realistically, the HOM content is often several percent, and can even exceed 10 %. As such, we will explore the effect of HOMs at the miter bend by using a numerical approach and by considering previously established analytical expressions.

4.1 Determining the Effect of HOMs on Miter Bend Losses through Numerical Simulation

In the previous chapter, when a numerical approach was needed, a commercial electromagnetic solver like HFSS was chosen. In this case, we are not particularly concerned with obtaining the complete solution that includes all asymmetric modes, i.e. it is sufficient to solve the problem in the context of other theoretical work pertaining to miter bend losses, and commercial solvers are typically quite slow to go along with the other downfalls discussed in Chapter 3, thus an alternative is desired. As a result, we opted to use an in-house code, developed by Michael Shapiro, to solve the mathematical formulation of this problem.

4.1.1   Formulation of the Numerical Code

To solve this problem, the numerical code should take an input in the form of a mode mix of a dominant HE_{11} mode combined with some amount of a parasitic higher order mode (HOM) such as HE_{12}. We must recognize that it is not purely the amplitude of the modes that is important, since their phases also need to be considered. This task can be simplified by combining the two phases into one parameter indicating the phase of the HE_{12} mode relative to the phase of the HE_{11} mode. This mode mix must then be propagated through a miter bend-like geometry. The list of such geometries includes the full miter bend, the waveguide gap, and the waveguide cross; however for this application we consider a different geometry. We introduce a geometry herein referred to as the improved gap. This improved gap geometry retains the main properties of the gap, in that we only consider the symmetric HE_{1n} modes, however the waveguide walls continue into the gap region. In Figure 4-1 we can see that the improved gap geometry is essentially equivalent to removing the mirror of the miter bend and rotating one of the miter bend arms by 90°. Thus the loss measured across the improved gap is the same as the mode conversion loss in the miter bend and there is no need to divide the loss by two like we would in the case of the simple gap. Therefore, the improved gap geometry eliminates the need for another assumption that may or may not be correct across the whole range of sizes, frequencies, modes, and types of waveguide.
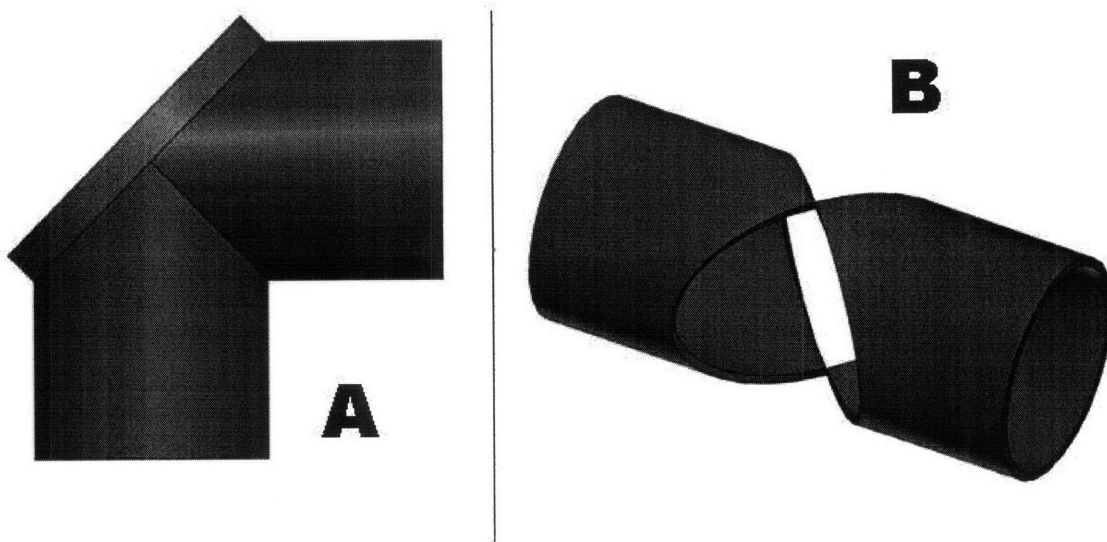

Figure 4-1: A - Top view of a miter bend, B – Improved gap geometry

We now consider the formulation of the problem for this numerical code. For these calculations, we consider the specific case of a parasitic HE_{12} mode, though we recognize that any mode could be selected.

We begin by writing the fields for the mode mixture:

$$E(r) = C_1 J_0\left(\frac{v_1}{a}r\right) + C_2 J_0\left(\frac{v_2}{a}r\right)\exp(j\varphi_{12}) \ , r \leq a \tag{4.1}$$

where C_1 is the amplitude of the HE_{11} mode, C_2 is the amplitude of the HE_{12} mode and φ_{12} is the relative phase. The Bessel function zeros are $v_1 = 2.405$ and $v_2 = 5.520$. We recognize that both modes are axially symmetric, therefore there is only an r dependence, and that the fields are confined within a waveguide of radius a, thus $E(r) = 0$ for $r > a$. The above fields are expressed in complex form, and for the purpose of calculations, it is preferable to express the fields as a real amplitude and phase:

$$A(x,y) = \sqrt{C_1^2 J_0^2\left(\frac{v_1}{a}r\right) + 2C_1 J_0\left(\frac{v_1}{a}r\right)C_2 J_0\left(\frac{v_2}{a}r\right)\cos(\varphi_{12}) + C_2^2 J_0^2\left(\frac{v_2}{a}r\right)} \tag{4.2}$$

$$\varphi(x,y) = \arctan\left(\frac{C_2 J_0\left(\frac{v_2}{a}r\right)\sin\varphi_{12}}{C_1 J_0\left(\frac{v_1}{a}r\right) + C_2 J_0\left(\frac{v_2}{a}r\right)\cos\varphi_{12}}\right) \tag{4.3}$$

where $r = \sqrt{x^2 + y^2}$ and $A(x,y) = 0$ for $r > a$.

The above array of amplitudes is placed within a larger square area with sides L. We can imagine this square zone as being a large metal box which now has a hole in the center where the above fields are contained. The fields within the metal region of this square will always be zero.

It is now convenient to represent the fields as a series of modes within this square box:

$$A(x,y)e^{j\varphi(x,y)} = \sum D_{pq}\sin\left(\frac{p\pi x}{L}\right)\sin\left(\frac{q\pi y}{L}\right) \tag{4.4}$$

where the coefficients D_{pq} are determined by applying a Fast Fourier Transform (FFT) to the fields.

Now we must consider how to propagate the fields from one end of the improved gap to the other. It is clear in Figure 4-1B that the waveguide walls are varying from cross-section to cross-section while crossing the gap. We therefore split the gap region into a finite number of steps and propagate the fields one step at a time. Figure 4-2 illustrates how the waveguide boundary changes as the gap region is crossed. We see that as the gap region is first entered, there is a small region on the side that is no longer confined by the waveguide. As we proceed further into the gap, this slot grows bigger and bigger until the halfway point where we could perceive a situation analogous to the waveguide cross in that there is a waveguide cutting through perpendicular to the direction of propagation. After the halfway point, the slot grows smaller until it is once again non-existent at the far end of the improved gap.
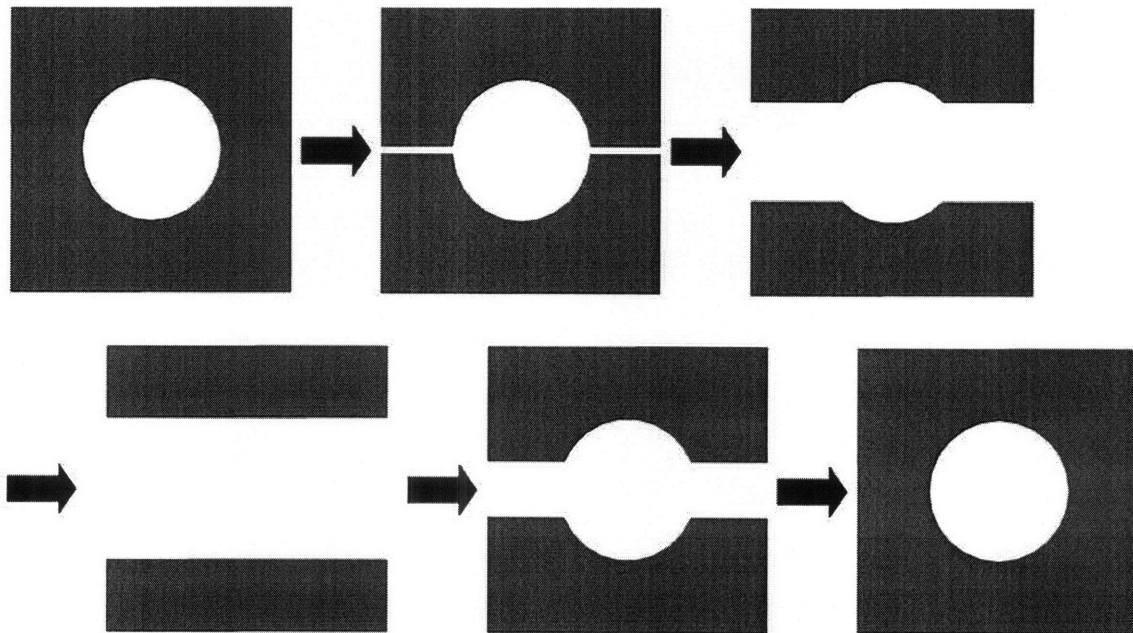
Figure 4-2: Variation in the boundary while crossing the improved gap

As previously mentioned, the fields within the metal region of the cross-section must be identically zero. This will be the case for each cross-section; however we note that the fields will be allowed to have a non-zero magnitude within the slots on the sides.

Let us now explore how the fields are propagated at each step. The propagation distance for each step will be $\Delta z = 2a/N$, with N being the total number of steps to cross the gap region. Recall that the fields are represented as a series of modes of the square

cavity, shown in Eqn (4.4). The propagation constant for each mode is therefore defined as:

$$k_{z,pq} = \sqrt{k^2 - \left(\frac{p\pi}{L}\right)^2 - \left(\frac{q\pi}{L}\right)^2}$$ (4.5)

where $k = \omega/c$.

We now propagate these fields by one step:

$$Ae^{j\varphi}{}_{(1)} = \sum D_{pq} \sin\left(\frac{p\pi x}{L}\right) \sin\left(\frac{q\pi y}{L}\right) \exp(jk_{z,pq}\Delta z)$$ (4.6)

This field solution though is not complete since there is still the outstanding condition stating that the fields must be zero within the metallic region. To account for this, we must first take the inverse FFT of the series of modes, returning to the domain of an array of field amplitudes and phases. We declare a new function $\tilde{A}e^{j\varphi}{}_{(1)}$ whose fields have been truncated according to the aforementioned criterion. The loss due to truncation from propagating across the first step is:

$$T_1 = \frac{\int A_{(1)}^2 dxdy - \int \tilde{A}_{(1)}^2 dxdy}{\int A_{(1)}^2 dxdy}$$ (4.7)

We then take $\tilde{A}e^{j\varphi}{}_{(1)}$ and as was the case with our initial function, we represent it as a series of modes of the square box by taking the FFT. This function is then propagated to the next cross-section where we take the inverse FFT, truncate the fields and calculate the loss once again. This process is repeated step-by-step until the whole improved gap region has been traversed and we obtain a final function $\tilde{A}(x,y)e^{j\varphi(x,y)}{}_{(N)}$. This final function is then decomposed into a series of HE_{1n} modes.

The result of each simulation can be broken down into three components: HE_{11} transmission, output power appearing in higher order modes, and a truncation loss that is

defined as $T_{GAP} = \sum_{n=1}^{N} T_n$.

4.1.2   Results

We now look at the results obtained using the numerical code that has been described. When running the code, we supply the ratio of the parasitic HOM content and this mode mixture will be solved across the entire range of relative phases. For all simulations, we consider the case of the ITER miter bends with $a = 31.75$ mm at 170 GHz. Figure 4-3 shows the HE_{11} output for an input mode mixture containing 3 % HE_{12}. This figure illustrates the dependence of the HE_{11} content of the output on the relative phase of the parasitic mode. We see that the amount of HE_{11} power varies sinusoidally with the relative phase. In Figure 4-4, we see how much HE_{11} power is lost, i.e. HE_{11} power in − HE_{11} power out, as a function of the amount of parasitic mode content. We see in the figure that as the parasitic mode content increases, the loss can diverge more and more from the value given a pure input mode, both above it and below it; however, it is important to notice that the average value still remains approximately the same.
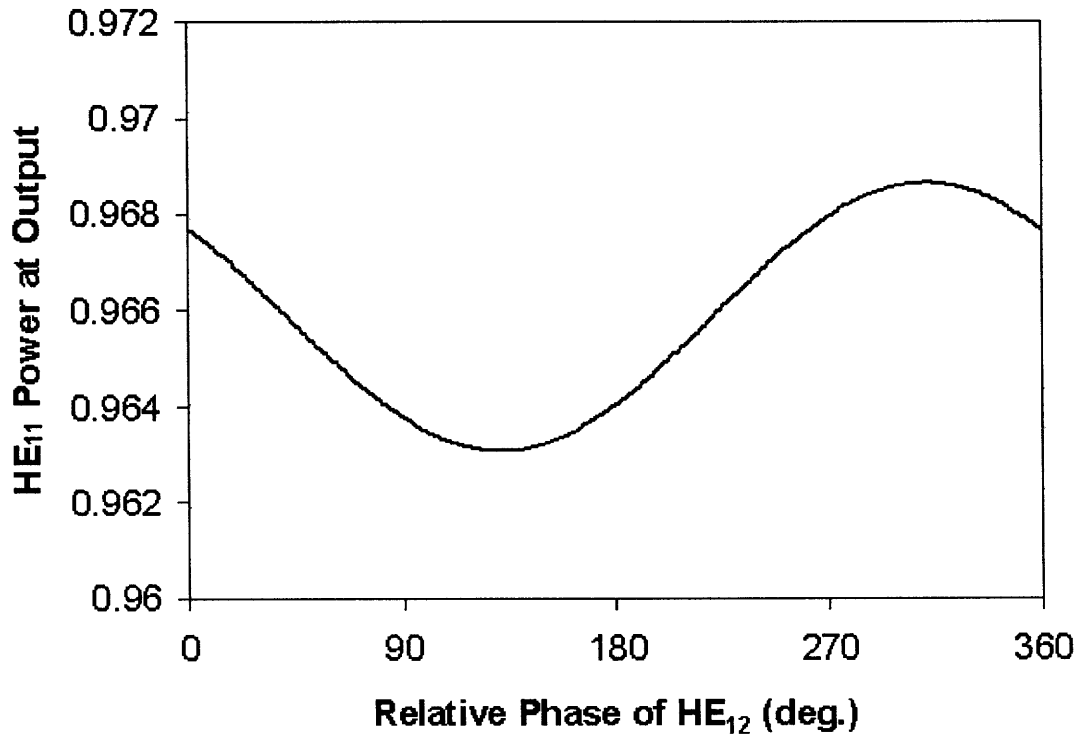
Figure 4-3: HE_{11} power at the output vs. the relative phase between the dominant HE_{11} mode and the parasitic HE_{12} mode for an input containing 3 % HE_{12}.
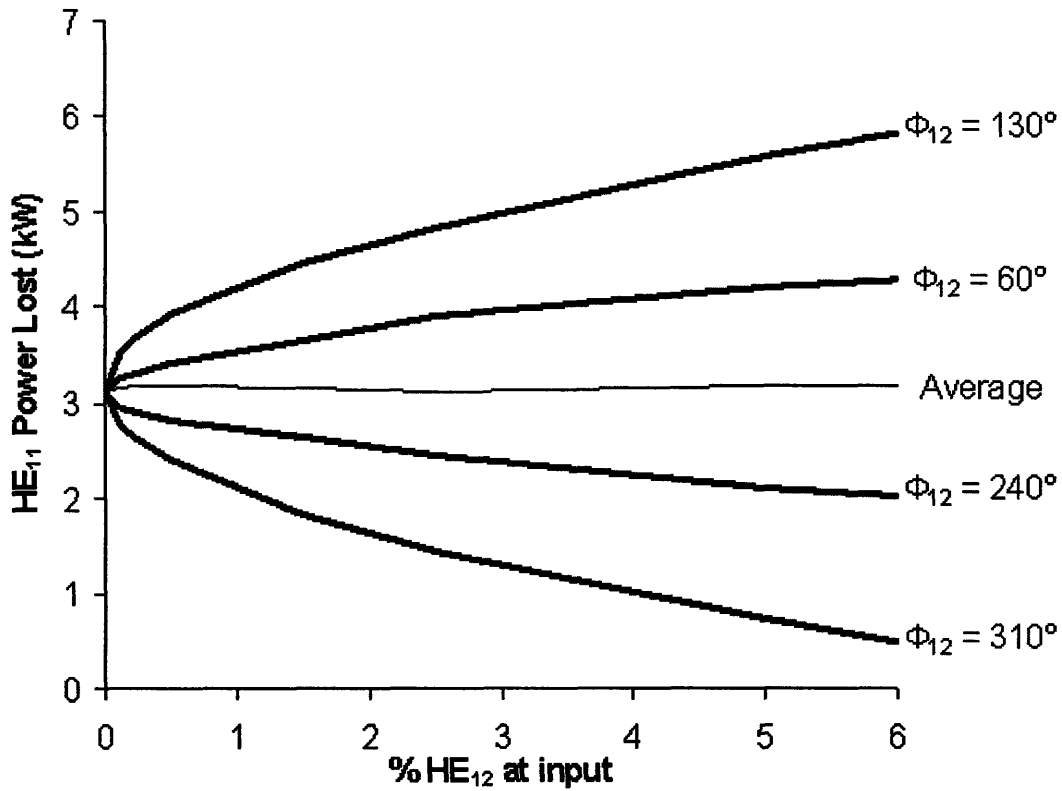
Figure 4-4: Power lost from the HE$_{11}$ mode at fixed relative phases as a function of the percentage of parasitic mode content at the input assuming a 1 MW input power

4.2 Analysis of Mode Mix Input Using Scattering Matrix Coefficients

The numerical simulations of the improved gap have demonstrated a new methodology for determining the losses in a miter bend. However, it is important to be able to bench-mark the above results to ensure that they agree reasonably well with the gap theory, as we should not expect any serious deviation except for the factor of two that relates the losses in the two geometries. Therefore, using the analytical expression for the scattering matrix coefficients from [31], we can perform a similar analysis for miter bends with a parasitic HOM at the input; however, in this case, we are once again considering the simple gap geometry. If the agreement between numerical and analytical results is good, this analytical approach can then be used to elaborate on the results of the previous

section since it is much easier to account for different amplitudes, phases, and modes with an analytical formula.

When solving using the scattering matrix coefficients, the problem is formulated in the same way as it was for the numerical code using Eqn (4.1); however in this case, we are not concerned with any field values. Thus, in solving the problem, we only need to determine the various amplitudes of the individual eigenmodes at the output as a function of the input amplitudes. If we assume an input of the form:

$$F_1 = A_1\psi_1 + A_2\psi_2 e^{j\varphi} \tag{4.8}$$

where ψ_1 and ψ_2 are the eigenfunctions representing the HE_{11} and HE_{12} modes respectively and φ is the relative phase of the second mode with respect to the first. The output will then be:

$$F_2 = \sum \left(S_{n1}A_1 + S_{n2}A_2 e^{j\varphi}\right)\psi_n \tag{4.9}$$

where the scattering coefficient S_{nm}, representing the coupling between ψ_m at the input with ψ_n at the output for the simple gap geometry, is defined as [31]:

$$S_{nm} = 2\chi_n\chi_m \sqrt{\frac{\sqrt{1-(\chi_n/ka)^2}}{\sqrt{1-(\chi_m/ka)^2}}} \int_0^\infty \frac{xJ_0^2(x)\exp\left[j2a(x^2-\chi_n^2)/(2ka^2)\right]}{(x^2-\chi_n^2)(x^2-\chi_m^2)}dx \tag{4.10}$$

with χ_m and χ_n being the respective Bessel zeros.

Solving the integral in Eqn (4.10) is no simple task. In order to obtain the scattering matrix, it was necessary to use a mathematical solver, such as Maple, that has the ability to perform numerical integration. Once this was complete, we could enter the scattering matrix of complex constants into MATLAB and use Eqn (4.9) to solve the problem of a dominant HE_{11} mode with a parasitic HE_{12} mode propagating across the simple gap. Figure 4-5 plots the magnitude of the scattering coefficients for HE_{11} and HE_{12} inputs for the first 20 output modes. Based on the result, we should expect to see the most mode conversion to the HE_{16} mode.
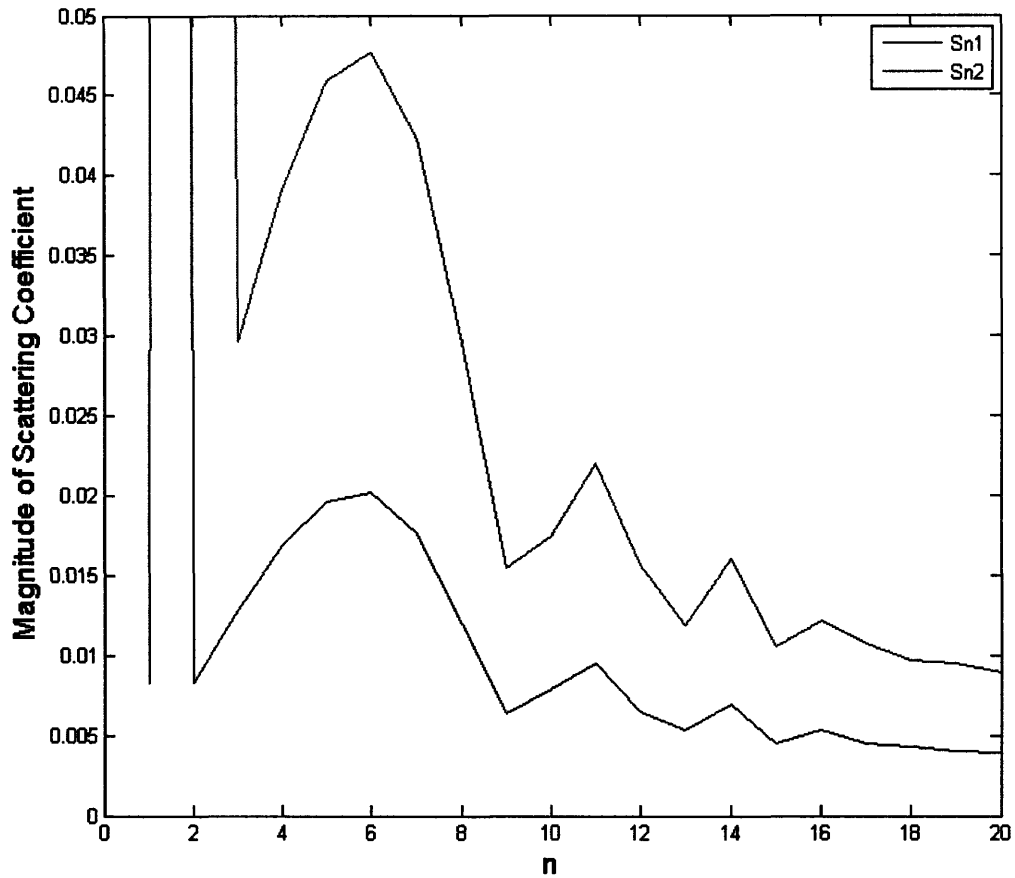
Figure 4-5: Scattering coefficients to mode HE_{1n} at the output for the HE_{11} and HE_{12} input modes

4.2.1   Comparison of Numerical Simulation and Analytical Approaches

To benchmark the numerical simulation results, we recreate the result of Figure 4-3 using the scattering coefficients, and plot both results in Figure 4-6. We first must recognize that while it seems like there is a large deviation between the results, this is not actually the case since we are considering two different geometries. Since the analytical formula is for the simple gap and not the improved gap, we expect the loss to be doubled. In both cases, the input HE_{11} power is 0.97, therefore if we consider the values at 0° phase, the simulation shows a loss of (0.97-0.9689) = 0.11% total power, while the analytical formula indicates a loss of (0.97-0.9668)/2 = 0.16% total power. While there may be a

small deviation in the loss numbers in the simulation, we see though that the trends are preserved quite accurately. In the scope of this problem of considering the effects of an input with a parasitic HOM, it is the trending that is most important, and the simulation code has good agreement with the analytical formula in this regard.

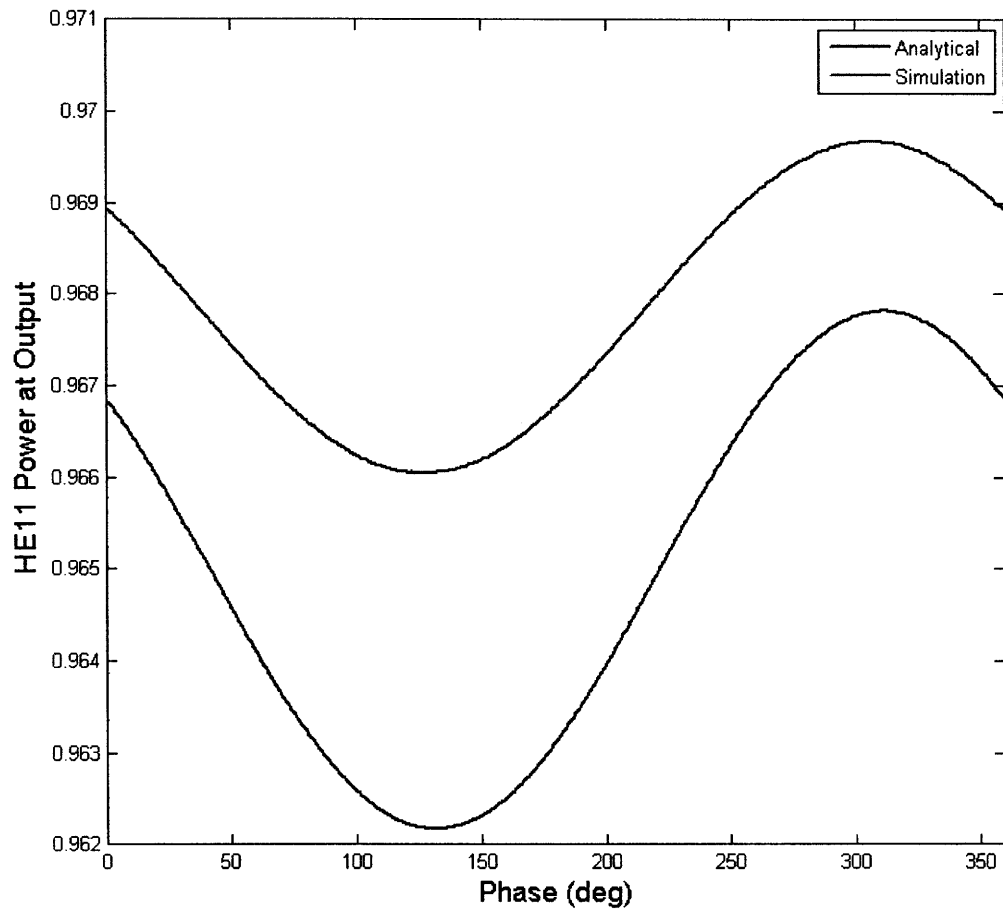**Figure 4-6: Comparison of the result of the numerical simulation and analytical formula for 3 % HOM content at the input**

4.2.2 Results and Discussion

Since the trends will be the same in the case of the numerical simulations and the analytic formula, we can introduce some new results that are more easily generated using the

scattering coefficients. As was the case with the numerical code, we solve for the ITER miter bends with $a = 31.75$ mm and a frequency of 170 GHz.
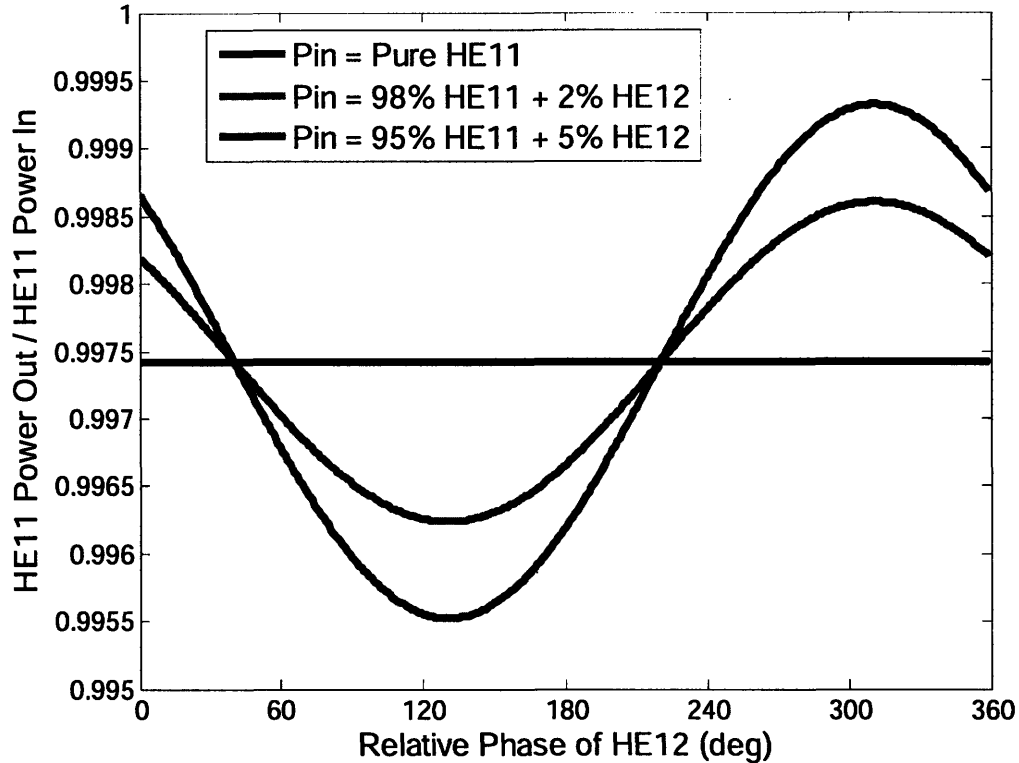
Figure 4-7: Dependence of the HE11 transmission on the amplitude and relative phase of a parasitic HE$_{12}$ mode

We can summarize the overall effect of the parasitic HOM at the input by the results in Figure 4-7. We observe that the amplitude of a HOM essentially determines the size of an error bar that could be put on loss of the miter bend, with the actual value depending on the relative phase. We also must realize that even a small amount of HOM content can have a fairly significant effect on the loss in the miter bend. For example, considering the case of 2 % HE$_{12}$ at the input, if the relative phase is such that the loss is maximized, the miter bend would have a mode conversion loss that is 46 % larger than the loss assuming a pure HE$_{11}$ input. This result will obviously have consequences.

First, this has a major impact on bridging the gap between experiment and theory. Depending on the situation, the result of considering HOM inputs can be either good news or bad news. In situations where there is a discrepancy between theory and experi-

ment, the presence of some HOM content in the transmission line can actually serve as a possible explanation for why experimental measurements do not match theoretical estimates. On the other hand, if there is good agreement between experiment and theory, the HOM content introduces uncertainty as to what the true expected theoretical value is, meaning that the measured value could simply be matching an incorrect theoretical value. We also expect that such a result has an impact on the design of millimeter wave transmission lines since the uncertainty in the miter bend loss will be reflected in the total loss estimate and possibly higher losses could also result in more heating of the transmission line.

In addition to simply analyzing the transmission and loss of the dominant mode, we can also consider how the power is lost. In the gap geometry, lost HE_{11} power can appear either as HOM content at the output or in power that fails to traverse the gap. In a miter bend, this latter term generates power in very high order modes that are absorbed just upstream or downstream from the bend. In Figure 4-8, we see how the power that fails to traverse the gap is affected by the amount of HOM content at the input. Again, there is a range of possible values and the curves that are plotted correspond to the relative phases that result in the maximum and minimum transmission. Unlike the case of the HE_{11} loss, we see that the average power failing to traverse the gap does not remain constant and instead increases with increasing parasitic HOM content at the input. This result also has major consequences on the design of transmission lines with respect to heat dissipation. As previously mentioned, this high order mode power will cause significant heating in the region around the miter bend. This result proves that it is not acceptable to simply assume a pure mode since given any HOM content at the input, we now expect there on average to be more heating. When it comes to accounting for heating, it is much more advisable to design a system around the worst-case scenario. Here we see that for as little as 4 % HOM content at the input, the power being absorbed into the line could as much as double. If this were not taken into consideration and proper safety margins were not built into the line to account for heating, then this excess power could have quite a serious effect if it were sufficient to result in sag or deformation of the line in any way.
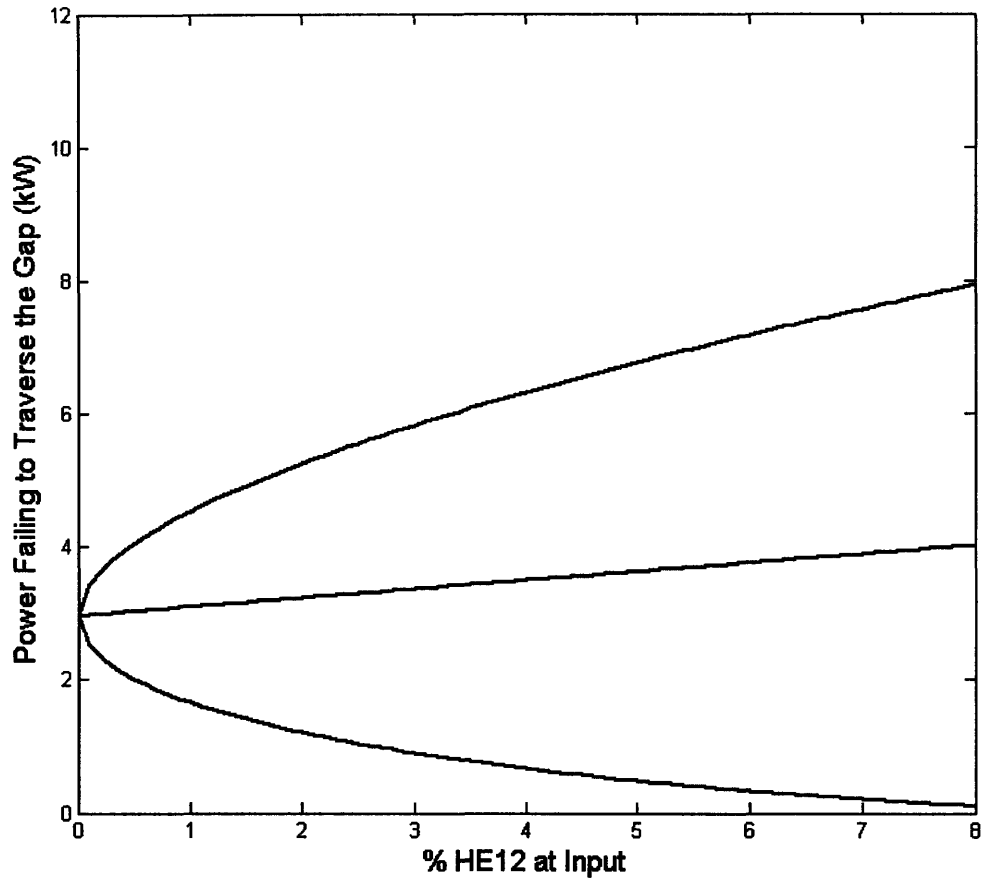
Figure 4-8: Power that fails to traverse the gap as a function of the parasitic mode content for a 1 MW input with the center line representing the average

4.3 Summary

A new technique for determining the losses of miter bends was introduced. This numerical code considers an improved gap geometry which is more similar to an actual miter bend compared with standard gap theory.

This numerical code, in addition to the analytical scattering coefficients from standard gap theory, was used to determine the effect of having an input mode to a miter bend consisting of a dominant mode and a parasitic higher order mode (HOM). We found that the transmission through the miter bend was a strong function of both the amplitude of the parasitic HOM as well as its phase relative to the phase of the dominant mode. While

the average transmission of the dominant mode remains unchanged with increased HOM content, the possible values of the loss can diverge more and more from the expected value, a result that introduces uncertainty into the validity of any experimental measurement. At the same time, when the parasitic HOM content at the input increases, the power in very high order modes will increase on average, which will result in more heating around the miter bend. The effects of parasitic HOMs should therefore be taken into consideration in the design of millimeter wave transmission lines.

Chapter 5

Measurement of Miter Bend Losses

Up until now, there has been much discussion about the nature of losses in transmission lines. The miter bend has been established as a major contributor of the overall loss in transmission line systems, and the theory of losses in miter bends has been considered from several different perspectives. Many interesting theoretical results about miter bend losses have been presented, however despite all this progress, there still remains no absolute, unequivocal theory for the exact amount of loss in a miter bend and the nature of such losses. In these types of situations, when the theory can only be considered approximate, experimental results can prove to be a very effective tool. Even the roughest of measurements can generally at least confirm that a theoretical prediction is in the correct ballpark, while a very careful and precise experimental campaign can go a long way in proving or disproving any theoretical work.

With this in mind, we consider the ITER project. Being such a large and costly international collaboration, it puts a lot of pressure on each of the individual engineering teams assigned to their respective systems. When one team's system depends on the output of another's for example, it is important that this system adheres to the guidelines and specifications laid out in the design. The transmission lines for ITER's ECH system are a perfect example since they are fed power from the gyrotrons that are the responsibility of a separate engineering team. The effect of higher order modes (HOMs) in the transmission line was considered in the previous chapter, with the result being that they have the possibility to drastically increase the loss. So while there is a specification on the quality of the gyrotron beams, this is a factor that is out of the control of the team responsible for the transmission lines, thus introducing some uncertainty.

At the same time, the transmission line team has its own set of specifications. According to the ITER Detailed Design Document Section 5.2, the transmission loss from the gyrotron sources to the plasma, which includes the transmission lines and the ECH launcher, is limited to 17 %. In Chapter 2, the losses of the transmission line alone were shown, and were already quite close to this imposed limit. As such, it is very important that the loss in every component be kept to a minimum. In addition, with relatively little margin for error, the loss of each component should be known with great precision. We need to look no further than the miter bends to illustrate this point. If the gap theory is underestimating the loss by as little as 0.5 % per miter bend, the transmission line could already be over the limit. If that were the case, it would be imperative that the design team know so that a redesign of the transmission line could take place. Therefore, it is very important that experiments are undertaken to precisely measure the losses in these components and ensure that all theoretical predictions are correct.

While it may sound relatively straightforward, it is no simple task to measure the losses in the ITER transmission lines. First, there are only so many options with regards to equipment for measurements at millimeter wave frequencies. Secondly, even though we have been constantly referring to the miter bends as high loss components, this is only relative to the other transmission line components. For such large, overmoded waveguide, the loss per miter bend is actually quite small, making it increasingly hard to obtain an extremely accurate result.

One way to measure the losses of transmission line components is to do so using high power sources [35]. Such measurements allow for several other ways of measuring the loss; however, due to the source, there is doubt as to the purity of the input mode and this is also generally a long and laborious campaign. As a result, we will discuss a couple of cold test (low power) techniques for measuring low loss transmission line components. We will first consider the case of a smaller test transmission line to illustrate these techniques before tackling the measurement of the prototype ITER ECH transmission line.

5.1 Low Power Measurement of Transmission Line Losses

The following section is adapted from a 2008 paper submitted to the International Journal of Infrared and Millimeter Waves by S.T. Han et al. with contributions from the author of this thesis.

We now introduce two techniques for low power testing of transmission line components: a coherent technique using a vector network analyzer (VNA) and an incoherent technique using a radiometer. The losses were measured in two separate transmission lines: the prototype ITER ECH 170 GHz transmission line which has previously been discussed in this thesis, and a smaller 140 GHz corrugated transmission line which is used for a spectroscopy application, built by Thomas Keating. The reason for introducing this second "test" transmission line is that, as established in Chapter 2, the loss in a miter bend is dependant on the value of a/λ for the particular transmission line, thus the test line is a good way of proving the effectiveness of the measurement techniques before tackling the measurement of the extremely small loss of the ITER transmission line.

5.2 Measurement of 140 GHz Transmission Line

5.2.1 Coherent Technique

We first consider the coherent technique. For this measurement, and for any subsequent measurement using a VNA, we use an Agilent E8363B PNA. For this 140 GHz transmission line, we attach WR8 (90-147 GHz) millimeter wave extension heads from Oleson Microwave Labs which launch a TE_{10} mode in the rectangular waveguide.

For the experimental setup, we begin by attaching corrugated horns and rectangular to circular waveguide adapters at the two millimeter wave heads in order to launch an HE_{11} mode in the corrugated waveguide at the transmitter and convert back to the TE_{10} rectangular mode at the receiver. We next insert two hollow dielectric waveguides between the tapered horns and the corrugated waveguides to damp the unwanted higher order modes that are also generated at the HE_{11} mode launchers and tapers. The hollow

dielectric waveguides are tubes made from G10 and have an inner diameter of 12.7 mm, a thickness of 2 cm, and are each 10 cm long. If the loss in the tube wall is large enough for the tube to be considered infinite in radial extent, then the Gaussian-like mode in the hollow dielectric waveguide will be identical to that in the attached corrugated waveguide [19]. The baseline setup also consists of 1.5 m of straight corrugated waveguide and a miter bend.

To determine the loss, a device under test (DUT) is inserted and the DUT loss can be determined by calculating the difference between the loss in the total system and the loss of the baseline system. The experimental setup for this measurement is shown in Figure 5-1. The DUT consists of 3 miter bends and 1.7 m of straight corrugated waveguide.

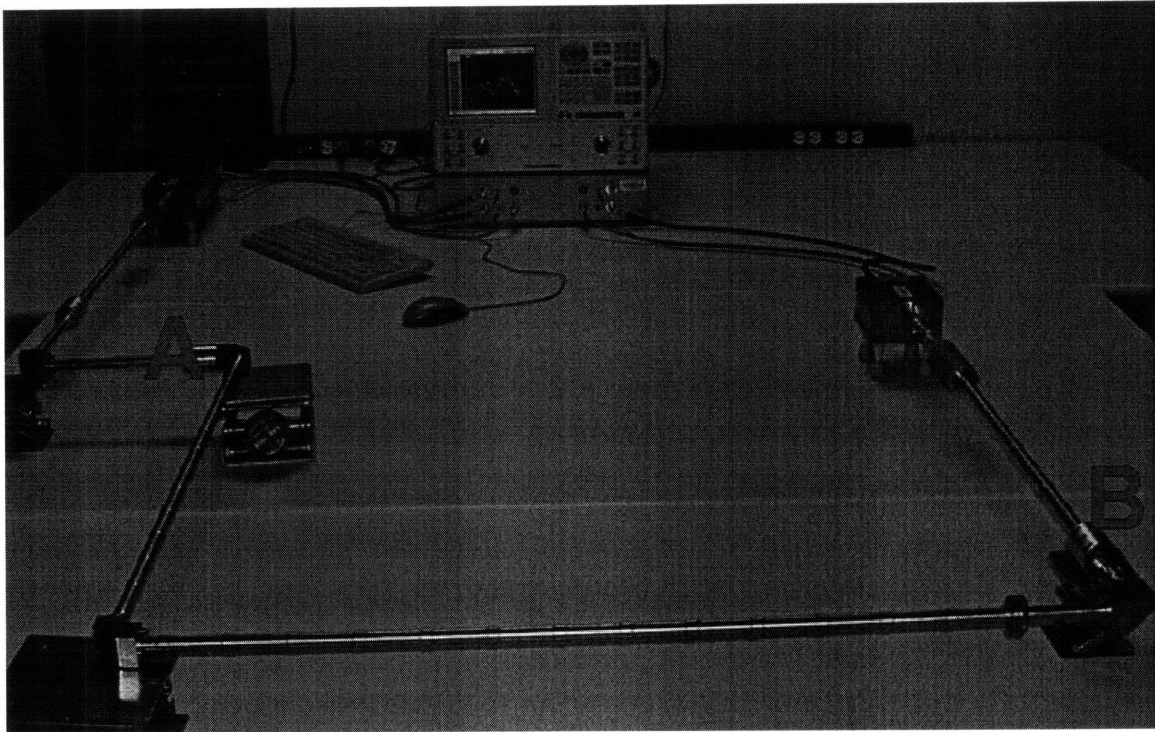**Figure 5-1: Experimental setup for the coherent technique using a VNA. Device under test (DUT) is shown between A and B**

The loss measured for the DUT was 0.9 dB at 140 GHz, shown in Figure 5-2. This measurement was reproducible within ± 0.2 dB. The loss per miter bend is therefore 0.3 dB and counting both systematic and random error the error bar on the loss of each miter bend is ± 0.1 dB.
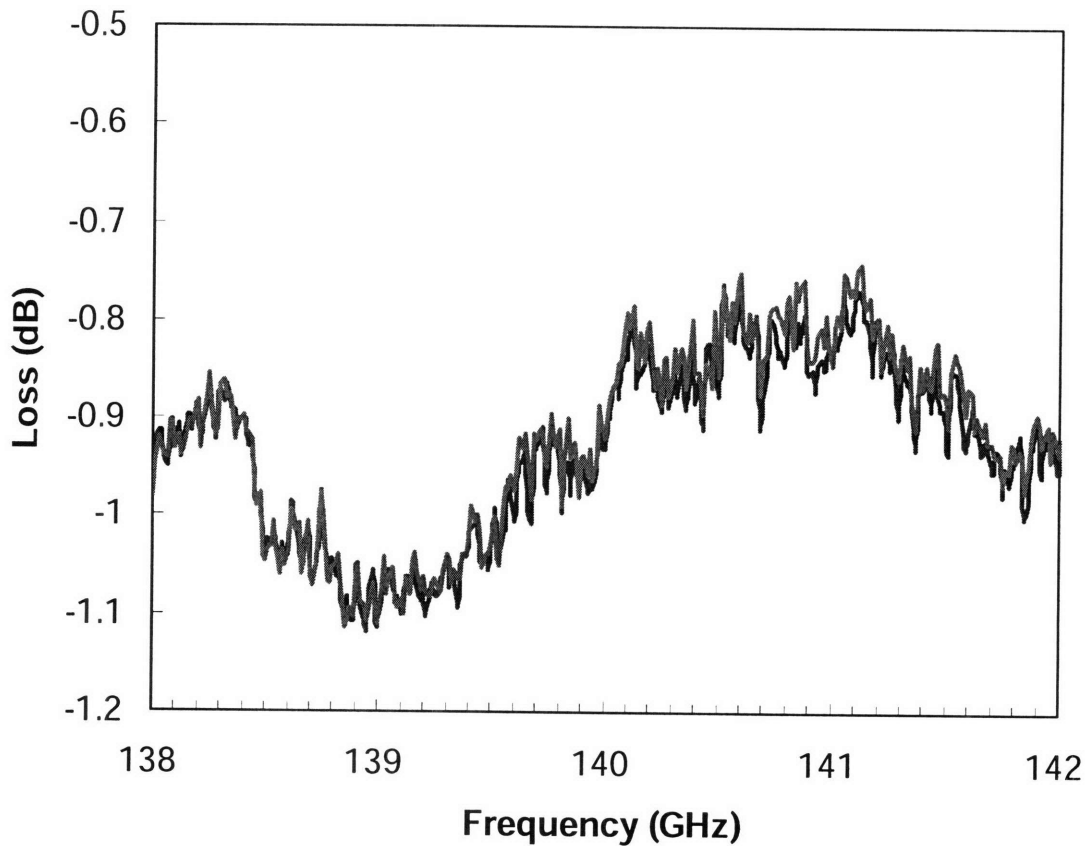
Figure 5-2: Loss for DUT consisting of 3 miter bends measured using the coherent technique

5.2.2   Incoherent Technique

We next consider an incoherent technique using a radiometer. The radiometer is used to measure the transmission losses of incoherent thermal radiation, or equivalently the increase in radiometer noise temperature when a transmission line is inserted into the radiometer field of view of a black body of known temperature.

The radiometer consists of a 137 GHz local oscillator and intermediate frequency amplifiers of 2 GHz bandwidth, thus allowing for measurement of radiation from a black body between 135 and 139 GHz. In this experiment, the black body is a liquid-nitrogen cooled 30mm thick eccosorb sheet [36].

A corrugated horn provides an HE_{11} mode field-of-view that was coupled to the transmission line diameter by a hollow acrylic conical transition. A chopper and lock-in

amplifier allow for stable phase sensitive detection of the change in measured receiver noise temperature which is proportional to the insertion loss of the DUT. The experimental setup for this technique is shown in Figure 5-3.
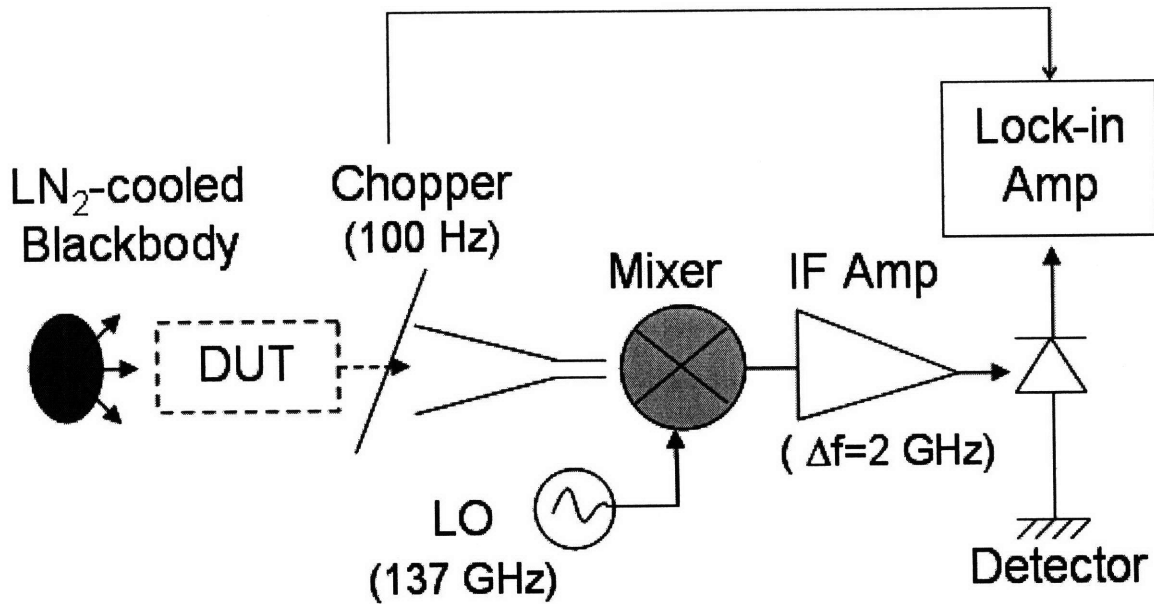

Figure 5-3: Schematic of the experimental setup for the incoherent technique using a radiometer

The loss is determined by comparing the detected voltage with and without the DUT over the frequency range. The result using the incoherent technique here indicated a loss per miter bend of 0.22 ± 0.1 dB, agreeing relatively well with the loss measured using the coherent technique. The transmission line has an a/λ value of ~3 which, according to the gap theory, should have a loss of 0.17 dB per miter bend. The measured losses were slightly higher; however the theory value is within the error bars of the measurements.

5.3 Loss Measurement of ITER Transmission Line

Compared to the test line, the losses in the ITER line will be significantly smaller since the 63.5 mm diameter 170 GHz line has an a/λ of ~18, corresponding to a theoretical loss of only 0.027 dB. With such a small expected loss, the experimental equipment must be very precise to be able to measure it. At the outset, both techniques were considered,

however the BWO which was to be used for the incoherent technique proved to be too unstable for the precision that is required to make this measurement, therefore we only consider the results of the coherent technique for the ITER transmission line.

For this measurement at 170 GHz, a set of WR5 (140-220 GHz) millimeter wave extension heads from Oleson Microwave Labs are used in conjunction with the VNA. The approach to measuring the loss will be the same here: measure a baseline system, insert a DUT and determine the differential loss.
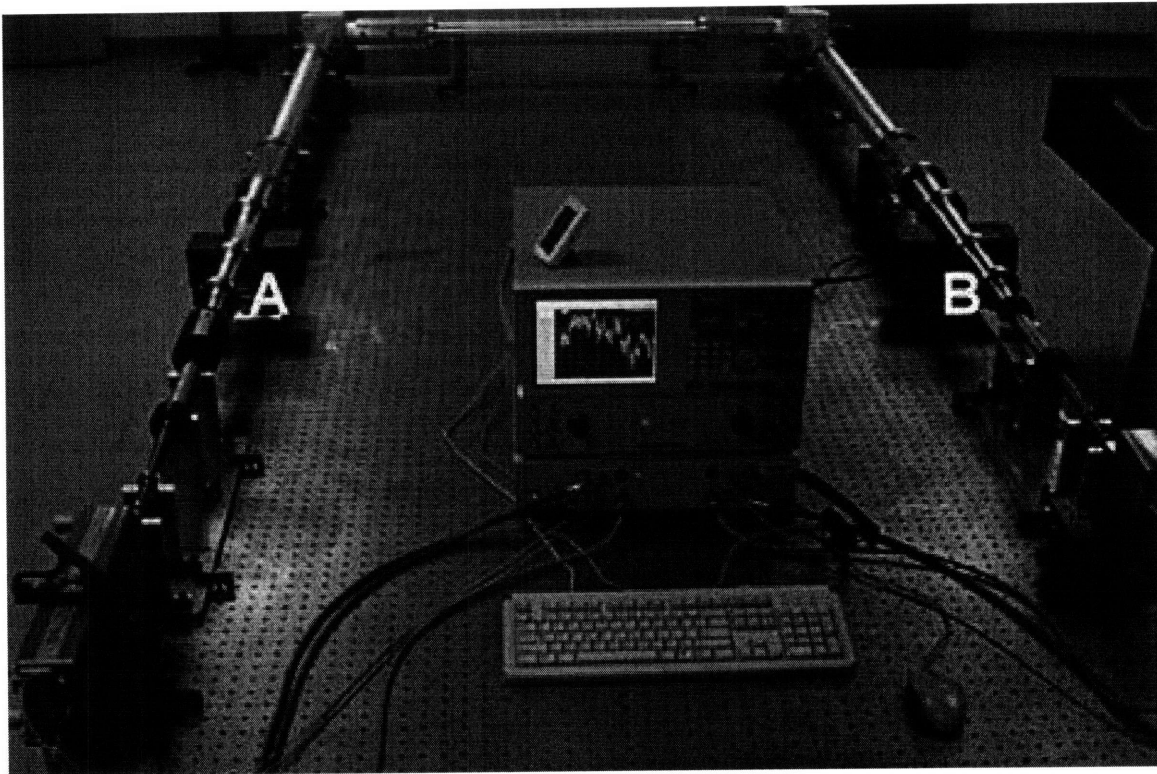
Figure 5-4: Experimental setup for the loss measurement of the 170 GHz ITER transmission line using a VNA

For the ITER waveguide, the baseline setup consists of a series of tapers, adapters and a phase shifting waveguide to convert the fundamental mode in the WR5 rectangular waveguide into an HE_{11} mode in 20.32 mm diameter circular corrugated waveguide as well as a dielectric filter to suppress higher order modes. The experimental setup is shown in Figure 5-4 where the DUT consisting of 2 miter bends, 3 sections of straight corrugated waveguide each 1 m long, and 2 corrugated uptaper sections going from 20.32 mm diameter to 63.5 mm diameter is inserted between points A and B. Initially, the

measured loss of the DUT, shown in Figure 5-5, appeared to be much too large; however, we then considered that there was possibly additional loss by atmospheric effects caused by the high water absorption nearby in frequency at 183.3 GHz. After accounting for this extra factor, the loss per miter bend was determined to be 0.05 ± 0.02 dB. While this loss agrees reasonably well with gap theory value of 0.027 dB, as was the case with the test transmission line, the loss is higher than the theoretical prediction.
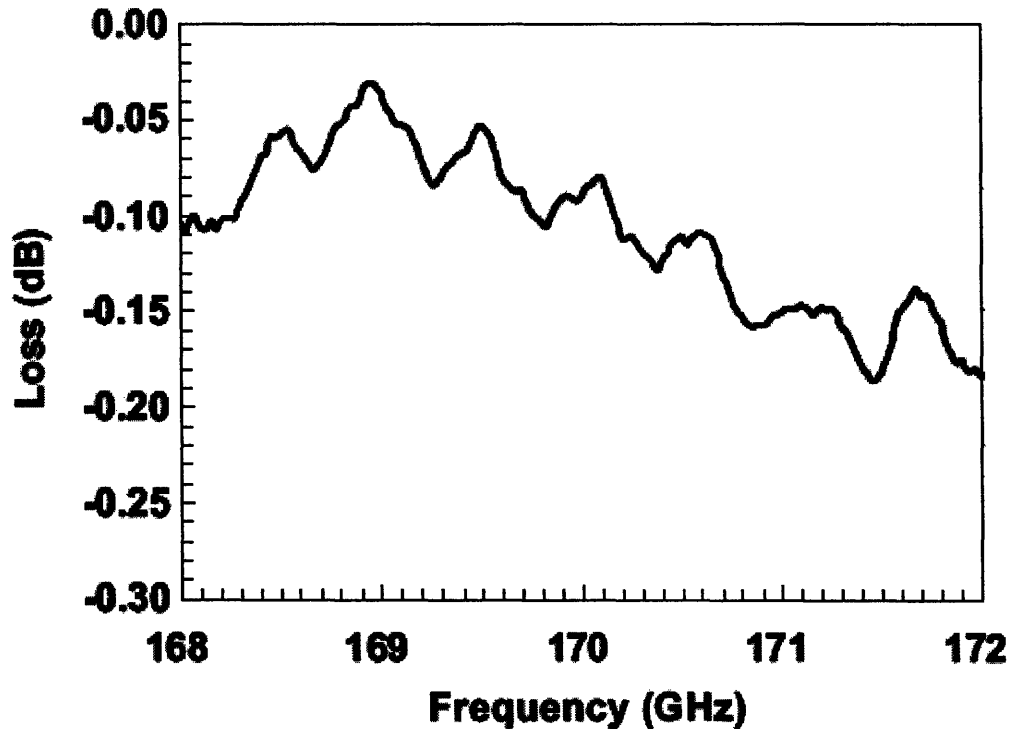
Figure 5-5: Measured loss of the DUT for the 170 GHz ITER ECH transmission line

5.4 Summary

Two distinct techniques have been presented for measuring the loss in millimeter wave transmission line components. For the same device under test, both techniques yielded very similar results. In all three cases, which included measurements using both techniques as well as measurements on two separate transmission lines, the loss per miter bend was found to be larger than the theoretical prediction offered by the gap theory; however due to some uncertainty in the measurements, it is difficult to say definitively

whether the difference can be attributed to a deviation in the experiment or an incorrect prediction from the theory.

Chapter 6

Measurement of Mode Conversion in ITER Miter Bends

In the previous chapter, a couple of techniques for measuring the loss through a millimeter wave transmission line were discussed. While these techniques can yield some very valuable results, there is at least one piece of information that cannot be obtained from the methods, and that is information about the mode content. Whenever a gap geometry has been considered, the lost power either fails to traverse the gap or appears as higher order modes (HOMs) at the output. In the case of the miter bend, when we neglect the tiny Ohmic loss, the power must be accounted for in higher order modes at the output or as very high order modes at either the output or the input. In order to delve into this problem, a new approach is required.

6.1 Preliminary Measurement

Before beginning a full blown measurement campaign, it was first advisable to run some preliminary measurements and to determine the feasibility of such measurements. The goal is to measure the mode pattern of the transmission line before and after a miter bend to see if there is any noticeable deformation of the field pattern, indicating that some mode conversion took place in the bend. To do such a measurement, we take the setup used for VNA measurement of the ITER ECH transmission line described in the previous chapter and remove the second set of tapers and filters, thus leaving an open ended 63.5 mm diameter at the receiving end. We can now attach a receiving antenna to the receiving head of the VNA so that we are only measuring the fields at a very specific location.

To act as the receiving antenna, we use a piece of cut waveguide, i.e. a simple straight waveguide section without a flange.
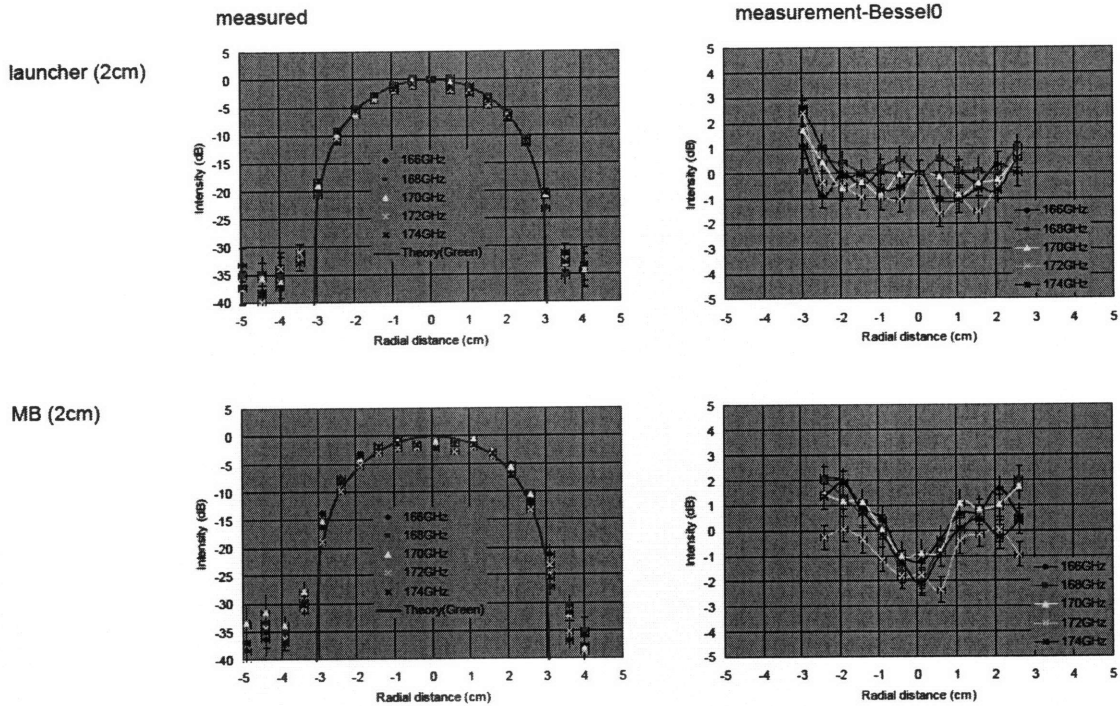

Figure 6-1: Results of preliminary 1-D scans of the field pattern within the ITER transmission line comparing the pattern for the launcher alone with the pattern for the launcher and a miter bend

Since this is a preliminary measurement, with all adjustments being done by hand, it is sufficient to simply scan along the central axis of the waveguide to see a cross-section of the field pattern. If there is any visible mode conversion, it should be able to be seen on these 1-D cross-sections. Thus the head was positioned accordingly and was moved in 5 mm increments across the aperture of the waveguide. At every point the VNA measurement was recorded for a few frequencies, providing us with the field profile. The results of these preliminary scans, with and without a miter bend, are shown in Figure 6-1. We see that there is a noticeable difference between the two results, particularly when considering the figures on the right which show the differential between measurement and the J_0 Bessel, i.e. a pure HE_{11} mode. The data for the launcher appears to just have some random measurement noise, which is expected, but still matches well with the HE_{11} field pattern; however the field pattern after the miter bend has a noticeable dip below the HE_{11} value in the center and is larger along the edges. Figure 6-2 shows the

81

amplitude of the HE_{11} and HE_{12} modes plotted on a linear scale. If we apply the result shown in this figure to the results of Figure 6-1, then the mode conversion that is seen in the presence of the miter bend could be consistent with a small amount of HE_{12} mode content that is out of phase with the HE_{11} mode, i.e. its amplitude is negative at the center of the waveguide.
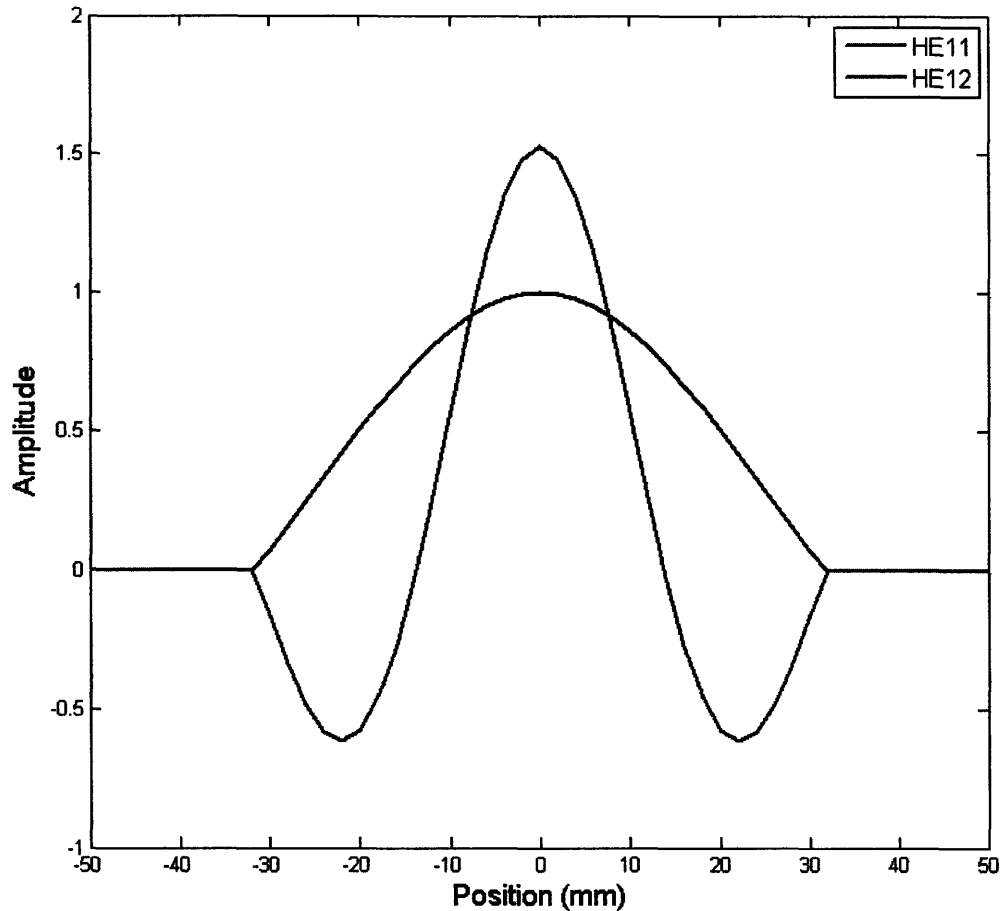

Figure 6-2: Amplitude of a HE_{11} and HE_{12} mode along the central axis of a 63.5 mm diameter waveguide on a linear scale with the power in each mode normalized

These preliminary results are quite promising so we will therefore pursue much more accurate and rigorous measurements of the mode content of the ITER transmission lines.

6.2 Constructing the Experiment

The first step to this measurement campaign involves setting up the required equipment to perform the measurements. We recognize that in order to accurately and correctly determine the mode content in the transmission line we will require full 2-D scans of the waveguide aperture.

In order to be able to do these measurements with good precision, repeatability, and speed, a scanning system is needed. Since no such scanner was already available, the first task was to obtain the parts and construct the system. The scanner parts were purchased from Velmex, Inc. and consisted of the following:

- 3 BiSlide Assemblies, each containing a screw and carriage assembly allowing for motion along an axis

- 3 step motors, which, along with the pitch of the screw, allows for motion as precise as 6 microns per step

- VXM Motor controller which allows for manual motor control as well as control via a computer interface

Using the supplied joints and brackets, the assemblies were connected together allowing for scanning along all three axes. As was the case for the preliminary measurement, the VNA will be used to measure the data, thus we construct a special plate that allows us to mount the receiving head of the VNA on to the vertical axis of the scanner. The constructed scanner system along with the VNA is shown in Figure 6-3. This figure shows the setup for another application for which we used the scanner: measurement of a gyrotron's internal mode converter.

In Chapter 4, it was mentioned that the gyrotrons output a Gaussian beam when discussing the issue of higher order modes in the ITER transmission lines. The internal mode converter serves to convert the power from the gyrotron's mode of operation in the cavity, in this case a $TE_{22,6}$ mode, into a (hopefully) perfect Gaussian beam. This though is no easy task, so the scanner is an excellent tool in measuring an accurate profile of the output beam and determining if it is elliptical or has significant sidelobes to validate the design of the mode converter. While these measurements produced interesting results, they are not pertinent to the rest of the matter contained in this thesis and are omitted.
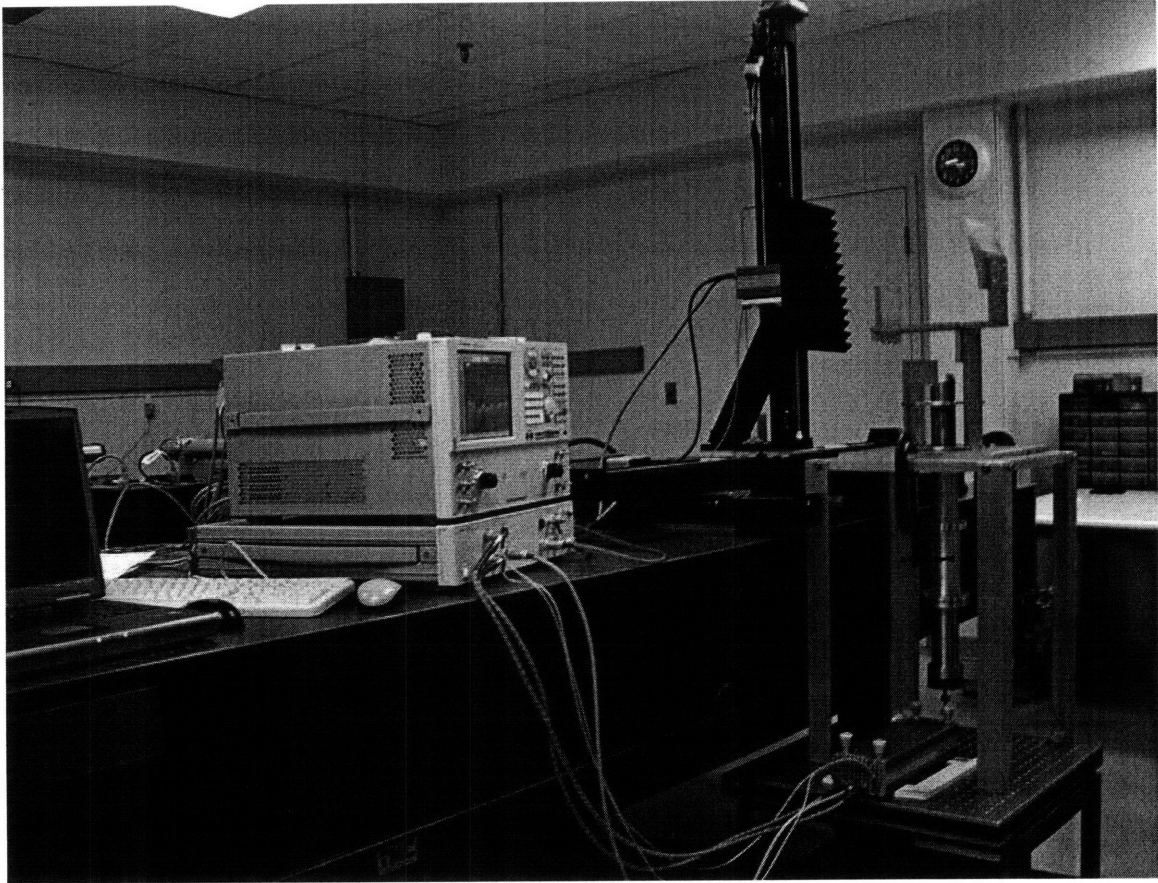
Figure 6-3: Experimental setup of the 3-axis scanning system, shown for the measurement of a gyrotron internal mode converter

The final component of the setup, and arguably most important, is the computer interface. Using a program such as LabView, we are able to interface with both the motor controller and the VNA. The interface of the LabView code which was developed for the scanner is shown in Figure 6-4. The interface allows all necessary VNA options to be set on the computer, such as the number of sweep points, the frequency range being measured by the VNA, the parameter and type of measurement to be performed (S_{11}/S_{21} and Phase/Magnitude), as well as the discrete frequencies of interest to the user. The scan parameters such as the distance between each step in the measurement plane and the number of measurement planes can also be set. When run, the code will move the motors step-by-step through the measurement grid defined by the user's settings. At each point, the VNA data is accessed, and the measurement at each user-selected frequency is written

to a file. This output file is formatted such that it is easily read by a program like MATLAB for the purpose of data analysis.
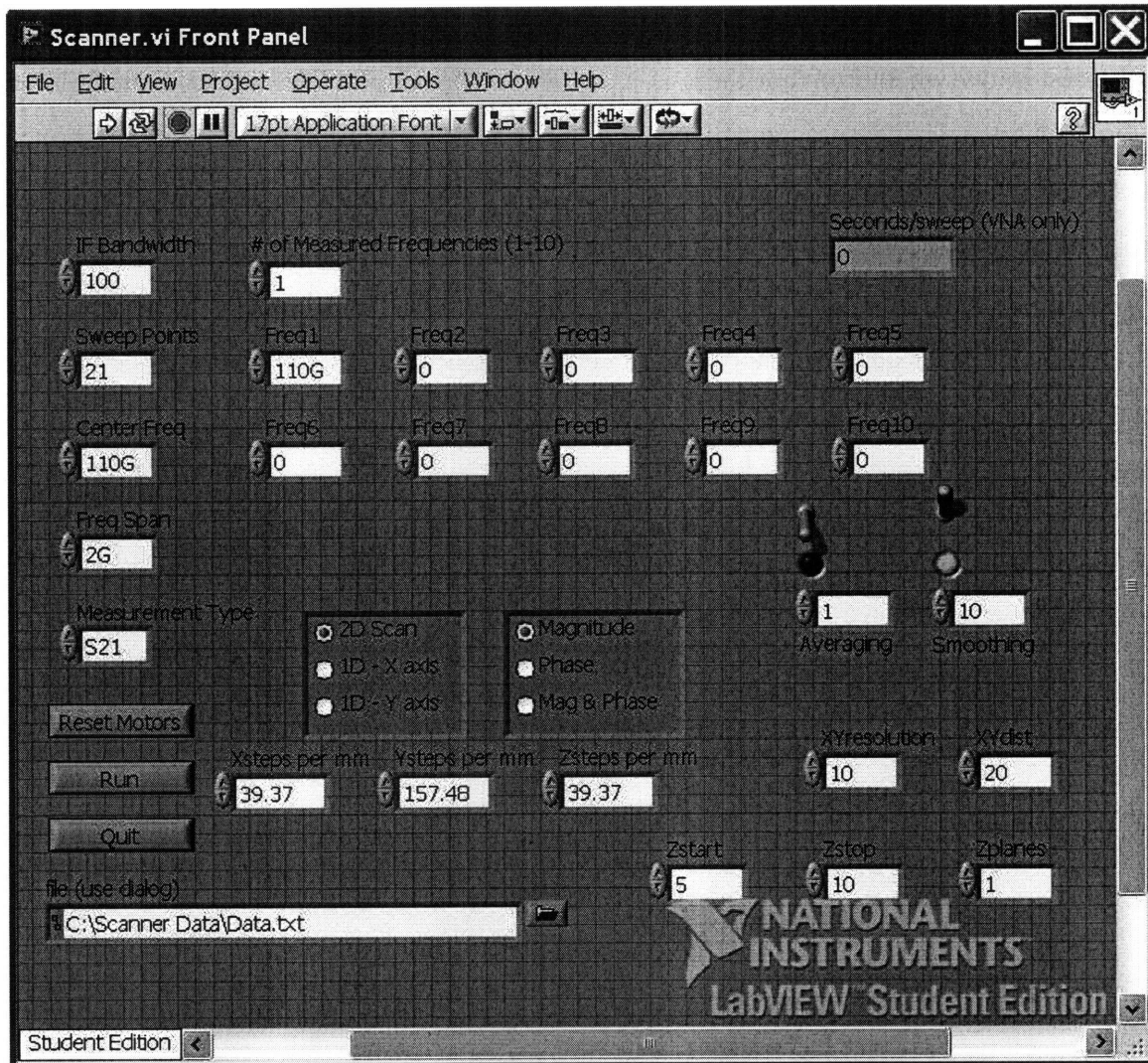
Figure 6-4: Interface of the LabView code developed for the 3-axis scanner system

6.3 Evaluating Measurement Accuracy

When approaching the measurement of the ITER waveguide, there are a number of things that we must take into consideration to ensure that all data being taken is valid.

Most importantly, we must consider any inherent inaccuracies in the VNA measurements. We recognize that unlike the measurements outlined in Chapter 5, calibration of the VNA is not a factor here. Since we are only concerned with determining the mode

content, each data point is only considered relative to other data points on the same measurement plane. The power measured for any plane can simply be normalized in order to make all measurements consistent. However, to ensure the integrity of the data, we must know whether or not there is a significant drift in the VNA data over the time frame of a single measurement plane. Figure 6-5 shows how the measured magnitude and phase values of the VNA vary over the course of 85 minutes with a data point being recorded every second. Over this time frame, the magnitude drifted approximately 0.02 dB while the phase drifted approximately 1°. An average 50 x 50 measurement using the scanner code takes approximately 25 minutes to run, thus any drift would be one third of the aforementioned values and is negligible. The results of Figure 6-5 are also useful in demonstrating the accuracy of a VNA measurement since we can see a small fluctuation in the measured values over a very short time frame. From the figure, we determine that this fluctuation is ± 0.025 dB for magnitude measurements and ± 0.2° for phase measurements.

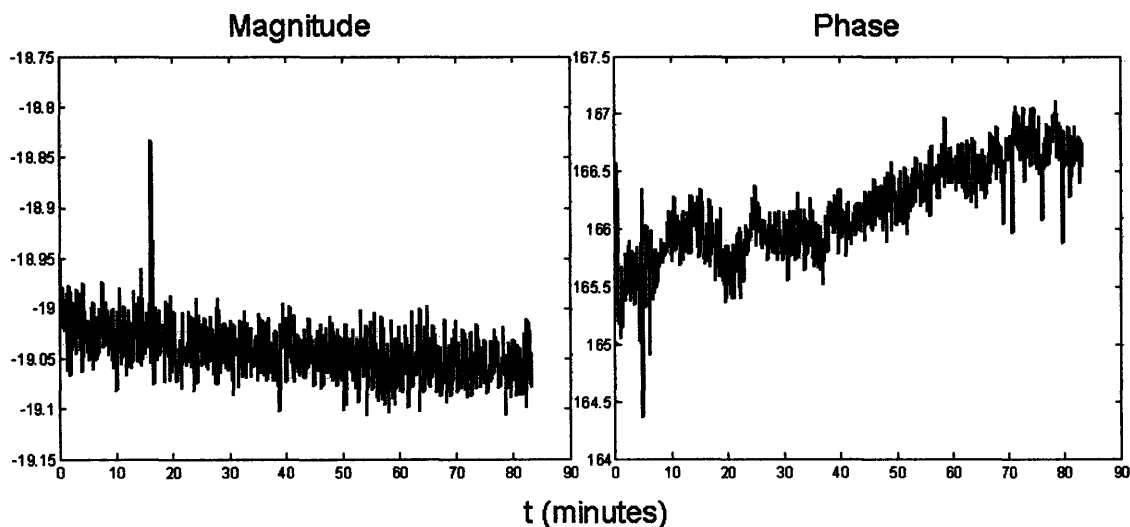Figure 6-5: Measurement of the drift in VNA data

We must also consider that when the scanner system moves around the grid, the cables connecting the receiver head and the VNA body are being contorted, which could possibly introduce some uncertainty. In Figure 6-6, we see that the VNA measurements are quite repeatable in spite of the fact that the cables were contorted between each measurement.
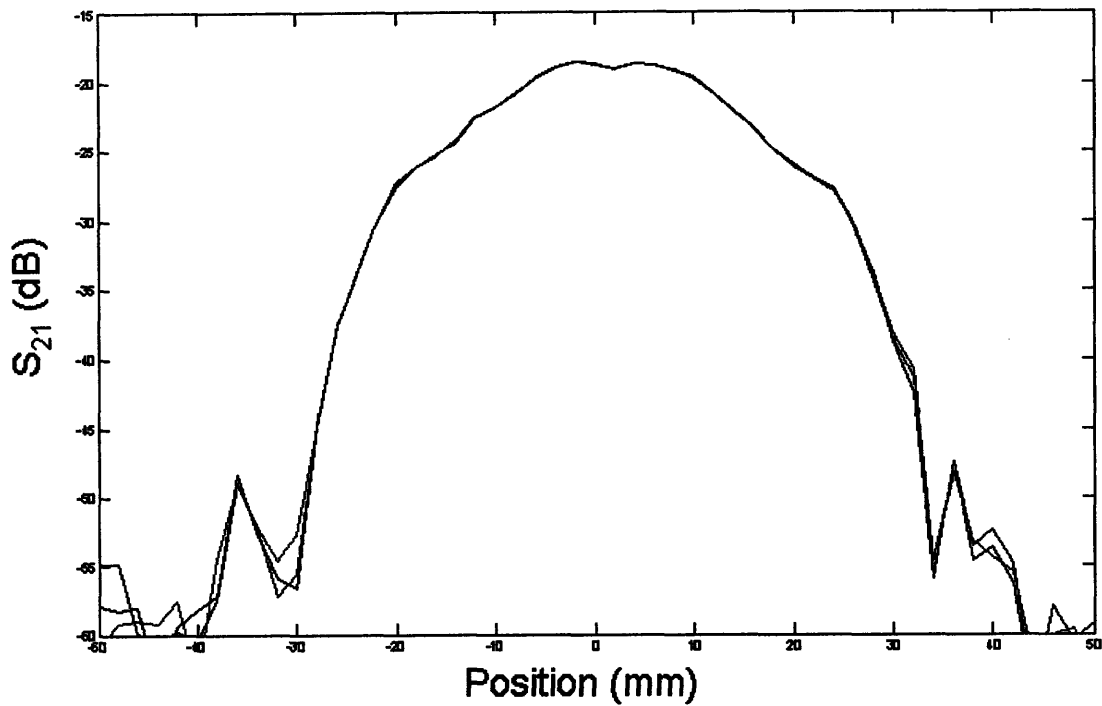
Figure 6-6: Repeatability of VNA measurement

A final issue to consider is how the VNA measurements are affected during a 2-D scan by the physical surroundings. When doing ITER measurements, we want to make sure that we do not have any issue with power reflecting off various surfaces and introducing unnecessary error into the results. As a result, we place a large eccosorb sheet around the cut waveguide attached to the receiver head to prevent any reflections from the metallic face of the VNA receiver as well as a small pyramidal piece to cover the flange of the waveguide. We can then measure S_{11} of the system to determine if there is any change to the amount of reflection as we scan across the entire measurement plane. Figure 6-7 shows the side view of the 2-D surface plot representing the S_{11} values measured as the scanner moves from location-to location in the measurement plane. While there is a variation of about 0.6 dB in the measured S_{11}, this is actually incredibly small, since even if the scanner is static at the aperture of the ITER waveguide, there is an inherent fluctuation of the same order. However, the real reason we know that this small fluctuation is not due to the scanner system is that there is no pattern to the variation in S_{11}. If there was an effect due to the scanner, we would expect to see a peak when the cut waveguide,

which is the only metal surface facing the ITER waveguide, was at or around the center of the ITER waveguide where the field intensity is peaked; however, we see no such effect.
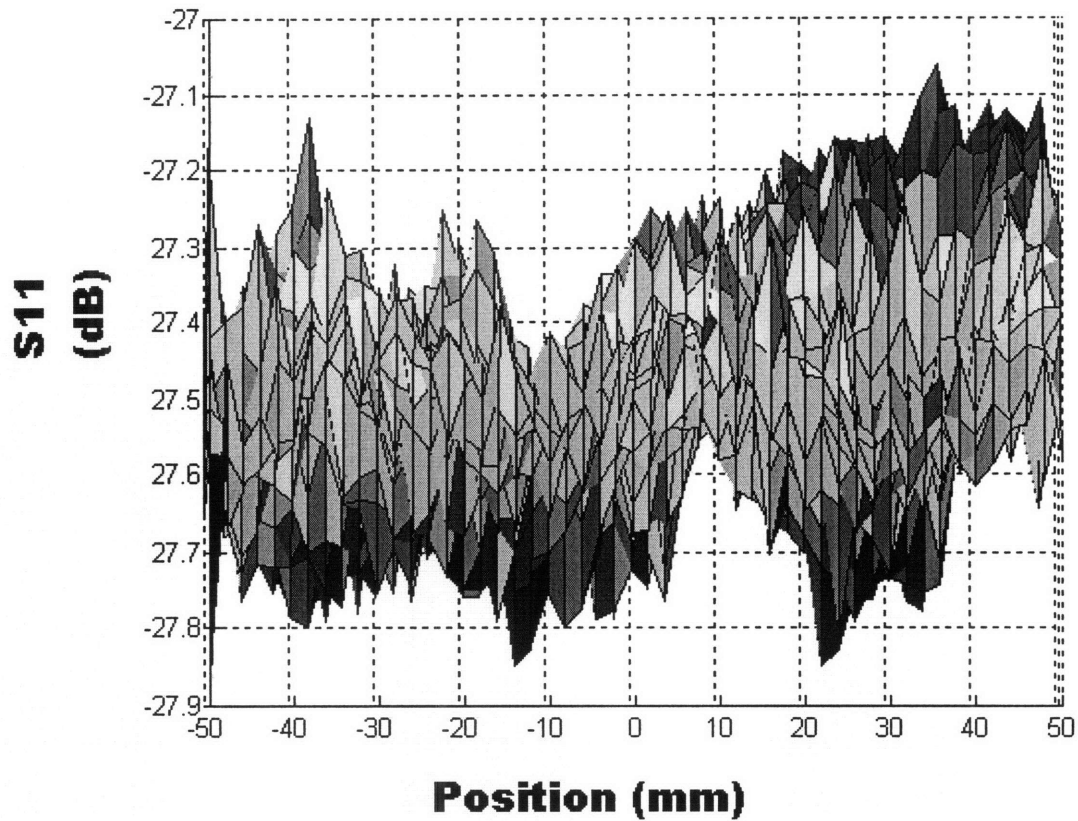
Figure 6-7: Measured change in S_{11} over the course of a full 2-D scan

We can conclude therefore that these measurements should provide accurate data and we do not necessitate any changes to the experimental setup.

6.4   Measuring the ITER Waveguide

While certain aspects of the setup have been touched upon, we summarize here the specifics of the setup for this measurement. We begin with the 170 GHz Oleson millimeter wave VNA transmitting head which is connected to a series of phase shifting

waveguide and uptapers which were described in the previous chapter whose purpose is to generate an HE_{11} mode in the 63.5 mm diameter corrugated waveguide. For the purpose of these measurements, we refer to aforementioned structure as the launcher. Following the launcher, we attach the ITER transmission line components which may include straight sections of waveguide, miter bends, or a combination of several of each. The launcher and transmission line are fixed to an optical table with the open end of the transmission line extending out past one side of the table. The 3-axis scanner is fixed to a separate table and is placed in front of the open end of the transmission line. The receiving millimeter wave VNA head is mounted to the vertical axis of the scanner. A small cut waveguide antenna is attached to the receiver to ensure that we are only measuring the intensity at a particular location. In order to minimize the reflection of power off of the scanner and back into the transmission line, we place eccosorb around the cut waveguide. For each measurement, we manually step the scanner motors so that we are measuring as near as possible to the center of the transmission. This is done more for the purpose of minimizing the size of the measurement plane, since when analyzing the data, routines can be developed to center the data more accurately.

We understand that when it comes to these measurements, there are a number of possibilities for the combinations of transmission line components that can be used and their order. For completeness, it is important that we explore many possibilities, therefore after the launcher we could have: nothing, one meter of straight waveguide, one meter of straight guide followed by a miter bend, a miter bend only, a miter bend followed by one meter of straight waveguide, and so on. We also consider that we have the ability to obtain data in several planes, therefore we could measure as near as possible to the aperture of the waveguide and again after the fields have propagated a distance out from this location.

While figures for each setup could be shown, this would be far too cumbersome, so in this section, only a few representative data plots will be shown, and analysis comparing the various setups will be pursued in the following section.

Figure 6-8 shows a representative plot of the magnitude taken after the launcher section. On the logarithmic scale, the shape matches up quite well with the HE_{11} mode. We see that the magnitude goes to zero at the edge of the waveguide, approximately $\pm$ 30

mm, which is to be expected since the corrugated waveguide only sees the metallic face corresponding to the thickness of the ITER transmission line directly in front of it. We do see an interesting halo effect around the edge of the waveguide which is likely a result of diffraction along the edge. While this is interesting, in the context of determining the mode content of the transmission line, we are only concerned with the data within the walls of the ITER waveguide, thus we can simply truncate the noise that is seen outside of the waveguide diameter.
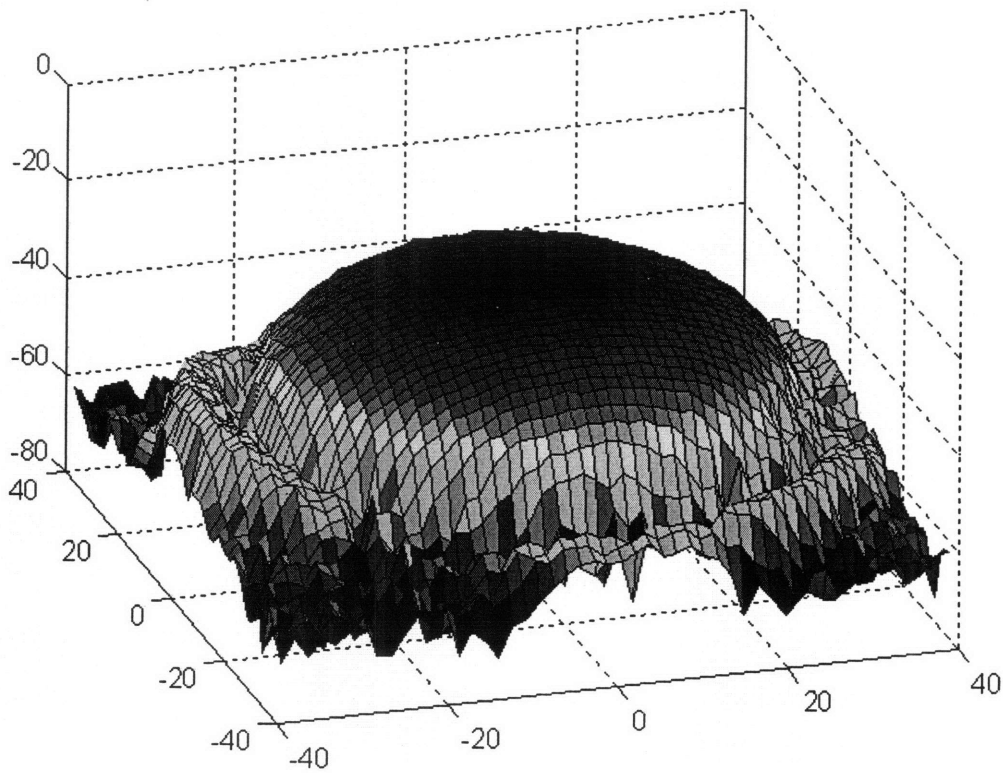
Figure 6-8: Surface plot in dB for a 2-D scan taken at the aperture of the launcher section

A 2-D phase measurement taken at the output of the launcher is shown in Figure 6-9. In the case of the phase measurement, there are a couple of things that we observe. First, we see that outside of the waveguide radius, the noise has a random phase which we are again not particularly concerned with since we will truncate all data outside the waveguide walls. Second, we notice that that the phase is slanted linearly in one direction. While it is flat, which is what we want to see, the slope makes it difficult to obtain

useful data. The origin of this slope in the phase measurement is simply a factor of the alignment between the waveguide aperture and the scanner. If the plane of motion of the scanner is perfectly parallel with the aperture of the waveguide, then we would expect a flat slope. However, in our case, the scanner is at an angle, which is very small but still non-zero, meaning that at one end of the waveguide, we are actually measuring slightly closer or further away than the measurement taken at the opposite end of the waveguide. Since we know that propagation over a distance has a corresponding phase advance, the effect of the misalignment is explained. As a result, the phase data is not particularly useful if this error is too great since it is very hard to determine the actual flat phase value; however, the phase measurements can definitely be used to verify the alignment.

For the majority of the analysis, we will only consider the amplitude of the measured fields.
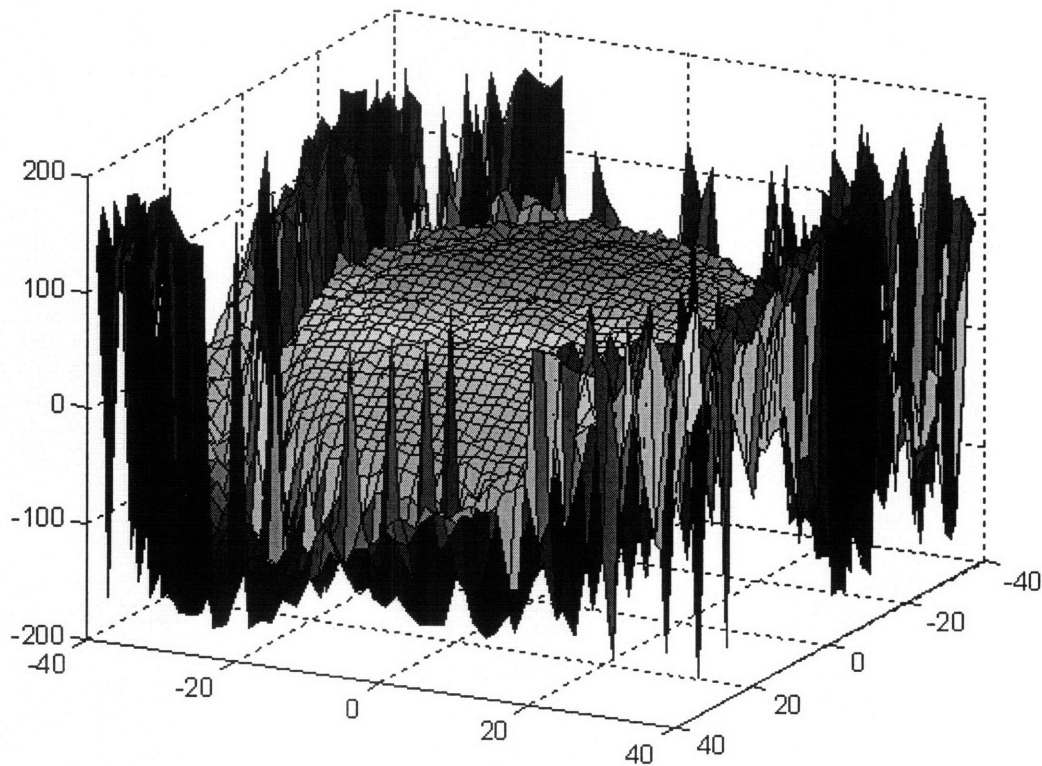
Figure 6-9: Surface plot of the 2-D phase measurement after the launcher section

6.5 Analysis of Measurements

In order to extract meaningful information from the types of results shown in the previous section, we must employ several data analysis routines. As such, several MATLAB routines were created for this analysis to interpolate, shift, and normalize data and to convert all measurements to a more meaningful linear scale. By running these routines, comparisons can be drawn between the different measurements, even if the power levels measured in each case are different.
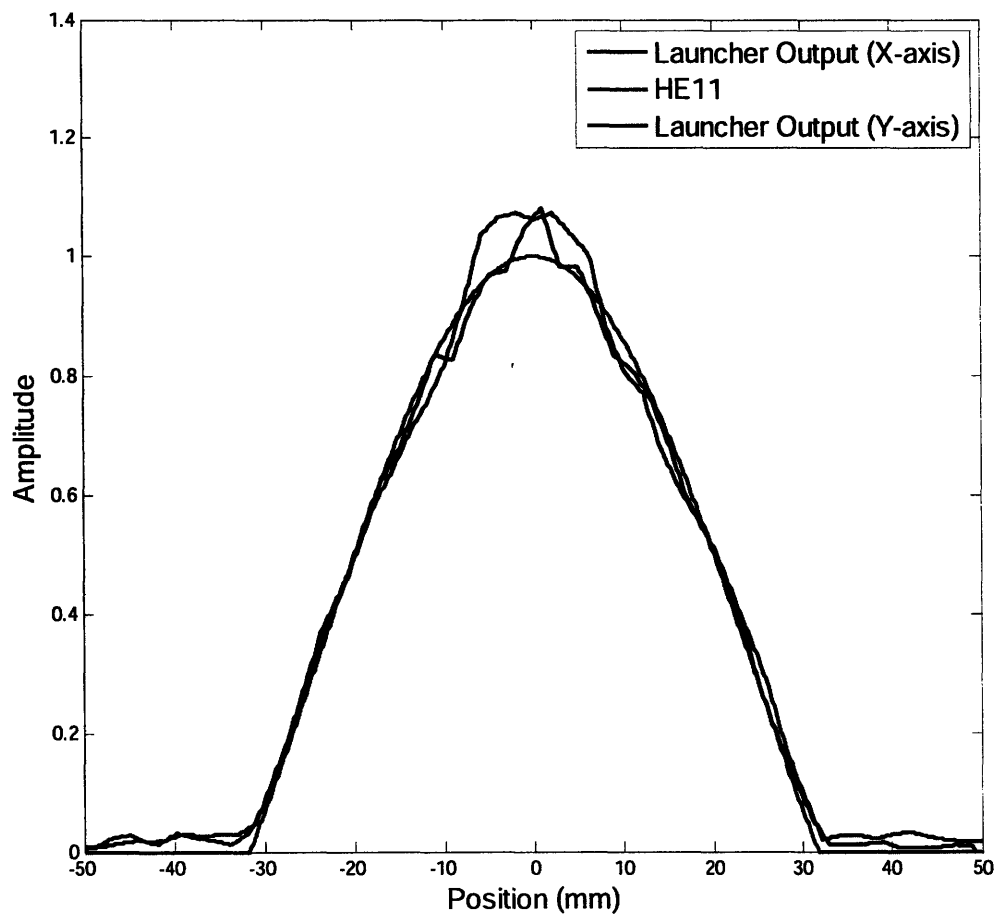
Figure 6-10: Comparison of the cross-sections of the measured field pattern at the output of the launcher compared to a pure HE$_{11}$ mode pattern
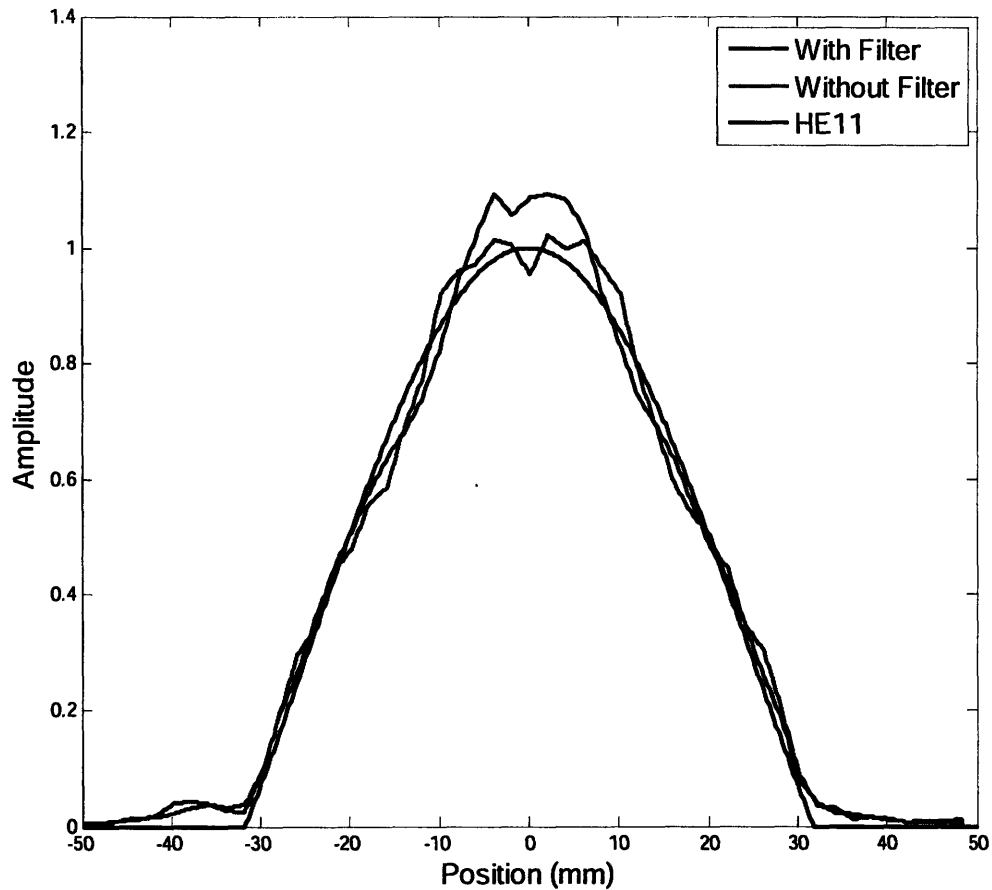
Figure 6-11: Output of the launcher with and without the dielectric filter

As a first order of business, we are interested in seeing if the launcher is outputting a pure HE_{11} mode. Figure 6-10 shows a comparison between the output of the launcher and the HE_{11} mode and we can see that there is a noticeable difference. We see that the mode pattern appears to be squeezed near the center, which could indicate the presence of a higher order mode, or perhaps it could also be an artifact caused by the filter. Therefore, we next look to see the difference in the field pattern if the dielectric filter is included or not to see if it is filtering the higher order modes as expected. In Figure 6-11, we see that when the filter is removed, there are a lot of fluctuations in the field pattern with respect to the HE_{11} mode pattern, which would tend to indicate that there is some higher order mode content that the filter removes. At the same time, we still see a larger peak at the center when the filter is included. This is not necessarily an artifact of the

93

filter, since we must take into consideration that by removing the filter, we have changed the length of the system, and thus we expect the phasing to be different.

To further expand on this, we consider the case of adding a section or two of waveguide after the launcher. When multiple modes propagate in the waveguide, we recognize that the propagation constant of each mode is different, meaning that the relative phase between the two modes changes as the mode mix propagates.
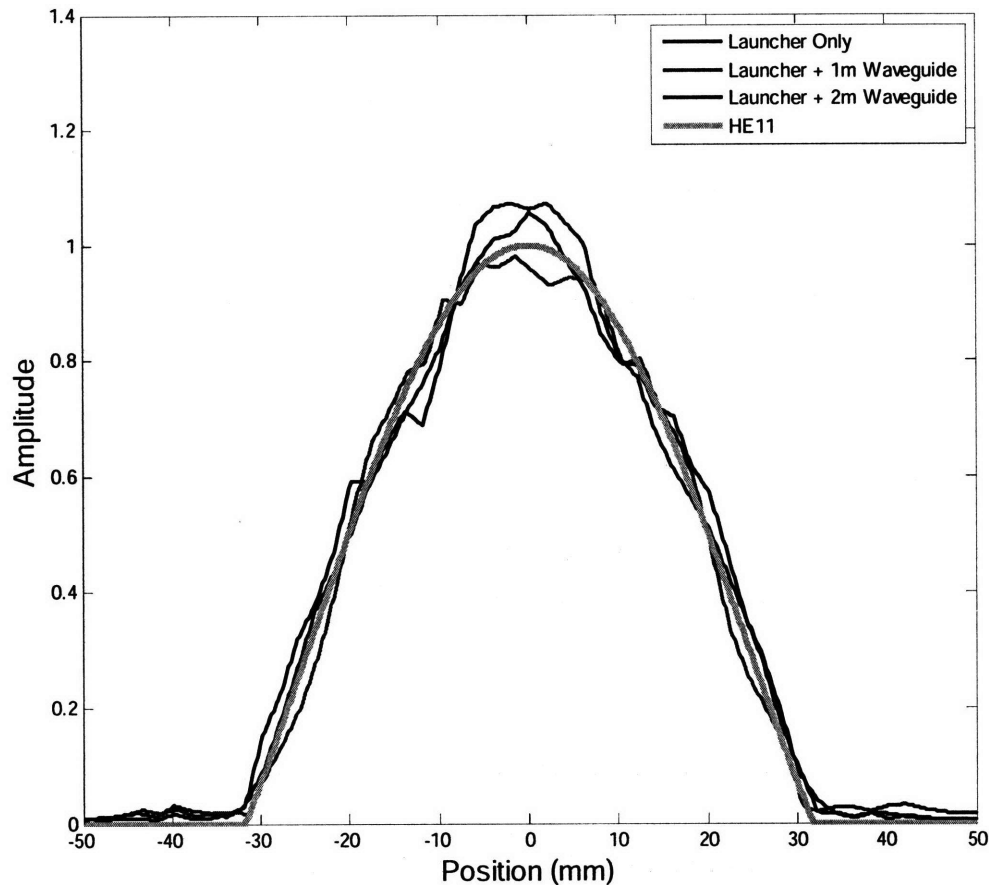
Figure 6-12: Cross-section of the launcher output with varying lengths of waveguide added

Essentially, Figure 6-12 shows how the phasing of the mode mix changes as it propagates down the waveguide. The straight sections of waveguide should not be introducing any mode conversion or other loss. As a result, we can discount the argument that the field pattern at the output of the launcher without any waveguide is caused by anything other than some amount of higher order modes. By only looking at the output with zero or one

meter of waveguide, one could possibly draw the conclusion that the waveguide was acting as a filter of sorts for the higher order mode contact since the field pattern after 1 m of waveguide looks a lot more like the HE_{11} mode; however it is obvious in the measurement after 2 m of waveguide that the higher order mode content is still present.

One way to approximate this higher order mode content is to simply plot various mode mixtures and to see what percentage is necessary to obtain results similar to those seen in the scans. To obtain a peaking at the center on the order of 10 %, we found that the measurement data could be consistent with as little as about 0.5 % HE_{12} mode content; however, that is assuming that the phasing is perfect to generate the pattern and that no other higher order modes are present. Realistic initial estimates indicated that such a pattern was likely consistent with over 1 % high order mode content, which could even be upwards of 3 %. A more rigorous effort to determine this mode content will be outlined in the following section.

The problem with this high order mode content output by the launcher is that it essentially eliminates the possibility of doing any form of differential analysis to determine the mode conversion caused by the miter bend. To be able to proceed with these measurements, we must reduce or come close to eliminating the high order modes. One way to do so is to simply increase the length of the dielectric filter. While this will reduce the dynamic range of the measurements since the HE_{11} mode will also be partially damped, the high order modes will be damped much more severely. This is currently something that we are pursuing.

While the presence of high order modes at the output of the launcher prevents us from obtaining quantitative results on the mode content, we can still look qualitatively at the effect of the miter bend. Figure 6-13 again appears to show that there is noticeable mode conversion being introduced by the miter bend, especially considering that it is plotted on the dB scale; however, this may also again simply be a result of the relative phase of the HOM content. While it is possible to develop a technique to very accurately obtain the mode content both before and after a miter bend, we still have to remember that high order modes at the miter bend's input do have a serious impact on the mode conversion through the miter bend, as was discussed in Chapter 4. Therefore, even with those results, it would still be a difficult to claim a loss figure for the miter bend.
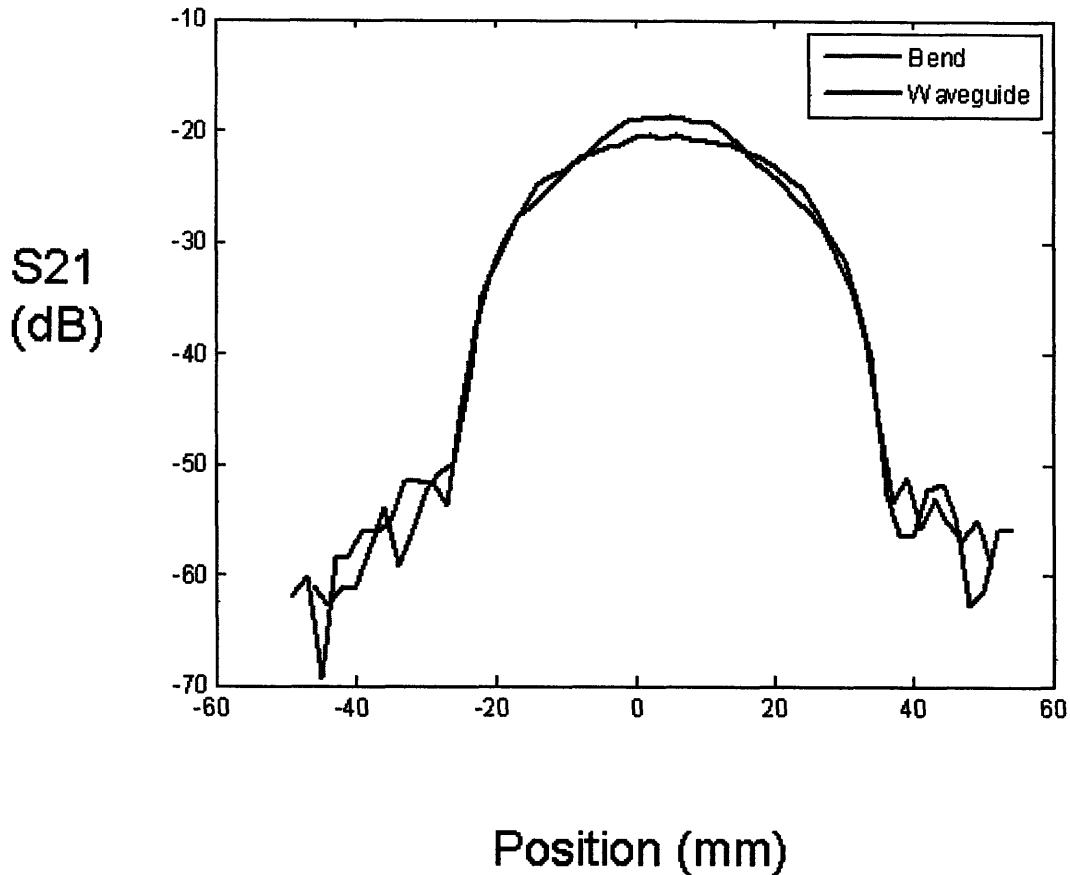
Figure 6-13: Comparison of the output of the launcher with 1 m of straight waveguide and the launcher with a miter bend

6.6 Mode Content Analysis

The ultimate goal of these measurements is to be able to determine the mode conversion caused by the miter bend. As discussed in the previous section, the higher order mode content already present in the line before inserting any miter bend prevents us from obtaining an accurate final solution to that problem. Nonetheless, we can still attempt to determine the mode content of the line as this will be an important part that needs to be solved when we pursue a complete solution to the problem.

There are several ways we can approach the problem of decomposing the measured intensities into the mode content ranging from iterative techniques to simply employing a brute force approach to the problem. We consider the latter first.

One relatively simple way to attack this problem is by taking a few modes, and solving across a range of different combinations to find which one best fits the given data, i.e. a brute force approach. There are a few problems with this approach. First of all, we must recognize that it is not simply the magnitude of the various modes that determines the measured field pattern, it is also the phases of each mode, thus for every mode we must sweep across two variables. The main problem is the computational time required. Even if as few as three modes are considered across a handful of magnitudes and phases, the number of computations required quickly jumps up, taking upwards of one minute. If we introduced 100 new amplitude and phase combinations for a fourth mode, then the required time would be well over an hour, and the problem quickly becomes unsolvable in a reasonable time frame. If we limit the number of modes, we encounter a problem similar to the problem with the TE_{01} miter bend simulations in that we will fail to converge on a single correct solution. This issue is actually already well documented in [37]. Essentially, in these situations, there exist several combinations of eigenmodes that will produce similar matches to the given field pattern, and it is impossible to distinguish which is correct without having more information. As a result, we must consider a method that takes into consideration the phase information of the measured data.

Even if we are unable to obtain viable phase data to accompany field profile measurements, we can use a phase retrieval code to extract this information from amplitude measurements in multiple planes. In the case of the ITER measurements, we have measured the output directly after launcher and after one and two meters of straight waveguide, therefore we will apply the phase retrieval code to this data to obtain the phase and determine the mode content being launched.

We have two arrays of measured amplitudes $A_1(x,y)$ and $A_2(x,y)$ representing the values at plane 1 and at plane 2 respectively, which are separated by a distance L. We assume an initial flat phase of zero at the first measurement plane, i.e. $\varphi_1(x,y) = 0$. We recognize that the data at each plane can be written as a sum of eigenmodes ψ_{mn}, such that:

$$A(x,y)e^{j\varphi(x,y)} = \sum_{m,n} C_{mn} \exp(j\theta_{mn})\psi_{mn}(x,y) \tag{6.1}$$

where the constants C_{mn} are determined by:

$$C_{mn} = \frac{\int A(x,y)e^{j\varphi(x,y)}\psi_{mn}(x,y)dxdy}{\int \psi_{mn}^2(x,y)dxdy} \tag{6.2}$$

For the assumed zero initial phase, we have $\theta_{mn}=0$. We begin by determining a first set of coefficients $C_{mn}^{(0)}$ for the first plane. We can then propagate the fields at the first plane to the second plane. Therefore:

$$\widetilde{A}_2(x,y)\exp(j\varphi_2(x,y)) = \sum_{mn} C_{mn}^{(0)} \exp(j\theta_{mn})\exp(j\beta_{mn}L)\psi_{mn}(x,y) \tag{6.3}$$

where $\widetilde{A}$ will always represent the projected amplitudes and β_{mn} is the propagation constant of eigenmode ψ_{mn}. We now replace the projected amplitude at the second plane with the measured amplitude, though we retain the projected phase, and solve for the series of eigenmodes and the set of constants:

$$A_2(x,y)\exp(j\varphi_2(x,y)) = \sum_{mn} C_{mn}^{(1)} \exp(j\beta_{mn}L)\psi_{mn}(x,y)\exp(j\theta_{mn}^{(1)}) \tag{6.4}$$

$$C_{mn}^{(1)} \exp(j\beta_{mn}L)\exp(j\theta_{mn}^{(1)}) = \frac{\int A_2(x,y)\exp(j\varphi_2(x,y))\psi_{mn}(x,y)dxdy}{\int \psi_{mn}^2(x,y)dxdy} \tag{6.5}$$

We now propagate the above fields back to the first plane, resulting in an amplitude $\widetilde{A}_1(x,y)$ and a new non-zero phase $\varphi_1(x,y)$. The same process as described above is then repeated: replace the projected amplitude with the measured amplitude, use the measured amplitude and the projected phase to solve for the coefficients C_{mn} and θ_{mn}, then propagate the newly calculated fields back to the other plane. The iterative nature of this phase

retrieval code is clear. After each iteration, we calculate the value of a convergence parameter, which we choose to be:

$$\Delta = \int \left[A^2_{measured} - A^2_{projected} \right]^2 dxdy \qquad (6.6)$$

Once this convergence parameter drops below the requirement established at the outset, we can determine that the calculated phase at each plane is accurate and we can use this complete set of information to determine the mode content.

Using the technique that has just been described, we evaluated the mode content from the launcher in the ITER waveguide. Using the data from 2-D scans right after the launcher, after 1 meter of waveguide and after 2 meters of waveguide, we were able to determine the mode content shown in Table 6.1. Depending on the measurement planes that we considered, there was a small variation; therefore we estimate that there is approximately 2 ± 0.5 % HOM content.

Mode	Power	Phase
HE_{11}	98.01%	0°
HE_{31}	0.14%	88°
HE_{22}	0.31%	263°
HE_{13}	0.24%	332°
HE_{14}	0.24%	269°

Table 6.1: Calculated mode content of the output of the launcher used for measurement of the prototype ITER ECH transmission line

We can test this calculated mode content by plotting the fields and comparing the result with the measurements of the ITER transmission line. This comparison is plotted in Figure 6-14, and the agreement is quite good.
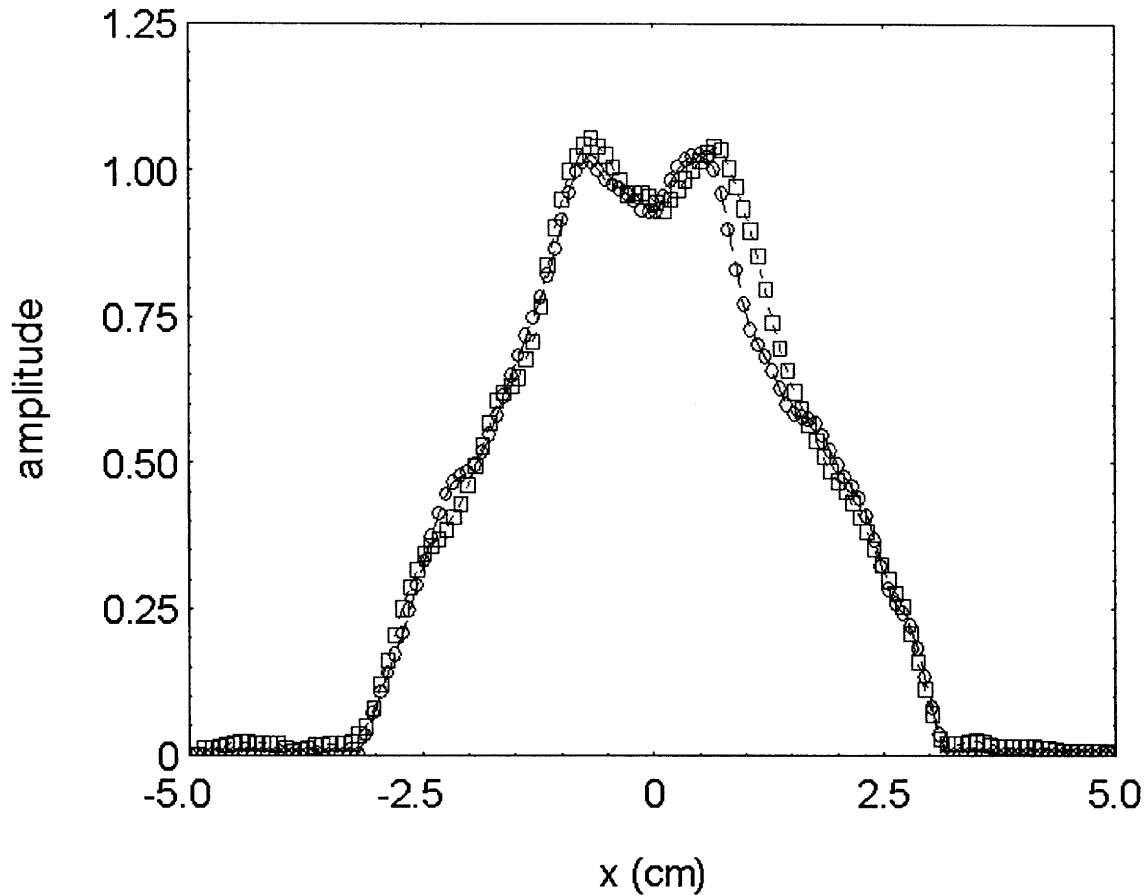
Figure 6-14: Comparison of the retrieved mode content using the iterative code (blue circles) and the data measured using the scanner system (red squares)

6.7 Summary

Preliminary 1-D scans of the field profile of the ITER transmission line with and without a miter bend showed good promise that the mode conversion could be measured. As a result, we constructed a 3-axis scanning system that would enable the measurement of full 2-D field profiles. Testing of this system showed that we can obtain very accurate and repeatable results.

Field profiles for the transmission line were measured for a variety of configurations of waveguide lengths and with and without miter bends. After developing the analysis tools to review this data, we quickly found that the high order mode content output by the launcher was much higher than anticipated. Because of this higher order mode content,

we can not make a definitive assessment of the mode conversion resulting from the miter bends, and a new longer filter was proposed to eliminate this higher order mode content.

Nevertheless, we worked to develop methods to extract the mode content from the measurement data. By employing an iterative phase retrieval code, we were able to generate a solution that provided a field profile which agreed reasonably well with the experimental data.

Chapter 7

Conclusion

7.1 Summary

This work has covered a broad range of topics with regards to the applications, theory, and experimental measurement of millimeter wave transmission lines. Millimeter wave transmission lines are an integral component in a number of important applications ranging from nuclear fusion to spectroscopy to radar.

Unlike their lower frequency counterparts, the core of the millimeter wave transmission line is the structure known as a waveguide. Typically made out of metal, these waveguides confine the fields within in a particular distribution that satisfies the boundary condition known as a mode. These modes propagate down the waveguide and encounter an Ohmic loss proportional to the square of the field along the walls. Waveguides can come in all sorts of shapes and sizes, from rectangular to circular, and when low loss is desired, waveguide with corrugated walls is preferred. Corrugated waveguides propagate hybrid modes, having both longitudinal magnetic and electric fields, such as the HE_{11} mode, which exhibits the lowest loss. In transmission lines, to reduce losses, it is advisable to use waveguide with a high radius to wavelength ratio (a/λ) for the frequency of the application. In these cases, the Ohmic losses are negligible in comparison with the mode conversion loss of transmission line components such as the miter bend. The loss in a miter bend is calculated from a theory that approximates the miter bend geometry as a simple gap one diameter in length between two waveguides. The loss of the gap is twice the loss in the miter bend since continuing the waveguide walls to the location of the miter bend's mirror would effectively eliminate diffraction in one of two planes.

While the gap theory is widely accepted, there is no arguing that it requires several assumptions. To determine its validity, we first explored via numerical simulation if the analytical theory for the gap loss was correct. HFSS simulations of the waveguide gap showed excellent agreement with theory; however, it is relating this gap loss to the loss in a miter bend that is the biggest point of contention in the theory. Due to limitations of the simulation code, it was impossible to obtain conclusive results for the miter bend geometry, though simulation at low a/λ did agree reasonably well with the assertion of gap theory that the loss in the miter bend is half that of the gap. We also found that mode conversion favored the low order modes that shared symmetry with the input mode and that due to the symmetry of the 90° bend, for a mode with an even azimuthal mode number, modes with odd azimuthal mode number will have exactly the same amount of power propagating forward through the output and reflecting back through the input.

We next considered the problem of what happens when the input mode at a miter bend is actually a mix between a dominant HE_{11} mode and a parasitic higher order mode (HOM). Using a new numerical technique that considers an improved gap geometry which involves the continuation of the waveguide walls into the gap to where the mirror would be located, we were able to show that the mode conversion loss in the miter bend is strongly dependent on the amplitude and the relative phase of the parasitic HOM. Even for a couple of percent of HOM content at the input, if the relative phase of the parasitic mode is a particular value, the mode conversion loss could increase by about 50 %; though the average across all phases does remain about the same regardless of the amount of HOM content. On the other hand, the loss into the gap, which corresponds to very high order modes that will be absorbed into the transmission line near the miter bends, will increase on average with higher proportions of HOM content.

We also explored several techniques for measuring the loss in millimeter wave transmission line components. We first introduced a coherent technique using a VNA and an incoherent technique using a radiometer to measure the loss in a miter bend, with the measured losses being 0.3 ± 0.1 dB and 0.22 ± 0.1 dB respectively for a line whose theoretical loss is 0.17 dB. We next measured the ITER transmission line, whose predicted loss is 0.027 dB, and found the loss to be 0.05 ± 0.02 dB using the VNA

technique. While all results showed relatively good agreement, it is still noticeable that all measurements showed losses greater than those predicted by gap theory.

We next considered measuring the mode content of the ITER transmission line. To accomplish this, we constructed an experimental setup consisting of a 3-axis scanner, a VNA, and a LabView code. The 2-D field profiles measured using this setup are very accurate and repeatable. Upon analyzing the results of various measurements of the HE_{11} mode launcher and different combinations of waveguide sections and miter bends, we found that even without any miter bends, there was a significant amount of higher order modes within the line. Due to this HOM content, it is not possible at this time to determine with proper certainty the actual mode conversion caused by a miter bend. However, using a phase retrieval code, we were able to calculate that the HOM content of the launcher sections, including a small dielectric filter, is on the order of 2 %. In order to decrease the HOM content, we will implement a longer filter that will further damp all HOMs.

7.2   Future Work

There are a couple of areas in which work can continue on this project.

With regards to the miter bend simulations, if HFSS increases the mode limit on waveports (which was supposed to happen when the latest version was released earlier this year), then new simulations can be run for some larger values of a/λ. This could definitely help provide some more insight on the relationship between the loss in the gap and the loss in a miter bend.

The rest of the work that we could pursue pertains to the experiments. When the new filter is obtained, a new series of scanner measurements can be taken with the hope that the launcher output will be very close to a pure HE_{11} mode. If this is the case, then the mode conversion in the miter bend should be possible to determine.

It would also be advisable to reconsider some of the original loss measurements. The new filter could also yield an improvement in these measurements; however there is also another factor that may improve these results. When setting up the scanner experiment, we purchased longer VNA cables. The length of the VNA cables was actually a

limiting factor in the original loss measurements and prevented the 20.32 mm − 63.5 mm tapers from being included in the baseline measurement. Thus, any loss that these components may have introduced is also included in the DUT loss which is attributed purely to the miter bends.

References

[1] ITER team, vol. 2008,

[2] Kobayashi, N. et al, "Design of electron cyclotron heating and current drive system of ITER," in 2007,

[3] T. Imai, N. Kobayashi, R. Temkin, M. Thumm, M. Q. Tran and V. Alikaev, "ITER R and D: Auxiliary systems: Electron cyclotron heating and current drive system," *Fusion Engineering and Design*, vol. 55, pp. 281-289, 2001.

[4] W. Suttrop, vol. 2008, 1997.

[5] M. Bornatici, R. Cano, O. De Barbieri and F. Engelmann, "Electron Cyclotron Emission and Absorption in Fusion Plasmas," *Nuclear Fusion*, vol. 23, pp. 1153-1258, 1983.

[6] Equipe TFR, "Tokamak Plasma Diagnostics," *Nuclear Fusion*, vol. 18, pp. 647-732, 1978.

[7] M. K. Hornstein, V. S. Bajaj, R. G. Griffin, K. E. Kreischer, I. Mastovsky, M. A. Shapiro, J. R. Sirigiri and R. J. Temkin, "Second harmonic operation at 460 GHz and broadband continuous frequency tuning of a gyrotron oscillator," *Electron Devices, IEEE Transactions on*, vol. 52, pp. 798-807, 2005.

[8] V. Weis, M. Bennati, M. Rosay, J. A. Bryant and R. G. Griffin, "High-Field DNP and ENDOR with a Novel Multiple-Frequency Resonance Structure," *Journal of Magnetic Resonance*, vol. 140, pp. 293-299, 9. 1999.

[9] A. Barnes, G. De Paepe, van der Wel, P.C.A., K. Hu, V. S. Bajaj, M. L. Mak-Jurkauskas, J. Herzfeld and R. G. Griffin, "High field dynamic nuclear polarization for solid and solution biological NMR," *Appl. Magn. Reson.*, submitted 2008.

[10] L. R. Becerra, G. J. Gerfen, R. J. Temkin, D. J. Singel and R. G. Griffin, "Dynamic nuclear polarization with a cyclotron resonance maser at 5 T," *Phys. Rev. Lett.,* vol. 71, pp. 3561-3564, Nov. 1993.

[11] G. J. Gerfen, L. R. Becerra, D. A. Hall, R. G. Griffin, R. J. Temkin and D. J. Singel, "High frequency (140 GHz) dynamic nuclear polarization: polarization transfer to a solute in frozen aqueous solution," *J. Chem. Phys.,* vol. 102, pp. 9494-9497, 1995.

[12] C. -. Joo, K. -. Hu, J. A. Bryant and R. G. Griffin, "In situ temperature jump high-frequency dynamic nuclear polarization experiments: enhanced sensitivity in liquid-state NMR spectroscopy," *J. Am. Chem. Soc.,* vol. 128, pp. 9428-9432, 2006.

[13] J. A. Kong, *Electromagnetic Wave Theory.* Cambridge, MA: EMW Publishing, 2005,

[14] C. S. Lee, S. W. Lee and S. L. Chuang, "Plot of Modal Field Distribution in Rectangular and Circular Waveguides," *Microwave Theory and Techniques, IEEE Transactions on,* vol. 33, pp. 271-274, 1985.

[15] J. L. Doane, "Propagation and mode coupling in corrugated and smooth-wall circular waveguides," in *Infrared and Millimeter Waves ,* vol. 13, K. J. Button, Ed. New York: Academic Press, Inc., 1985, pp. 123-170.

[16] D. Wagner, J. Pretterebner and M. Thumm, "Eigenmode mixtures in circumferentially corrugated waveguides," *Proc. EC-8,* vol. 2, pp. 575-585, 1993.

[17] P. J. B. Clarricoats, A. D. Olver and S. L. Chong, "Attenuation in Corrugated Circular Waveguides," *Proc. IEE,* vol. 122, pp. 1173-1179, 1975.

[18] P. J. B. Clarricoats and M. I. Sobhy, "Propagation Behaviour of Periodically Loaded Waveguides," *Proc. IEE,* vol. 115, pp. 652-661, 1968.

[19] E. A. J. Marcatili and R. A. Schmeltzer, "Hollow Metallic and Dielectric Waveguides for Long Distance Optical Transmission and Lasers," *Bell System Technical Journal,* vol. 43, pp. 1783-1809, 1964.

[20] C. Dragone, "Reflection, Transmission, and Mode Conversion in a Corrugated Feed," *Bell System Technical Journal,* vol. 56, pp. 835-867, 1977.

[21] J. L. Doane, "Design of circular corrugated waveguides to transmit millimeter waves at ITER," *Fusion Sci. Tech.,* vol. 53, pp. 159-173, 2008.

[22] M. K. Thumm and W. Kasparek, "Passive high-power microwave components," *Plasma Science, IEEE Transactions on,* vol. 30, pp. 755-786, 2002.

[23] R. B. Vaganov, "Phase corrector in the bend of a wide waveguide," *Radio Eng. Electron Phys.,* vol. 18, pp. 170-175, 1973.

[24] S. T. Han, M. A. Shapiro, J. R. Sirigiri, D. S. Tax, R. J. Temkin and P. P. Woskov, "Low power testing of losses in components for the ITER ECH transmission lines," in 2007,

[25] E. A. J. Marcatili, "Miter elbow for circular electric mode," in 1964, pp. 535-542.

[26] B. Z. Katsenelenbaum, "Diffraction on Plane Mirror in Broad-Waveguide Junction," *Radio Eng. Electron Phys.,* vol. 8, pp. 1098-1106, 1963.

[27] I. P. Kotik and A. N. Sivov, "Diffraction of Electromagnetic Waves on a Mirror in a Break of a Plane Waveguide," *Radiotekhnika i Elektronika,* vol. 9, 1964.

[28] R. B. Vaganov, "Phase Corrector in the Bend of a Wide Waveguide," *Radio Engineering and Electronic Physics,* vol. 18, pp. 170-175, 1973.

[29] D. Wagner, M. Thumm and W. Kasparek, "Spectrum of unwanted spurious modes generated by flat and phase correcting mirrors in highly oversized HE_{11} and TE_{01} elbow bends," in 1990, pp. 437-439.

[30] R. B. Vaganov, "Measurements of Losses of Certain Quasioptical Waveguide Elements," *Radio Engineering and Electronic Physics,* vol. 8, pp. 1228-1231, 1963.

[31] J. L. Doane and C. P. Moeller, "HE_{11} Mitre Bends and Gaps in a Circular Corrugated Waveguide," *Int. J. Electronics,* vol. 77, pp. 489-509, 1994.

[32] D. Wagner, M. Thumm, W. Kasparek, G. A. Muller and O. Braz, "Prediction of TE-, TM-, and Hybrid-Mode Transmission Losses in Gaps of Oversized Waveguides Using a Scattering Matrix Code," *International Journal of Infrared and Millimeter Waves,* vol. 17, pp. 1071-1081, 1996.

[33] M. A. Shapiro and S. N. Vlasov, "Study of combined transmission line for high power wave generated by a gyrotron in the millimeter wavelength range," *Int. J. Electron.,* vol. 72, pp. 1127-1133, 1992.

[34] K. Ohkubo, S. Kubo, H. Idei, M. Sato, T. Shimozuma and Y. Takita, "Coupling of Tilting Gaussian Beam with Hybrid Mode in the Corrugated Waveguide," *International Journal of Infrared and Millimeter Waves,* vol. 18, pp. 23-41, 1997.

[35] K. Kajiwara, K. Takahashi, N. Kobayashi, A. Kasugai, T. Kobayashi and K. Sakamoto, "Development of the transmission line and the launcher for the ITER ECH system," *Infrared and Millimeter Waves, 2007 and the 2007 15th International Conference on Terahertz Electronics. IRMMW-THz. Joint 32nd International Conference on,* pp. 793-794, 2007.

[36] P. P. Woskov, V. S. Bajaj, M. K. Hornstein, R. J. Temkin and R. G. Griffin, "Corrugated Waveguide and Directional Coupler for 250-GHz Gyrotron DNP Experiments," *IEEE Trans. Microwave Theory and Tech.,* vol. 53, pp. 1863-1869, 2005.

[37] O. Shapira, A. F. Abouraddy, J. D. Joannopoulos and Y. Fink, "Complete Modal Decomposition for Optical Waveguides," *Phys. Rev. Lett.,* vol. 94, pp. 143902, April 15, 2005. 2005.